To

My Family

and

Delia

Declaration

This thesis contains the results of research undertaken by the author between October 1998 and March 2005 in the Emerging Technologies Research Centre, De Montfort University. This research is entirely my own original work and contains nothing done in collaboration except where explicit acknowledgment is given.

This work has not been submitted in whole or in part for any other University degree or diploma.

Permission is granted to consult or copy the information contained herein for the purposes of private study but not for publication.

Richard Barrie Michael Cross

Leicester, March 2005

Summary

Low temperature (< 150 °C) hydrogenated amorphous silicon grown by PECVD with source gas heating

Richard Barrie Michael Cross

Hydrogenated amorphous silicon (a-Si:H) is a semiconductor that is widely used in a variety of applications. A particularly important development has been the incorporation of this material into thin film transistor (TFT) arrays for the active matrix addressing of liquid crystal displays. Plasma Enhanced Chemical Vapour Deposition (PECVD) is one of the most successful techniques currently in use for the deposition of device quality a-Si:H. However, there is an increasing desire to improve process compatibility with low cost, plastic substrates. This entails trying to reduce the deposition temperature from approximately 250 – 300 °C to below 150 °C, whilst maintaining material quality.

This thesis describes the design of a novel, low temperature PECVD system incorporating the facility to pre-heat the deposition source gases. The physical and electronic properties of a-Si:H deposited at <150 °C are investigated, and the performance of TFT structures incorporating optimised material as the active layer is described.

It is shown that the physical properties of a-Si:H produced at a substrate temperature of 125 °C with the source gas line heated to 400 °C are commensurate with films deposited at 250-300 °C. The hydrogen content of the optimised film was found to be 10.5 %, with a Tauc bandgap of 1.66 eV. Pre-heating of the source gases also leads to an increase in the proportion of hydrogen bonded in the monohydride configuration. It is suggested that the diffusion of the film-forming gaseous species is enhanced by this technique, resulting in a reduction in the degree of disorder within the film and hydrogen elimination. Consequently, the concentration of hydrogen and the Tauc

bandgap also decrease, leading to an increase in photoconductivity of one order of magnitude. TFTs exhibit a switching ratio of 10^5, which is approximately an order of magnitude smaller than high temperature a-Si:H TFTs, but a comparable OFF current of approximately 10^{-12}A. However, the field effect mobility of these devices is very poor (10^{-3} $cm^2V^{-1}s^{-1}$). This is thought to be due to a high interface state density at the boundary between the low temperature, gas-heated a-Si:H layer and the high temperature silicon nitride gate insulator.

Acknowledgements

The author would like to thank the following without whose help and support this work would not have been possible:

EPSRC: for financial support over three years and three months of this research

Philips Research Laboratories: for financial support over three years of this research and for providing the photolithographic mask set used to define the thin film transistor structures.

Frank Clough: my supervisor for the first ten months of this research, for his advice, encouragement and support. Not to mention his (at times tested) patience!

Shankar Ekkanath Madathil: my supervisor for the remainder of this research, for his support, encouragement and good humour.

David Oxley: for his invaluable advice and efforts quite beyond the call of duty and for his help proof reading this thesis.

Andrew Flewitt: for his advice on PECVD system design and numerous aspects of this research.

Paul Taylor: for his technical knowledge, advice and assistance, and limitless bonhomie.

Mark, Tim, Chanders, David, Subhas, Shashi and Xu: for help and comedy through some testing times.

Contents

	Page
Declaration	
Summary	I
Acknowledgements	III
Notation	VIII
Chapter 1: Introduction	
1.1 Overview of a-Si:H and its Applications	1
1.2 Outline of Thesis	3
Chapter 2: The Structure and Electronic Properties of a-Si:H	
2.1 Introduction	5
2.2 Atomic Structure of a-Si	5
2.3 The Role of Hydrogen	7
2.4 Electronic Structure of a-Si:H	8
2.4.1 Band Structure in a-Si:H	8
2.4.2 Conduction in a-Si:H	10
2.4.3 Doped a-Si:H	12
2.5 The Metastability of a-Si:H	15
2.5.1 Metastable State Creation	15
2.5.2 Metastable Changes in Doping Efficiency	17
2.5.3 Metastable Defects Induced by Particle Bombardment	18
2.5.4 The Defect Pool Model	19
Chapter 3: The Structure and Electronic Properties of a-Si:H TFTs	
3.1 Introduction	22
3.2 Background to TFTs	22

3.3 Operation of the Metal-Insulator-Semiconductor Field Effect Transistor (MISFET) 23
3.4 The Structure and Operation of a-Si:H TFTs 25
3.4.1 The Operation of a-Si:H TFTs 27
3.5 Instability of a-Si:H TFTs 31
3.6 Electrical Contacts to a-Si:H 32
3.7 Device Design of Test Structures 34

Chapter 4: Plasma Enhanced Chemical Vapour Deposition of a-Si:H

4.1 Introduction 36
4.2 Overview of Chemical Vapour Deposition (CVD) 36
4.3 Plasma Enhanced Chemical Vapour Deposition (PECVD) 38
4.3.1 RF Discharges 40
4.3.1.1 Plasma Anatomy 41
4.3.1.2 Gas Phase Chemical Processes 42
4.3.1.3 α-γ Transition 44
4.3.2 The Deposition Process of a-Si:H 46
4.3.2.1 The Effect of Ions 50
4.4 Low Temperature Deposition of a-Si:H 52
4.1.1 The Novel PECVD system 53

Chapter 5: Thin Film and TFT Characterisation Techniques

5.1 Introduction 56
5.2 Physical Characterisation 56
5.2.1 Fourier Transform Infrared Spectroscopy (FTIR) 56
5.2.2 UV/VIS Spectroscopy 59
5.2.3 Film Thickness Measurement 60
5.2.4 Ellipsometry 61
5.2.5 Etch Rate Measurements 61
5.3 Electrical Characterisation 62
5.3.1 Conductivity Measurements 62
5.3.2 Dielectric Strength Measurements 64

5.3.3 Interfacial Characterisation 65
5.3.4 Electrical Measurements of TFTs 66
5.3.4.1 Transfer Characteristics 66
5.3.4.2 Output Characteristics 68
5.3.5 Assessment of TFT Stability 68

Chapter 6: Experimental Optimisation of a-Si:H films grown by PECVD with Source Gas Heating

6.1 Introduction 70
6.2 System Evaluation 70
6.3 Experimental Optimisation of a-Si:H 72
6.3.1 Silane Flow Rate 73
6.3.2 Hydrogen Flow Rate 75
6.3.3 Substrate Temperature 78
6.3.4 Power 81
6.3.5 Pressure 82
6.4 Summary of Initial Optimisation 83
6.5 Source Gas Heating Investigations 84
6.6 Properties of Optimised a-Si:H Grown with Source Gas Heating 92

Chapter 7: Plasma Enhanced Chemical Vapour Deposition of Silicon Nitride

7.1 Introduction 94
7.2 PECVD Silicon Nitride 94
7.3 Optimisation of PECVD Silicon Nitride 97
7.3.1 Deposition Rate 98
7.3.2 Physical Characterisation 99
7.3.3 Bulk Electrical Characterisation 104
7.3.4 Interfacial Characterisation 106
7.3.5 Properties of Optimised PECVD Silicon Nitride 107
7.4 Towards complete TFTs produced at a low thermal budget 108

Chapter 8: The Performance of TFTs using low temperature PECVD a-Si:H

8.1 Introduction **111**

8.2 Gas Heated a-Si:H TFT (GH-TFTs) Characteristics **111**

8.2.1 Transfer Characteristics **111**

8.2.2 Output Characteristics **114**

8.2.3 Gas Heated a-Si:H TFT Stability **115**

8.3 Comparison with Room Temperature a-Si:H TFTs (RT-TFTs) **117**

Chapter 9: Conclusions and Future Work

9.1 Contributions **123**

9.2 Conclusions **123**

9.3 Future Work **125**

References **127**

Appendices

A: Low Temperature PECVD Chamber Schematics **145**

B: Substrate Preparation **153**

C: TFT Fabrication Procedure **154**

D: Photolithographic Processing Steps **157**

Notation

UNITS

It is most usual in this field to use c.g.s. units rather than the more conventional S. I. units. Therefore, for compatibility with other published data c.g.s. units have been adopted for all experimental results and equations used in this thesis.

REFERENCES

References to published literature are given in the text in square brackets, and direct the reader to the list given at the back of this dissertation. The numerical value of each reference is determined by the order in which it first appears in the text. References in round brackets preceded by the symbol §, direct the reader to sections of this thesis. Numbers in round brackets refer to equations and reactions within the body of the text.

ABBREVIATIONS AND SYMBOLS

All abbreviations used in the text are written out in full at their first occurrence, followed by the relevant abbreviation in round brackets.

KEYWORDS

Plasma Enhanced Chemical Vapour Deposition (PECVD) Low Temperature

Hydrogenated Amorphous Silicon (a-Si:H) Thin Film Transistor (TFT)

Chapter 1

Introduction

The aim of this chapter is to give a brief overview of hydrogenated amorphous silicon (a-Si:H) and to outline its many applications. Particular emphasis is placed on the growth at low temperatures of a-Si:H for Thin Film Transistors (TFTs) applications, or for use in Active Matrix Liquid Crystal Displays (AMLCDs). Following this, the research contained within this thesis is outlined.

1.1 OVERVIEW OF A-Si:H AND ITS APPLICATIONS

Research on amorphous semiconductors began in earnest in the 1950s and 1960s and focussed on the chalcogenides, i.e. materials containing sulphur, selenium and tellurium. Of particular interest was how the disorder of the non-crystalline structure influenced the electronic properties. However, it was the pioneering work of Chittick et al [1], and Spear and LeComber [2][3], that first stimulated interest in a-Si:H as an electronic material.

A-Si:H can be produced by a number of different methods, but the most commonly used technique is Plasma Enhanced Chemical Vapour Deposition (PECVD). This process enables a-Si:H to be deposited uniformly over large areas, at low temperatures ($< \sim 300$ °C) and on to a variety of substrates. The large area compatibility is a distinct advantage over conventional semiconductor materials, e.g. crystalline-silicon (c-Si), which must be grown as single crystals that are then sawn into wafers. This limits the structures based on single crystal semiconductors to the maximum available wafer size.

Device research based on a-Si:H was initiated by Carlson and Wronski [4] with the development of photovoltaic devices. Since then, there has been considerable investigation and development of this material leading to many different applications. In the photovoltaic field, these range from solar cell modules for consumer electronics

(calculators, watches etc.), to flexible modules used as building-integrated roofing elements [5]. Other devices include radiation detectors [6], X-ray imagers [7] and high voltage TFTs [8].

However, by far the main application for a-Si:H is its use as the active material in the pixel switching elements (TFTs), in Active Matrix Liquid Crystal Displays (AMLCDs). The principle of active matrix displays using TFTs was first described by Lechner et al [9], but the first commercial product to use a-Si:H TFTs in an active matrix was developed by Matsushita [10].

A liquid crystal (LC) is a material that responds to an applied voltage by rotating the plane of polarisation of light passing through it. An AMLCD consists of an array of LC cells (or pixels) that are sequentially addressed by switching elements [11][12]. When the LC is placed between two polarising films, light transmission is controlled by the voltage on each pixel electrode. The a-Si:H TFTs act as switches that control this voltage.

The TFTs are turned on one gate line at a time, and information is passed to each pixel individually. The pixels in the other lines are unaffected provided the off currents of the transistors are low enough. When the TFTs are turned off, the liquid crystal maintains its state for the whole of the scan time as it forms part of the pixel capacitance. During this period, pixels on other gate lines are addressed.

The flat panel display market as a whole has seen rapid growth in recent years, with sales in 2002 reaching $ 28.8 billion, and expected to rise to $62 billion in 2006 [13]. AMLCDs have seen their share of this market rise from 66 % in 2001, to 76 % in 2002, and this domination is expected to continue for the next few years in a variety of technologies. However, there are a number of research challenges that need to be met if the development of AMCLDs is to continue. One of the most important of these is the increasing desire to manufacture TFTs for large area, low cost substrates.

The production of high quality a-Si:H and gate insulator materials currently requires the use of deposition temperatures greater than 150 °C. The consequence of which is that glass is used as the substrate material for AMLCDs incorporating a-Si:H. Plastic

substrates offer a number of potential advantages over glass. They are cheaper, lighter and have the added benefit of facilitating the development of flexible displays.

Unfortunately, however, decreasing the deposition temperature currently results in a significant degradation in material properties, and consequently device performance Therefore, the real test is to reduce the deposition temperature of a-Si:H, whilst maintaining material quality, to be compatible with the working temperatures of most plastics (< 150 °C).

1.2 OUTLINE OF THESIS

This work is dedicated to the optimisation of a-Si:H deposited by PECVD at deposition temperatures < 150 °C for large area electronic applications. In order to carry out this research, a novel low temperature PECVD reactor incorporating a method for pre-heating of the source gases has been designed and built by the author. This thesis describes the effect of source gas heating on the properties of a-Si:H deposited at low substrate temperatures, and the performance of TFTs incorporating gas-heated material as the active channel layer.

Chapter 2 describes the structure and electronic properties of a-Si:H. This includes details of the band structure and conduction mechanisms, in addition to descriptions of material metastability and the defect pool model. In chapter 3 the structure and operation of a-Si:H TFTs is introduced. Aspects such as instability mechanisms and appropriate electrical contact schemes are discussed, together with the design and fabrication of the TFT structures used in this work. The PECVD technique is described in detail in chapter 4, including the anatomy of RF discharges and the deposition process of a-Si:H. The remainder of the chapter examines the design of the novel PECVD system. Chapter 5 reviews the various physical and electrical characterisation techniques used to investigate the properties of the low temperature a-Si:H manufactured in this work. Also included are descriptions of the electrical testing procedures for the TFTs. Following a discussion of initial system testing, the effect of the various deposition parameters on the properties of a-Si:H are detailed in chapter 6. The optimisation procedure and analysis of the properties of high temperature (300 °C) silicon nitride is described in chapter 7. Chapter 8 describes the performance of

TFTs using gas-heated a-Si:H as the active layer, and compares it to that of devices fabricated with material deposited with the source gas line at room temperature. In chapter 9, the author's main conclusions are outlined and specific suggestions for future research are set out.

Chapter 2

The structure and electronic properties of a-Si:H

2.1 INTRODUCTION

The purpose of this chapter is to summarise the accepted model for the structure of amorphous silicon (a-Si). Details of the role that hydrogen plays in the formation of a-Si:H are given, together with its atomic, electronic and metastable characteristics. In addition, the density of states (DOS) and the effects and mechanism of doping are also discussed.

2.2 ATOMIC STRUCTURE OF A-Si

The disorder of the atomic structure is the main feature that distinguishes amorphous from crystalline materials. In a crystal, the position of the atoms in the lattice is defined by the size and shape of the unit cell, and the position of the atom within it. For crystalline silicon, the unit cell is representative of the entire lattice; thus by repeating the unit cell throughout the entire crystal, the lattice can be generated. This regularity results in well-defined bands of allowed and forbidden energy levels for the electrons, as can be shown from quantum mechanics. The allowed energy states extend over the entire lattice resulting in a high carrier mobility that is only limited by scattering. In amorphous semiconductors, there is no 'long-range' periodicity because the bond angles deviate from the tetrahedral value of crystalline silicon (109.5°), and also due to the variations in bond length, although these materials are not completely disordered. There exists a Continuous Random Network (CRN) in which the short-range order is preserved by the local chemical bonding of the atoms. Consequently, the majority of the silicon atoms are covalently bound to four neighbours, as is the case with c-Si, with the nearest-neighbour environment being determined by the

average bond length and angles. However, not all the silicon atoms in a-Si are four-fold co-ordinated.

In c-Si, defects occur when an atom is missing or displaced in the lattice. This results in either a vacancy, interstitial or dislocation defect. The only structural defect in a CRN is a co-ordination defect, when an atom has too few or too many bonds to satisfy its outer sp3 orbital. These are more commonly known as silicon dangling bonds, and in pure a-Si electron spin resonance (ESR) measurements indicate the dangling bond density to be ~10^{18} cm^{-3} [14]. The variation in the bond lengths and angles results in band tails of localised states into the forbidden or mobility gap – so called, as there is a well-defined gap in which there are no mobile states. The large number of dangling bonds results in localised states around mid-gap [15], which can effectively pin the Fermi level and significantly degrade the electrical and optical properties of the material.

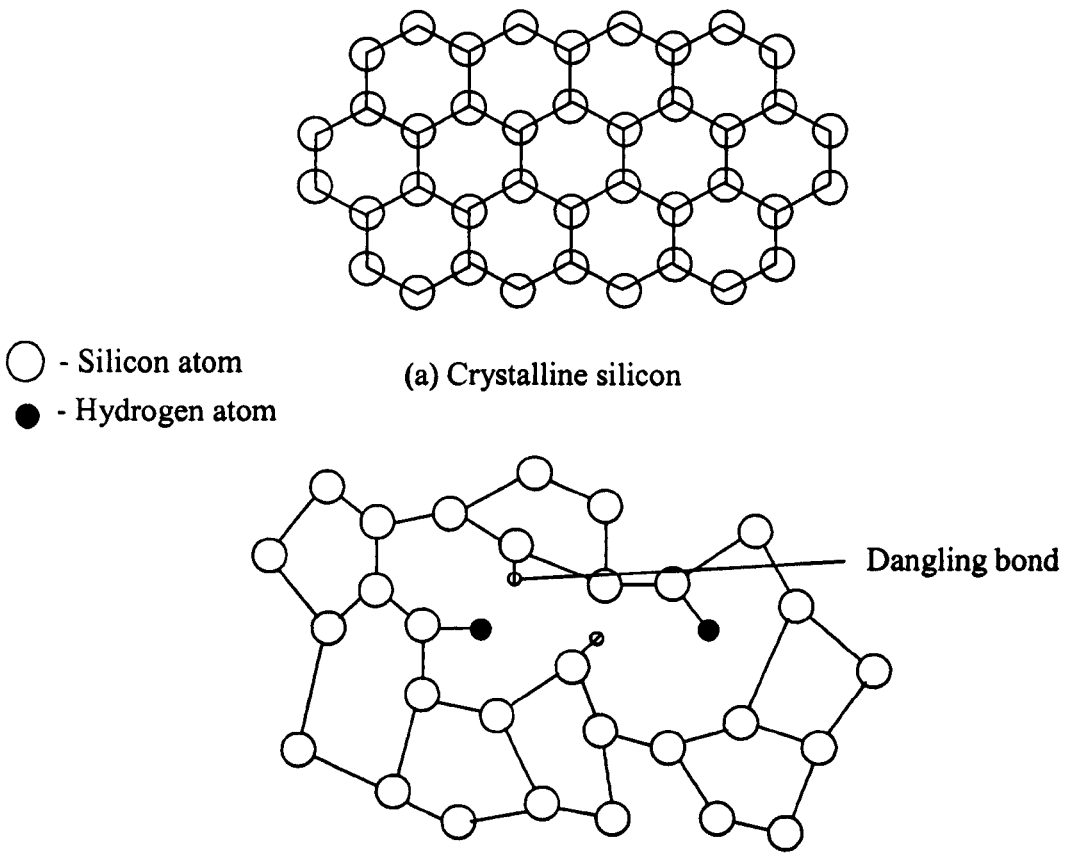

Figure 2.1 Crystalline and hydrogenated amorphous silicon (Each silicon atom has one bond perpendicular to the page)

2.3 THE ROLE OF HYDROGEN

A-Si was intially manufactured by sputtering, electron beam evaporation or Chemical Vapour Deposition (CVD). Later it was shown by Spear and LeComber [16] that a-Si grown by glow discharge decomposition of silane (SiH_4) contained a low density of gap states. This was attributed to the hydrogen atoms binding to the dangling bonds thus rendering them electrically inactive, as the bonded state would be outside the band gap. This process results in the formation of a-Si:H and can reduce the defect density by up to five orders of magnitude. Post-hydrogenation techniques have also been used to improve the quality of a-Si [17]. The consequence of this is that 'device-quality' a-Si:H contains approximately 10 atomic per cent (at%) of hydrogen, which is several orders of magnitude greater than is needed to passivate the dangling bonds in a-Si.

Therefore, the excess hydrogen is alloyed to a-Si and exists in many different bonding configurations (mono-, di-, poly-hydride or poly-silane groups $(SiH_2)_n$). It is thought that these modes relax the overall structure by reducing the ordinarily high levels of average bond strain within the a-Si CRN. With the migration of hydrogen atoms through the amorphous network, the structural constraints of four Si-Si bonds are negated, as silicon atoms are able to form Si-H units together with three Si-Si bonds as a result of a weak Si-Si bond being broken

However, the effects of hydrogen are not always beneficial [18]. The atomic rearrangments caused by the diffusion of hydrogen at moderate temperature (~150-200 °C), can leave behind dangling bonds. Thus, there can be either defect creation or defect removal.

It follows that there is a strict limitation of the possible processing and operating temperatures of a-Si:H devices due to the low thermal stability of the Si-H bond. De-hydrogenation will occur at any temperature above that of the deposition temperature used, and at temperatures above ~ 350 °C significant hydrogen evolution occurs from the CRN of a-Si:H which leads to a severe degradation of the electrical properties.

There is evidence that there are hydrogenated microvoids within the amorphous network [19][20], the size and density of which being dependent upon the deposition conditions. As the void fraction increases, the quality of the material decreases. Device-quality a-Si:H has been shown to have few voids, ~ 1%, with a diameter of ~ 10 Å, whilst poor-quality material can have a void fraction as high as 20% [21]. The surface of these voids is thought to be either partly covered by hydrogen [22] or the voids may be filled with H_2 [23][24]. However, there is much debate and uncertainty about the effect voids have on defect density.

The actual growth processes involved in the deposition of a-SiH by PECVD is of critical importance to the electrical and physical properties of the material and is discussed later (see § 4.3.2).

2.4 ELECTRONIC STRUCTURE OF A-Si:H

A fundamental property of a semiconductor is the presence of a band gap separating the mainly occupied valence band from the mainly empty conduction band states. The well-defined band structure in c-Si is a consequence of the periodicity of the lattice. The valence and conduction bands arise as there are distinct bands of allowed and forbidden states that extend throughout the entire lattice. The high carrier mobility in c-Si is limited only by scattering events within the lattice since the wave functions associated with the free carriers extend throughout the entire volume. The band structures are a consequence of the perfect short and long-range order of c-Si and can be seen in Figure 2.2 (top).

2.4.1 BAND STRUCTURE IN A-SI:H

The principal features of the structure of a-Si:H are the short-range order of the CRN, the long-range disorder and the co-ordination defects. The preservation of the short-range order in a-Si:H results in similar overall electronic properties to those of the crystalline form. However, a tail of states extending into the forbidden gap, which originates from the long-range disorder and electron localisation, replaces the sharp band edges of the crystal. This localisation of the wave function confines the electrons

to a small volume of material rather than the whole lattice. These states are particularly important because electronic transport occurs at the band edge.

The tail states protrude a few tenths of an electron volt (eV) into the forbidden gap, with the valence band tail states resulting from the weak or strained bonding sites, and the conduction tail states resulting from the anti-bonding sites. Davis and Mott [25] have postulated that the electron mobility of each state is very different. Electrons in the tail states must 'hop' from one state to the next that results in a very low mobility, whereas extended state electrons can be thought of as like conduction band electrons in c-Si having a much higher mobility. This then leads to the concept of a mobility gap in amorphous semiconductors, which is analogous to the band gap in a crystalline material. A schematic of the electron density of states (DOS) for a-Si:H can be seen in Figure 2.2 (bottom). E_V and E_C are the lower and upper edges of the mobility gap.

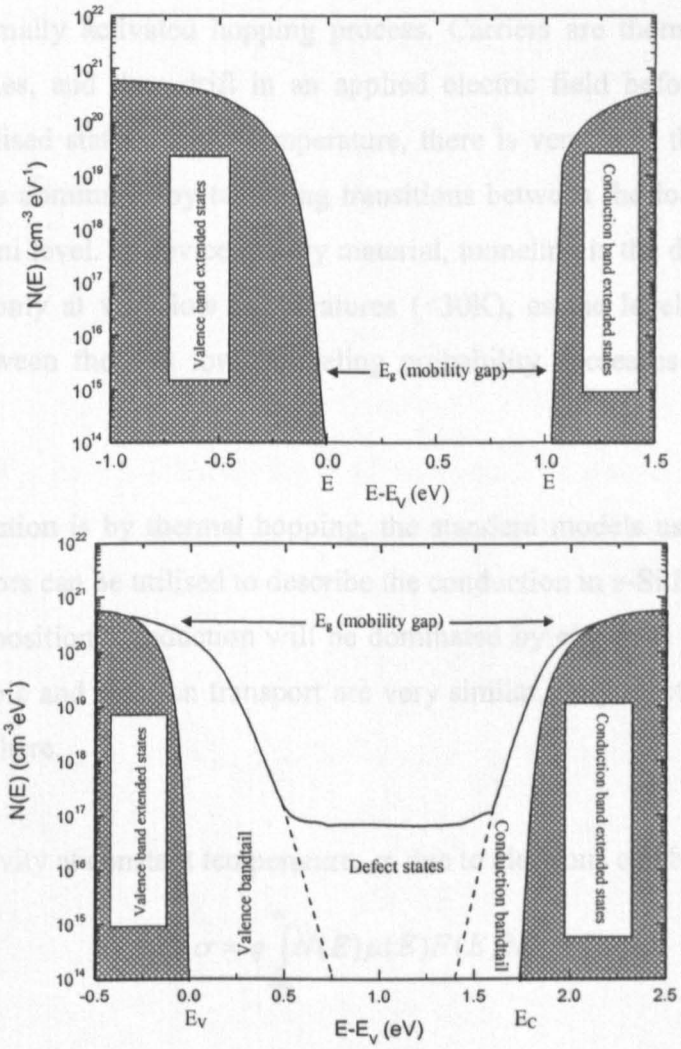

Figure 2.2 Electron density of states (DOS) for (top) crystalline and (bottom) amorphous silicon

The localised levels near the middle of the mobility gap, originating from defects in the CRN, are localised due to their position within the gap and can be split into donor and acceptor bands. These defects ordinarily determine the electronic properties of any semiconductor by controlling trapping and recombination. They also determine the position of the Fermi level, which controls the free carrier concentrations at thermal equilibrium. A-Si:H is in fact slightly n-type as the Fermi level is slightly above mid-gap at ~ 0.8 eV (for intrinsic a-Si:H with a typical optical band gap of ~1.70 eV, as determined by Tauc plot fitting).

2.4.2 CONDUCTION IN A-Si:H

There are three different types of states that facilitate three different modes of electrical conduction i.e. via the extended states, the band tails and the defect states found in the mobility gap. At and above room temperature the conduction mechanism is by a thermally activated hopping process. Carriers are thermally excited to the mobility edges, and then drift in an applied electric field before being trapped in another localised state. At low temperature, there is very little thermal hopping and conduction is dominated by tunneling transitions between the localised defect states near the Fermi level. In device quality material, tunneling is the dominant conduction mechanism only at very low temperatures (<30K), as the level of defects and the distance between them is low (tunneling probability decreases exponentially with distance).

If the conduction is by thermal hopping, the standard models used for conventional semiconductors can be utilised to describe the conduction in a-Si:H. Depending on the Fermi level position, conduction will be dominated by electrons or holes, and as the process of hole and electron transport are very similar, only electron conduction will be described here.

The conductivity at constant temperature, σ, due to electrons can be expressed as,

$$\sigma = q \int_{-\infty}^{\infty} N(E)\mu(E)F(E)\partial E, \qquad (2.1)$$

where N(E) and $\mu(E)$ are the density of states and the mobility at an energy E, $F(E)$ is the Fermi occupation function and q is the charge of an electron.

$$F(E) = \frac{1}{1 + \exp\left(\frac{E - E_F}{kT}\right)}, \tag{2.2}$$

where k is the Boltzman's constant and T is the absolute temperature.

If it is assumed that there is a sharp mobility edge at the conduction and valence band edges [26] and that E_F is approximately mid-gap (i.e. much more than a few kT from the mobility edge), the above equation can be rewritten using the Boltzman approximation,

$$F(E) = \exp\left(\frac{E_F - E}{kT}\right), \tag{2.3}$$

This enables equation 2.1 to be written as,

$$\sigma = q \int_{-\infty}^{\infty} N(E)\mu(E)\exp\left(\frac{E_F - E}{kT}\right)\partial E, \tag{2.4}$$

The extended state conductivity can then be defined if a constant DOS above E_C, ($N(E_C)$), is assumed. The above integral can then be evaluated as,

$$\sigma_{EXT} = qN(E_C)\mu_C kT \exp\left(\frac{E_F - E_C}{kT}\right), \tag{2.5}$$

where μ_C is taken as an average mobility in the extended states and $\mu(E)$ is taken to be zero in the gap.

Equation (2.5) can be rewritten as,

$$\sigma_{Ext} = C\exp\left(\frac{E_0}{kT}\right), \tag{2.6}$$

where, $$C = qN(E_C)\mu_C kT, \tag{2.7}$$

and, $$E_0 = E_C - E_F \tag{2.8}$$

There is evidence that temperature can affect the mobility gap [27] due to the lack of symmetry in the DOS (statistical shift). This also causes the relative position of the Fermi level with respect to the valence and conduction band edges to be temperature dependent. Above 200K optical measurements have shown that this dependence can be described as,

$$E_C - E_V = [E_C - E_V]_{T=0} - \gamma T, \tag{2.9}$$

where γ is the temperature coefficient of the bandgap and has typical values in the range 4-8 x 10^{-4}eVK^{-1}. This shift is a significant correction to the bandgap relative to that at 0K. The value of the correction will be up to 0.12 eV for a Fermi level near midgap at 300K, which results in the observable activation energy being higher than the actual separation of the Fermi level from the mobility edge of the conduction band.

2.4.3 DOPED A-Si:H

It is possible to dope a-Si:H, thus rendering it either n or p-type by adding either phosphine (PH_3) or diborane (B_2H_6) to the source gases during deposition. Spear and LeComber first described how the addition of small quantities of dopant results in a decrease in the activation energy [3]. These decreases are directly attributable to shifts in the Fermi level, rather than any changes in the bandgap; and the energy states of the dopants lie mostly within the existing band tail states and do not alter the band edges.

This doping phenomena is interesting and important, as it might seem logical to assume that an amorphous network could satisfy the valence requirements of any atom, as there are no lattice constraints similar to those in crystalline semiconductors. This directly contravenes Mott's 8-N rule [28]: in an amorphous network, the number of covalent bonds, Z, which an atom can form should be Z = N for atoms with valence N<4, and Z = 8-N for N≥4.

Several theories have been put forward to explain the doping effects in a-Si:H. The first was by Adler [29]. He proposed that doping could only occur in the presence of a defect, which lowered the formation energy of the dopant state. It was then thought that the formation of charged defects was a direct result of the doping mechanism, as it had been widely observed experimentally that defect concentration increases with doping levels [30][31][32]. A further extension proposed that defects and dopants did not need to be spatially correlated [33]. This meant that defects could be formed via a process of weak Si-Si bonds being broken in the presence of free carriers. For example, the results of defect-dopant reactions for phosphorous and boron would be:

Dopant reaction	***Defect reaction***	
$P_3^0 \Leftrightarrow P_4^+ + e$	$Si_4^0 + e \Leftrightarrow Si_3^-$	(2.10)
$B_3^0 \Leftrightarrow B_4^- + h$	$Si_4^0 + h \Leftrightarrow Si_3^+$	(2.11)

As the above reactions involve charged species, the formation energies and equilibrium constants will be Fermi level dependent. This means that the effect of the Fermi level on dopant activation is opposed by the effect of the defect reaction: both reactions are interdependent.

If the example of n-type doping is considered (2.10), with no defect reaction occurring, the equilibrium of the dopant reaction would be shifted far to the left because the Fermi level would soon rise making further dopant activation energetically unfavourable. However, the defect reaction, which is made energetically favourable by a raised Fermi level, removes excess band-tail carriers that are generated by the dopant reaction and the Fermi level is lowered. This then forces the dopant reaction to the right producing more active dopant states. Therefore, the net result of the two reactions is an upward shift in the Fermi level, an increase in the defect density and the activation of a proportion of the dopant atoms. This defect-dopant process (for n-type doping) is shown diagrammatically in Figure 2.3.

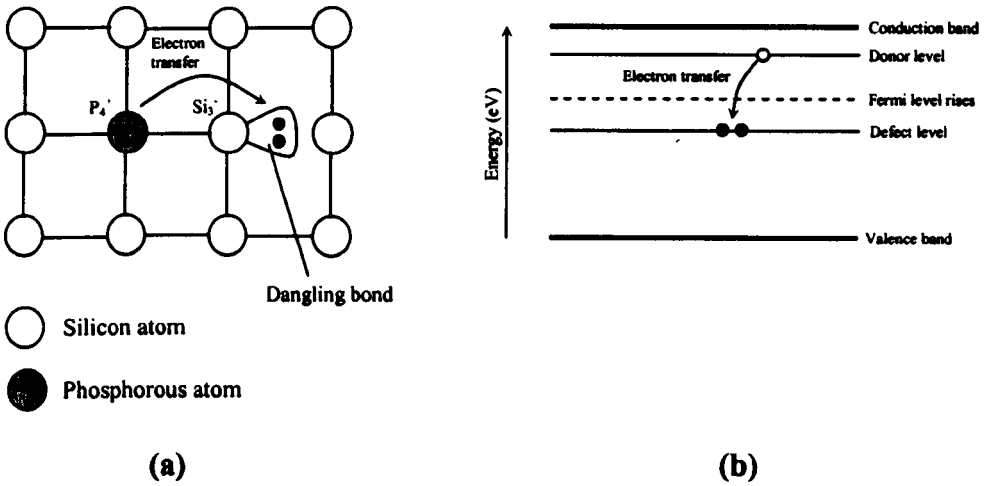

(a) (b)

Figure 2.3 The doping mechanism in a-Si:H using n-type doping with a phosphorous atom as an example. (a) An activated phosphorous atom donates an electron to a nearby neutral dangling bond. (b) This raises the Fermi level towards the conduction band

However, not all of the (in this case) phosphorous atoms contribute to the active doping of the a-Si:H material since the P_4 state is at a higher energy level than the ideal P_3 state. This leads to a dopant activation efficiency, η_d, given by the following [34],

$$\eta_d = \frac{[P_4^+]}{[P_3^0]} \tag{2.12}$$

where P_4^+ is the concentration of active dopants and P_3^0 is the total concentration of dopants. For phosphorous in a-Si:H this is found to be ~ 1%.

When both n and p-type dopants are present, as is the case with compensated material, the overall defect density is lower and the band edges are broadened. There is also direct recombination of the holes and electrons produced in (2.10) and (2.11). In addition, the positively and negatively charged defects recombine to allow for defect neutralisation to occur.

Thus, we see that the doping mechanism of a-Si:H is fundamentally different to that of c-Si. In c-Si the dopant atoms can only bond in the four-fold configuration, and as

has been shown, in a-Si:H the dopant impurities can only bond if there is a compensatory dangling bond created simultaneously (a negative or positive dangling bond depending on whether the dopant is question is n or p-type).

2.5 THE METASTABILITY OF A-SI:H

Metastability is a reversible change in the density of electronic states caused by an external electronic excitation, such as light illumination. The first metastable change in a-Si:H was reported by Staebler and Wronski [35], who found that the dark conductivity decreased by up to four orders of magnitude with an additional shift in the activation energy from 0.57 eV to 0.87 eV, when an a-Si:H sample was illuminated by intense light. The observed effect was found to be reversible by annealing the a-Si:H at temperatures ≥150 °C. The experimental cycle was repeated many times and it was found that there was no observable degradation of the sample. This phenomenon was named the Staebler-Wronski effect (SWE) and was attributed to a reversible increase in the number of dangling bond defects in the mobility gap, which in turn leads to a downward shift in the Fermi level, hence the increase in the activation energy.

It has been shown that any changes in the free carrier density lead to reversible changes in the mobility gap DOS [36]. Moreover, the mobility gap DOS has been found to depend on the previous 'thermal history' of the material [37]. Consequently, any movement of the Fermi level position due to state creation is obviously of fundamental importance for the operation of electronic devices. All devices that incorporate a-Si:H technology (TFTs, solar cells etc.) operate on the basis of an externally induced shift in the Fermi level. Therefore, the metastable creation of defects during device operation and thermal processing can cause degradation of the device characteristics, which is a serious technological problem that must be considered.

2.5.1 METASTABLE STATE CREATION

Many different models have been proposed to describe the cause of the metastable

phenomenon in a-Si:H. Most attribute the effect to the diffusion of hydrogen through the CRN, which is accompanied by the breaking of weak Si-Si bonds [38][39][40]. Stutzmann et al [41] have proposed that photogenerated charge carriers non-radiatively recombine at weak Si-Si bonds. The release of this recombination energy can be used to break the bond, and thus two dangling bonds are formed. These are prevented from recombining by the passivation of a hydrogen atom from an adjacent site. However, recent ESR measurements appear to contradict the local nature of most models, describing the lack of a close spatial correlation between the presence of hydrogen and light induced dangling bonds [42].

The SWE has been found to depend on the bonded hydrogen configuration with the CRN of a-Si:H. The density of metastable defects is determined by the amount of hydrogen bonded in the monohydride configuration [43]. In addition, the presence of clustered hydrogen is thought to lead to faster defect creation kinetics [44][45]. A model has been proposed by Branz that describes the kinetics of the SWE [46].

When mobile H atoms generated by excess carriers collide, they form metastable, immobile complexes containing two Si-H bonds. The defects associated with the SWE are left behind on the sites from which the colliding H were excited. The mobile H atom has been viewed as a mobile complex of an Si-H bond and a dangling bond [47]. This complex moves through the amorphous network, breaking one Si-Si bond after another, but each bond then reforms after the complex has passed it. The complex becomes immobile when one dangling bond meets another and they then annihilate to form a Si-Si bond. The H atom is then immobilised as Si-H. This way, the number of dangling bonds is conserved as one immobile dangling bond is created at the site of the H excitation and another is annihilated at the site of H retrapping. However, it has been found that there is no experimental evidence for mobile bonds. Indeed, defect diffusion, which includes floating bond diffusion, is less pronounced than hydrogen diffusion [48]. Powell et al [49] have proposed a model that short, weak bonds are a very likely precursor for defect creation. This local model involves hydrogen motion over relatively short distances. The hydrogen atom is at the tetrahedral site of a broken, weak Si-Si bond and the dangling bond is on the other Si atom. The separation of the dangling bond and the hydrogen atom is thought to be 4-5

Å, which leads to a model that involves few bonding rearrangements in a relatively small local volume.

A connection between the SWE and hydrogen diffusion has long been suspected [50], due to the fact that at temperatures commensurate to those utilised to anneal out any metastable changes (between 150 °C and 250 °C), hydrogen is known to diffuse quite readily through the a-Si:H material [51]. In addition, Jackson et al [52] have shown from bias-stressing experiments on TFT and MIS structures that metastable defect kinetics, as a function of time, temperature and carrier concentration are in qualitative agreement with models that envisage hydrogen motion (i.e. hydrogen is involved in many of the metastable processes observed in a-Si:H).

2.5.2 METASTABLE CHANGES IN DOPING EFFICIENCY

The thermal equilibrium of doped a-Si:H involves both the defects and the dopant sites and is governed by the position of the Fermi level at equilibration (i.e. the restoration of equilibrium after excitation by an external source such as illumination). Therefore, metastable changes in the defect and dopant densities are expected as a result of equilibrium disruption.

Rapid thermal quenching experiments have shown that dopant activation can be varied in grown samples of a-Si:H [53]. By quenching samples of n or p-type a-Si:H from elevated temperatures at different rates, varying activation energies can be achieved. Indeed, fast cooling ($> 1 Ks^{-1}$) results in a lower activation energy than slow cooling ($< 0.1\ Ks^{-1}$). This was found to be due to the presence of more active dopants in rapidly cooled samples rather than any significant change in the number of defect states. If it is assumed that the energy required to activate a dopant is positive, at higher temperatures a larger fraction of dopant sites have sufficient energy to become active. Consequently, if these sites are cooled quickly enough, they do not have enough time to relax, which effectively freezes the increased concentration of active dopants into the a-Si:H material. This dopant distribution will slowly decay towards the equilibrium distribution at room temperature.

Therefore, above a particular temperature, T*, doped material remains in thermal equilibrium for normal experimental timescales. Below T* however, the equilibration time for the material becomes longer than standard experimental timescales. The value T* has been found to be 200 °C for intrinsic a-Si:H, ~ 130 °C for n-type material and ~ 90°C for p-type material [53].

In addition to altering the dopant activation of a grown sample of a-Si:H by rapid thermal quenching, other workers have explored whether this same phenomena can be achieved by altering the position of the Fermi level. Charge sweep out measurements were carried out on structures that incorporated a channel layer lightly doped with phosphorous [54][55]. This technique measures the density of band tail electrons, which is assumed to approximately equal the active dopant density. By annealing the device when a depletion bias was applied (i.e. one which lowers the Fermi level in the doped material), it was found that the charge swept out had increased. These results suggested that there had been increased dopant activation. In line with this observation was the fact that the conductivity had increased and the activation energy had decreased after the bias anneal.

A further method was proposed for moving the Fermi level in doped samples of a-Si:H that involved varying the activation energy of conduction by applying a negative or positive gate bias, to either lower or raise the Fermi level near to the interface [31]. A TFT structure was rapidly quenched after being subjected to an anneal with a gate bias applied. The conduction activation energy was then measured without a gate bias. These experiments revealed that the activation energy of conduction could be varied between 0.11 and 0.59 eV. The results were interpreted as an increase in doping efficiency as the changes in defect densities (as measured by sub-bandgap absorption), were too small to account for the range of activation energies achieved.

The extra dopant activation outlined above was found to slowly decay back to the original activation levels at equilibrium over long periods of time.

2.5.3 METASTABLE DEFECTS INDUCED BY PARTICLE BOMBARDMENT

Work carried out that involved the effect of charged particle bombardment on defect

creation, found that any defects created are not induced by a shift in the Fermi level position, but by atomic impact, which breaks bonds and displaces atoms [56]. The equilibration of the dangling bonds takes place in much the same way as defects induced by device stressing, and the results have been explained in terms of hydrogen diffusion through the network as discussed earlier.

2.5.4 THE DEFECT POOL MODEL

The defect pool model (DPM) is essentially a tool that facilitates the calculation of the defect densities in a-Si:H. The fundamental result of this model is that the energy spectra of the defects depend on the position of the Fermi level at equilibrium.

It was first proposed by Bar-Yam et al [57] who noted that the formation energy of a defect depends on the charge state, it's position in the bandgap, and the Fermi energy. This work was then extended by Smith and Wagner, and subsequently by Winer [58][59]. However, perhaps the most comprehensive model is that proposed by Powell and Deane [60]. The results from the bias stressing and bias annealing experiments they carried out on a-Si:H TFTs were in excellent agreement with the theoretical prediction of the DPM. They then developed the theory further by combining predictions of the DPM and a hydrogen density of states (HDOS) model in order to produce a unified picture that explains a wide range of phenomena [61]. It was postulated that it was necessary to include a hydrogen mediated defect creation process to account for experimentally measured defect densities.

Due to the many different local environments within the a-Si:H network, there is a range or pool of potential energies throughout the bandgap at which the dangling bonds can form, but only those defects with the lowest formation energy actually form. The formation energy of a defect depends on the position of the Fermi level during equilibration. If the Fermi level is raised into the conduction band tail-states (electron accumulation), then the formation energy of negatively charged dangling bonds in the lower bandgap decreases, which leads to a peak in defect density in that area. In the opposite case (when the Fermi level is lowered into the valence band tail states), more defects form in the upper bandgap. The formation energy is calculated from the difference between the valence band tails states (the weak bonds) and the

energy of the dangling bond state [62]. This is illustrated by the configuration coordinate diagram shown in Figure 2.4.

The weak Si-Si bond (WB) state is converted to a dangling bond (DB) when the barrier is crossed from left to right with the energy required for this process being given by Φ_1. The dangling bond is either positively or negatively charged depending on whether the states are created under electron or hole accumulation. To anneal out the defect, energy Φ_2 is necessary. The offset of these two energy wells is the formation energy Φ_{form}. The rate of creation of dangling bonds is dependent upon the density of the weak bond states, the number of carriers and the barrier to formation.

The equilibrium between the weak Si-Si bond states in the valence band tail and excess carriers determines the defect density. At elevated temperatures (~ 220 °C), this equilibrium is established within a few minutes [60], but as the sample is cooled, the rate of equilibration reduces dramatically and the dangling bond density becomes 'frozen' into the sample.

At room temperature, the dangling bond density is modified very slowly and only by prodigious and prolonged increases in carrier density.

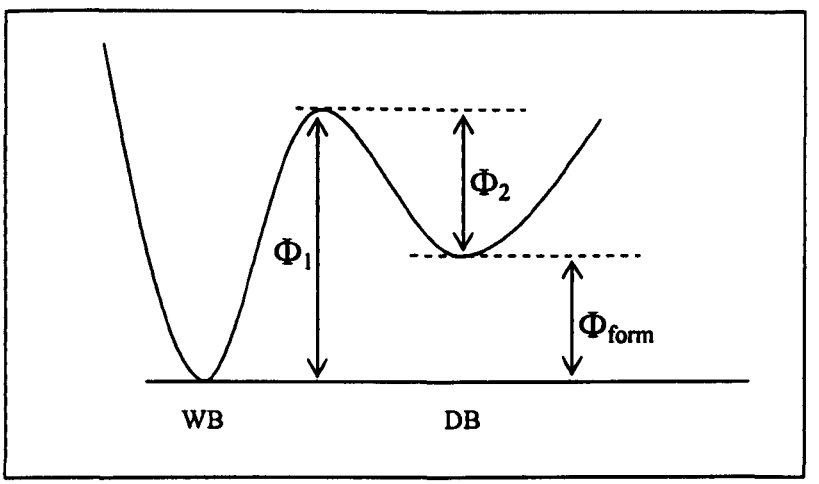

Figure 2.4 Configuration coordinate diagram showing weak bond/dangling bond conversion

Understanding the physical processes taking place during TFT operation is of fundamental importance for device optimisation. As a result of studying the nature of metastabilities within a-Si:H, it is possible evaluate the degradation in performance (the rate of turn on/off and the threshold voltage shift), as state creation is the major cause of instabilities within device grade TFTs [63].

Chapter 3

The Structure and electronic properties of a-Si:H TFTs

3.1 INTRODUCTION

In this chapter the thin film transistor (TFT) is introduced. The origin and principle of the field effect transistor is outlined, together with the structure and operation of a-Si:H TFTs. The theory and operation of a simple c-Si MISFET is summarised and equations detailing the relationship between device performance and structure, and material properties are defined. In addition, various TFT technologies are discussed and a section describing instability mechanisms is also included

3.2 BACKGROUND TO TFTs

The principle of the field effect transistor was first proposed around 1930 [64][65]. Then in 1960, Khang et al [66] proposed the first metal-insulator-semiconductor field effect transistor (MISFET). The first thin film transistor was reported by Weimer [67] and consisted of thermally evaporated layers of silicon monoxide and microcrystalline cadmium sulphide onto insulating substrates. TFT operation is similar to that of a conventional MISFET, i.e. turn-on is achieved by the application of an above-threshold voltage to the gate contact.

TFTs have been developed with a variety of semiconducting layers: Cadmium Selenide, Tellurium and Lead Telluride [68][69][70], but problems associated with uniformity and stability led to the investigation of other materials. A number of silicon-based technologies have also been developed that include polycrystalline silicon (poly-Si) and laser-recrystallised silicon [71][72], but these materials cannot yet be fabricated effectively over large areas. Whereas, a-Si:H has the advantage of being a low temperature, large area technology that is compatible with cheap glass,

and more recently plastic or polymide, substrates. The information that can be gleaned from the extensive deposition and processing experience developed for Si-based technologies, means that a-Si:H is the predominant semiconducting material used in large area electronic applications.

The first a-Si:H TFT was first proposed by Spear and LeComber [2] in 1972 in order to investigate the DOS in a-Si:H using the field effect technique. However, the design of an insulated-gate FET suitable for display applications was not published until 1979 [73]. This device used silicon nitride as the gate insulator, which was sequentially deposited with the a-Si:H layer by Plasma Enhanced Chemical Vapour Deposition (PECVD), onto Corning 7059 glass substrates. Subsequent work has resulted in a-Si:H TFTs being used in many other applications (§ 1.1).

To fully understand the nature of a-Si:H TFTs, a thorough understanding of the basic physics of operation and performance is essential. This is the aim of this chapter.

3.3 OPERATION OF THE METAL-INSULATOR-SEMICONDUCTOR FIELD EFFECT TRANSISTOR (MISFET)

The structure of a typical n-channel MISFET can be seen in Figure 3.1. The p-type crystalline silicon substrate has two strongly n-type regions that are diffused or implanted. These are labelled source (S) and drain (D). The metal gate contact (G) is separated from the surface of the c-Si surface by a thin insulating layer of thickness (d_{IN}). Without any applied voltage to the gate, little current can flow between the source and the drain because the structure corresponds to two p-n junctions in series. Therefore, the only current that can flow is the leakage current. When a sufficiently large positive bias (V_G) is applied to the gate, negative charges are induced in the semiconductor at the insulator surface. This forms a depletion region and a thin surface region that contains mobile electrons. The induced electrons form what is known as the channel of the FET, which has a length (L) and a width (W). The electrons then experience a drift from the source to the drain under the application of a drain-source voltage (V_D), that results in a drain-source current (I_{DS}). Varying the gate bias can then modulate the conductance of the channel. This alters the number of

charge carriers that are able to contribute to conduction. As only one type of carrier is involved in the conduction mechanism, these devices are called unipolar.

The minimum voltage required to induced the channel is called the threshold voltage (V_T), and therefore, for an n-channel device the gate voltage must be more positive than a value V_T before a channel can be induced. Ideally, when no voltage is applied, the energy bands are flat at the interface between the insulator and the semiconductor. However, once the insulator fixed charge (Q_F), mobile charge (Q_M), surface or interface states (Q_{SS}) and metal-insulator work function difference (ϕ_{MS}) are taken into account, some band bending occurs at the interface when there is zero applied gate bias. Consequently, to achieve threshold the applied gate bias must be large enough to firstly facilitate the flat band condition, then accommodate the charge in the depletion region and ultimately induce the channel itself.

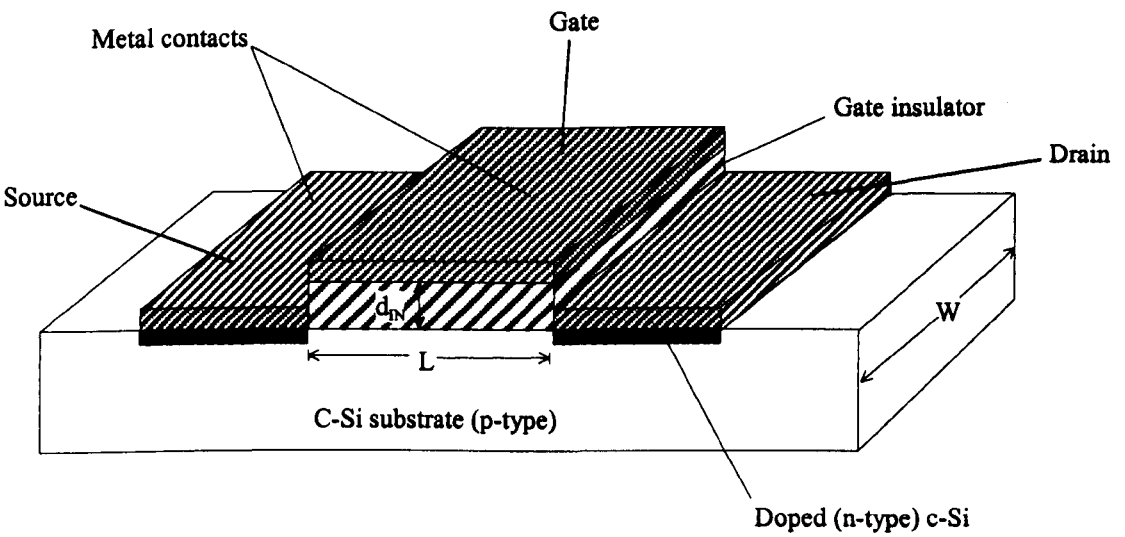

Figure 3.1 N-channel c-Si MISFET

For low drain-source voltages and when $V_D << V_G - V_T$, the channel will act like a resistor. This is known as the linear region, and I_{DS} can be defined as,

$$I_{DS} = \mu_C \frac{W}{L} C_{IN} (V_G - V_T) V_D \quad , \tag{3.1}$$

where $$C_{IN} = \frac{\varepsilon_{IN}}{d_{IN}}, \tag{3.2}$$

$$V_T = V_{FB} + 2\phi_B + \frac{\sqrt{2\varepsilon_S q N_A (2\phi_B)}}{C_{IN}}, \tag{3.3}$$

and $$V_{FB} = \phi_{MS} - \frac{Q_F + Q_M + Q_{SS}}{C_{IN}}, \tag{3.4}$$

Here μ_C is the electron mobility in the channel ε_{IN}, the permittivity of the insulator and C_{IN} is the capacitance of the gate insulator

As the drain voltage is increased, there is a point at which the drain current becomes saturated and remains essentially constant. The potential difference between the gate and the inversion layer near the drain end decreases until it falls below the value that is required to maintain an inversion layer, and the channel depth reduces to zero at the drain end. The number of carriers arriving at this point from the source, and hence the current flowing from the drain to the source, remains the same. This is known as the pinch-off point and $V_D = V_{sat}$. Therefore for $V_D \geq V_{sat}$, the drain current I_{DS} can be described as:

$$I_{DS} = \mu_C \left(\frac{W}{2L}\right) C_{IN} (V_G - V_T)^2 \tag{3.5}$$

3.4 THE STRUCTURE AND OPERATION OF A-Si:H TFTs

Essentially there are four types of planar TFT that are defined by the order of the deposition of the semiconducting layer, the gate insulator layer, the source-drain contacts and the gate electrode (see Figure 3.2). The staggered TFT structures have the source and drain contacts on the opposite side of the semiconductor to the gate electrode, whereas the coplanar have all three electrodes on the same side of the

semiconductor film. For inverted structures, the gate electrode is the first layer to be deposited.

The most popular design of a-Si:H TFT is the inverted-staggered structure. In the inverted-coplanar configuration the gate insulator must be exposed to processing steps before the active layer is deposited, which can lead to a degradation in the interface between the insulator and the active region. Similarly, top gate structures tend to have poor characteristics due to the low quality interface between the insulator layer and the a-Si: H [74].

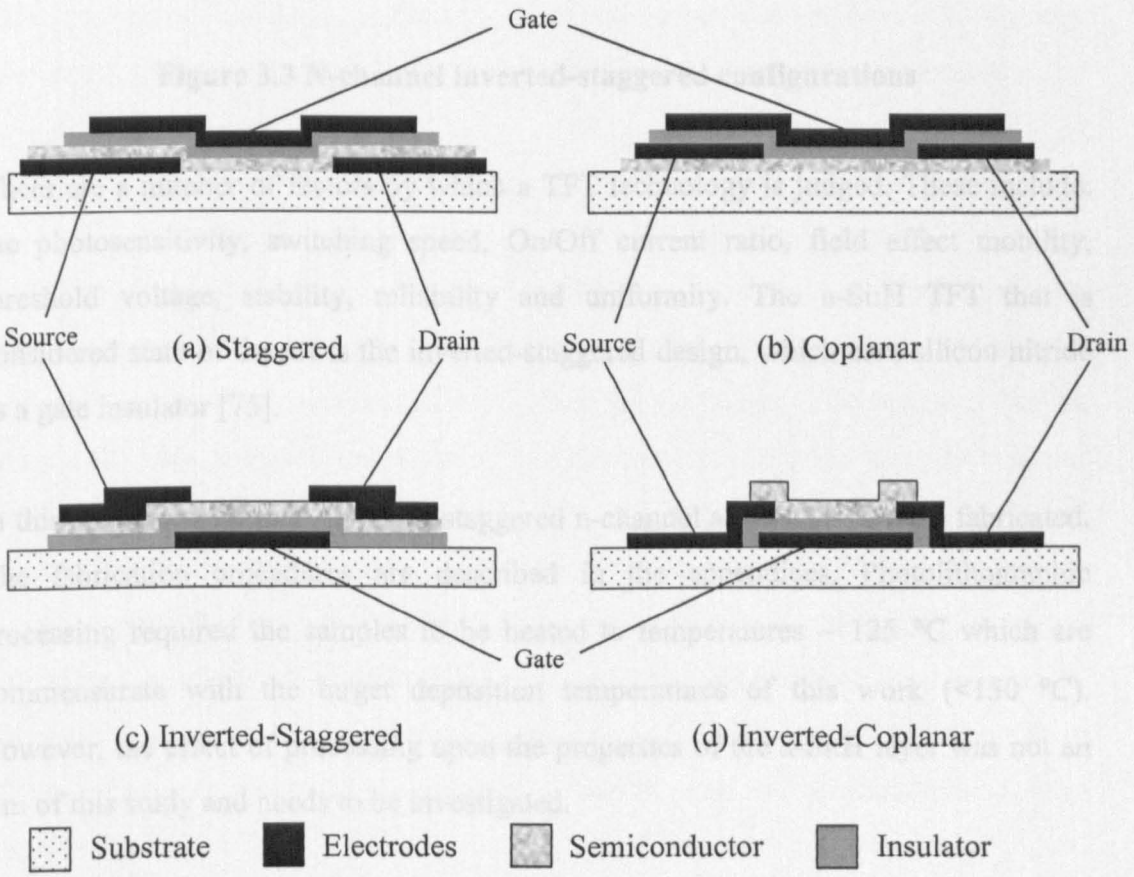

Figure 3.2 Various TFT structures

Inverted-staggered TFTs can be split into two further categories: passivated and unpassivated (see Figure 3.3). A passivated structure includes the deposition of an insulator on top of the active layer. Holes are then opened up in the insulator before the deposition of the doped layer.

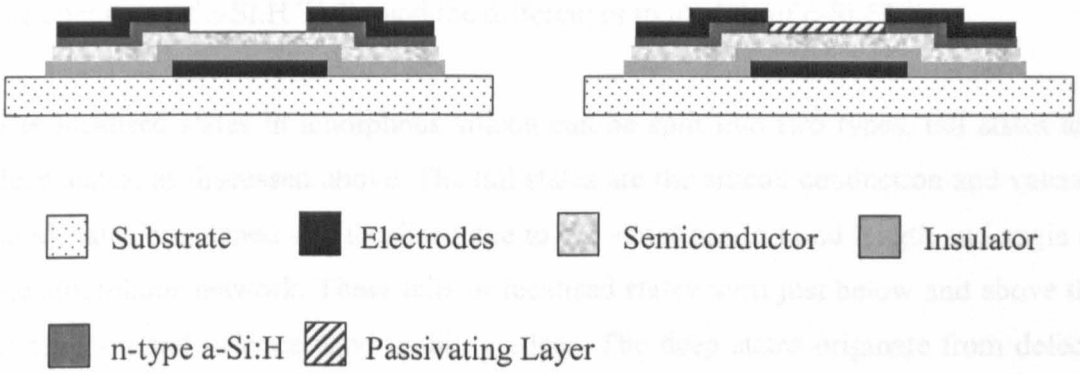

Figure 3.3 N-channel inverted-staggered configurations

There are a number of factors by which a TFT technology is judged. These include: the photosensitivity, switching speed, On/Off current ratio, field effect mobility, threshold voltage, stability, reliability and uniformity. The a-Si:H TFT that is considered state of the art is the inverted-staggered design, which uses silicon nitride as a gate insulator [75].

In this work, bottom gate, inverted-staggered n-channel a-Si:H TFTs were fabricated. The fabrication procedures are described in the appendices. Photolithographic processing required the samples to be heated to temperatures ~ 125 °C which are commensurate with the target deposition temperatures of this work (<150 °C). However, the effect of processing upon the properties of the a-Si:H layer was not an aim of this study and needs to be investigated.

3.4.1 THE OPERATION OF A-Si:H TFTs

In the case of c-Si field effect transistors (FET), when a bias is applied that is above that of threshold, nearly all of the charge induced in the channel appears in the conduction band extended states. This is due to the source-drain channel being formed by inversion and virtually all the localised states being filled. As a result, the Fermi level is near to the conduction band edge. When an a-Si:H TFT is turned on, it is only the carriers at the semiconductor/insulator interface that contribute to conduction. This

is a consequence of the high densities of localised states both within the bandgap and bandtails. The effect of the DOS distribution of a-Si:H is important in understanding the operation of a-Si:H TFTs, and the differences to models of c-Si FETs.

The localised states in amorphous silicon can be split into two types, tail states and deep states, as discussed above. The tail states are the silicon conduction and valence band states broadened and localised due to the variations in bond length and angle of the amorphous network. These tails of localised states form just below and above the conduction and valence band mobility edges. The deep states originate from defects within the network and consist mainly of dangling bands, and can have a broad range of energies that result from the wide variation in the local bonding environment.

The nature of the localised states is significant as they determine the characteristics of any device. In n-channel devices the acceptor-like localised states located in the upper half of the bandgap determine device characteristics, where donor-like states in the lower part of the energy gap will dominate p-channel devices. In addition, in modelling the transfer characteristics of a-Si:H TFTs, it cannot be assumed that the density of states is homogenous throughout the material [75] and there is evidence that the density of states is indeed lacking in homogeneity [76]. Initial models of the a-Si:H DOS did in fact assume a uniform distribution of localised states throughout the bandgap [77][78] and the role of the tail states was extensively described [79][80][81]. Later work postulated an exponential variation in both the deep and the tail states with a steeper exponential describing the tail distribution [82]. The effects of device structure, temperature and material properties on device characteristics were also discussed.

However, the effects of both bulk and surface states should be taken into account for an accurate model of a-Si:H TFTs. Moreover, the surface states and fixed charge at the a-Si:H interface with the gate insulator should also be included [83][84][81]. A modelling method that included the use of an inhomogeneous DOS was first proposed by Deane and Powell [85]. They developed a computer program that analysed field-effect measurements and incorporated a defect pool model of the DOS. This work succeeded in explaining a number of a-Si:H TFT characteristics (subthreshold slopes, apparent flat band voltages and activation energies of conduction) in relation to a

spatially inhomogeneous DOS. With reference to the information outlined previously, it is possible to describe the basic principles of a-Si:H TFT operation. This is illustrated using a simple DOS distribution and schematics of band-bending and the occupancy of the electronic states.

At zero gate bias the energy bands are close to the flat band condition, as is shown in Figure 3.4. In practice, the combined effects of the insulator fixed charge, surface states and metal-semiconductor work function difference will result in some band bending at zero applied bias. The TFT is said to be in the 'Off' state, and this is known as the subthreshold regime. The value of the TFT 'Off' conductance is dependent upon the position of the Fermi level, the DOS at the Fermi level in the bulk, and the interface with any channel passivation layer. Without any fixed charge or interface passivation interface, the 'Off' conductance is defined simply by the position of the Fermi level in the bulk.

When a positive gate voltage is applied, that is less than threshold, the energy bands bend downwards at the interface and the Fermi level moves through the occupied deep states. The concentration of mobile carriers in the conduction band tail rises as the Fermi level moves closer to the conduction band mobility edge, but the occupancy of these states low. Therefore, the total space charge is dominated by the deep states. The source-drain current arises from the small number of electrons excited from the Fermi level into the localised bandtails at the conduction band edge.

The space charge in the deep states increases proportionally with the gate bias. Concurrently, as the band bending increases the current increases exponentially.

The subthreshold region is spread over a larger gate bias range for an a-Si:H TFT than for a c-Si MOSFET. This is because the Fermi level needs to be moved through a substantial density of localised states. The result of the increased defect density is that the speed of 'turn on' is reduced. In essence, a larger voltage is required to turn the device on because the defect states in the gap must be filled before the accumulation of the mobile carriers in the channel can take place.

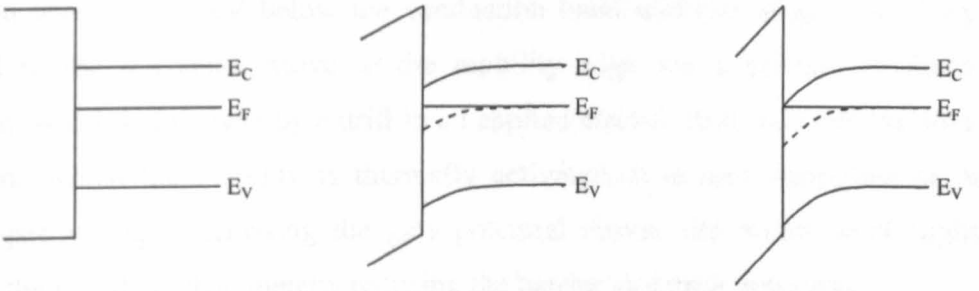

(a) $V_G = V_{FB}$ (b) $V_G < V_T$ (c) $V_G > V_T$

Band bending profiles

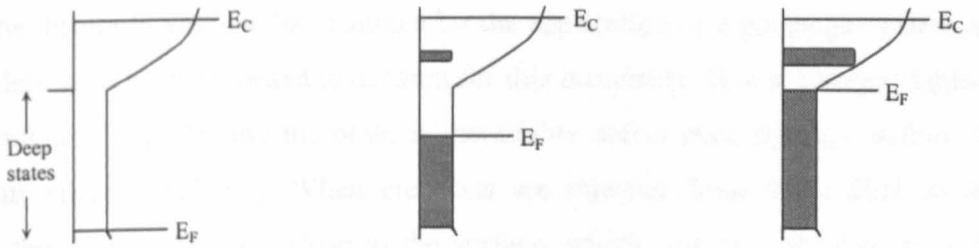

(a) $V_G = V_{FB}$ (b) $V_G < V_T$ (c) $V_G > V_T$

Occupancy of States

Figure 3.4 The basic operation of an a-Si:H TFT showing the band bending and the occupancy of states

As the device turns on and the gate bias increases above threshold, it will act like a voltage-controlled resistor. Any additional charge induced in the a-Si:H at the interface occupies the tail states and the shape of the conduction band tail governs the performance of the device. The space charge in the bandtail exceeds that of the deep states, and the Fermi level is below the tail states. At this point, both the total space charge and the source-drain current increase linearly with applied gate voltage hence this is the known as the linear regime. Using MISFET theory, device parameters such as threshold voltage and field effect mobility can be calculated.

The Fermi level cannot reach the conduction band edge due to the high density of localised states. Therefore, the high density of carriers needed to fill these states pins the Fermi level ~ 0.15 eV below the conduction band mobility edge. The charges localised in the tail states move to the mobility edge via a process of thermal activation, which is followed by a drift in an applied electric field between the source and drain. Whilst the mobility is thermally activated, it is also dependent on the applied gate voltage. Increasing the gate potential moves the Fermi level slightly closer to the mobility edge, thereby reducing the barrier to carrier activation.

3.5 INSTABILITY OF A-Si:H TFTs

There are inherent instabilities in a-Si:H TFTs. The most important of which is the shift in the threshold voltage that occurs after the application of a prolonged gate bias. Two models have been proposed to account for this instability. One is charge trapping in the insulator [86][87], and the other is metastable defect state creation within the amorphous silicon [88]-[91]. When electrons are injected from the a-Si:H to the insulator they can be trapped close to the surface, which results in a layer of fixed charge. This layer, Q_F, reduces the charge induced in the a-Si:H and the transfer characteristic shifts by an amount equal to Q_F/C_G, where C_G is the gate capacitance.

The injection process can occur by direct tunnelling from states in the semiconductor to traps in the insulator, which gradually fill from the surface [92]. The injection mechanism itself is weakly temperature dependent [93], but any temperature dependence is derived from the density of free carriers available for injection.

The second mechanism responsible for stability problems is the creation of defect states within the a-Si:H. The proposed model explaining this phenomenon is that Si dangling bonds are created by breaking weak Si-Si bonds, which are then stabilised by the diffusive movement of hydrogen [94]. This process has similarities to the Staebler-Wronski effect where states are created as a result of illumination. It has been found that the pre-threshold slope of the transfer characteristic of n-channel transistors does not change after prolonged bias stress. Therefore, the newly created defect states must be located below the flat band position of the Fermi level. This result supports the theory of the defect pool model outlined previously, i.e. under

positive bias stress, the interfacial Fermi level in the a-Si:H is raised above its equilibrium position and dangling bonds are created deep in the gap. It has also been demonstrated experimentally by measuring the effect of positive and negative stressing on the pre-threshold slopes of n- and p-channel devices [95]. Consequently, the creation of states in this position will shift the Fermi level nearer to midgap, which accounts for the shift of the electron threshold voltage.

The bias dependence of each instability mechanism has been investigated and the threshold voltage shift increases slowly with bias up to some critical voltage (V_{GC}), and then increases rapidly thereafter [96][97]. For applied biases below V_{GC} the threshold voltage shift is mainly due to state creation, whilst above V_{GC} charge trapping in the insulator is the dominant instability mechanism.

3.6 ELECTRICAL CONTACTS TO A-Si:H

To understand device performance, and the effect of a-Si:H material deposited at low temperatures on device characteristics, it is important to have electrical contacts of sufficient quality. This means that they should be sufficiently ohmic to allow a significant 'On' current at low source-drain voltages [76]. If the contacts are non-ohmic, current crowding can result which can increase the series contact resistance thereby causing the current-voltage characteristics to be non-linear. These resistances exist because current must flow from an n^+ contact, across the intrinsic a-Si:H layer to the conducting channel at the a-Si:H/insulator interface, before flowing along the channel and back across the intrinsic layer to the other n^+ contact.. This can lead to an alteration of device parameters such as a decrease in the field effect mobility and an increase in threshold voltage. In addition, the total contact resistance must be lower than the total channel resistance. If this isn't the case, the 'On' current will be limited by the contacts, and a change in the linear region transfer characteristics will be exhibited. A good way of reducing series resistance effects (i.e. contact resistance plus the bulk resistance of the intrinsic a-Si:H layer) is to select a TFT structure with a channel length that is larger than the thickness of the a-Si:H layer and to use highly injecting large areas contacts. The series resistance then becomes negligible relative to the channel resistance and can therefore be ignored.

Current crowding can still occur even if there are good ohmic contacts. The resistivity of intrinsic a-Si:H is of the order of 10^{10} Ωcm, which would be too high for the required device performance. However, it has been shown that this resistance is actually several orders of magnitude less [98]. This is because the injected carriers initially fill the available trapping sites in the a-Si:H material, which reduces the trapping probability for any excess electrons. But, if the bulk DOS is very high, current crowding can still be a problem as a result of the high trap density, regardless of the ohmicity of the source-drain contacts.

In order to achieve good injecting contacts, a very heavily doped a-Si:H layer is deposited at the metal/a-Si:H interface. At high doping levels, the depletion region becomes thin enough to produce an effective ohmic contact [99]. Examples of ohmic and non-ohmic contacts can be seen in the schematic in Figure 3.5.

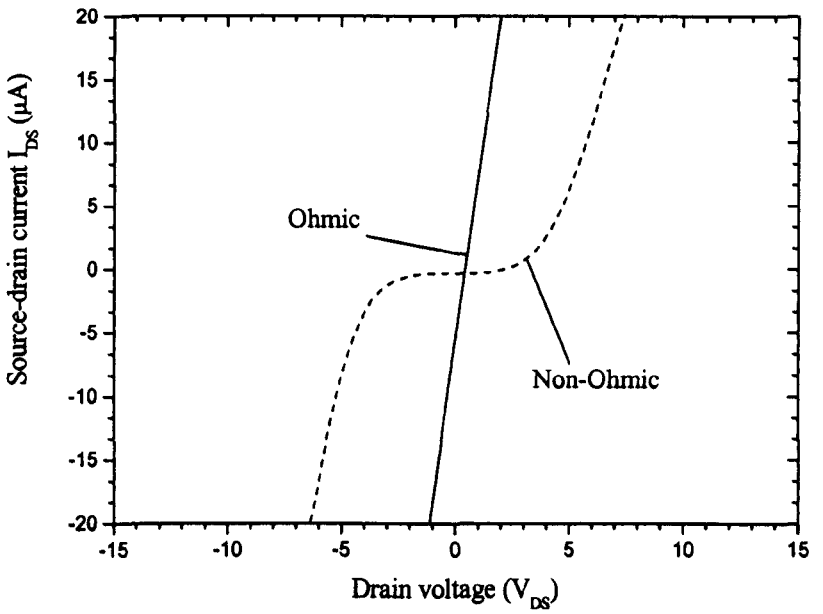

Figure 3.5 Ohmic and non-ohmic contacts

Thermal stability of the contact layers is also a issue for a-Si:H TFTs. Following thermal processing at standard fabrication temperatures (<~ 300 °C), it has been found that aluminium (Al) diffusion into a-Si:H degrades n-channel TFT performance [100][101]. Due to Al being a group III element, it is thought to have a doping effect in a-Si:H producing a p-type layer at the interface [102]. This layer will reduce

electron injection and hence inhibit n-channel operation. Heat increases Al diffusion, and increases the rate at which the p-type layer is produced.

To combat this problem chromium (Cr) is used as an intermediary layer between the Al and the n^+ a-Si:H layer. Al cannot effectively diffuse through the Cr layer so the integrity of the doped a-Si:H layer is preserved. The Al is still necessary as Cr has a very high sheet resistance. However, in these studies, the question of thermal stability was not a major issue as the maximum temperature of any thermal processing was 125 °C. Several studies have reported that Al only reacts with the a-Si:H layer at ~ 150-170 °C, when the contact and sheet resistances increase and there is Al diffusion of tens of nanometers into the amorphous film [103]-[106]. With reference to this, and the need to simplify device fabrication, only Al was used as gate contact material for TFTs in this work.

3.7 DEVICE DESIGN OF TEST STRUCTURES

The device design chosen for the TFTs used here is shown in Figure 3.6. The photolithographic mask set was provided by Philips Research Laboratories, Redhill, Surrey. It is a planar, bottom gate, inverted-staggered structure, known as the keyhole structure. All devices were fabricated in the Emerging Technologies Research Centre.

It is clear from the inverted-staggered structure that there are series resistances at the source and drain. In all cases the channel length was 50 μm, which ensured that the channel resistance dominated over contact resistance. The devices had a W/L ratio of 125 (based on the inner circumference of the channel).

The substrate used was a heavily doped n-type (20mΩcm) <100> oriented single crystal silicon wafer. The wafer acts as a common gate to all devices, but there are both advantages and disadvantages to this method. The large overlap between the source and the gate, and the drain and the gate reduces the series source and drain resistances (§ 3.6). However, the parasitic capacitance associated with this overlap can slow TFT operation, and also lead to an increase in the gate leakage current. However, these factors were not of any great significance in this work. Ohmic

electrical contact to the c-Si wafer was made by removing any surface oxide with a diamond scribe, then attaching a piece of aluminium foil with silver dag (electrically conducting paint).

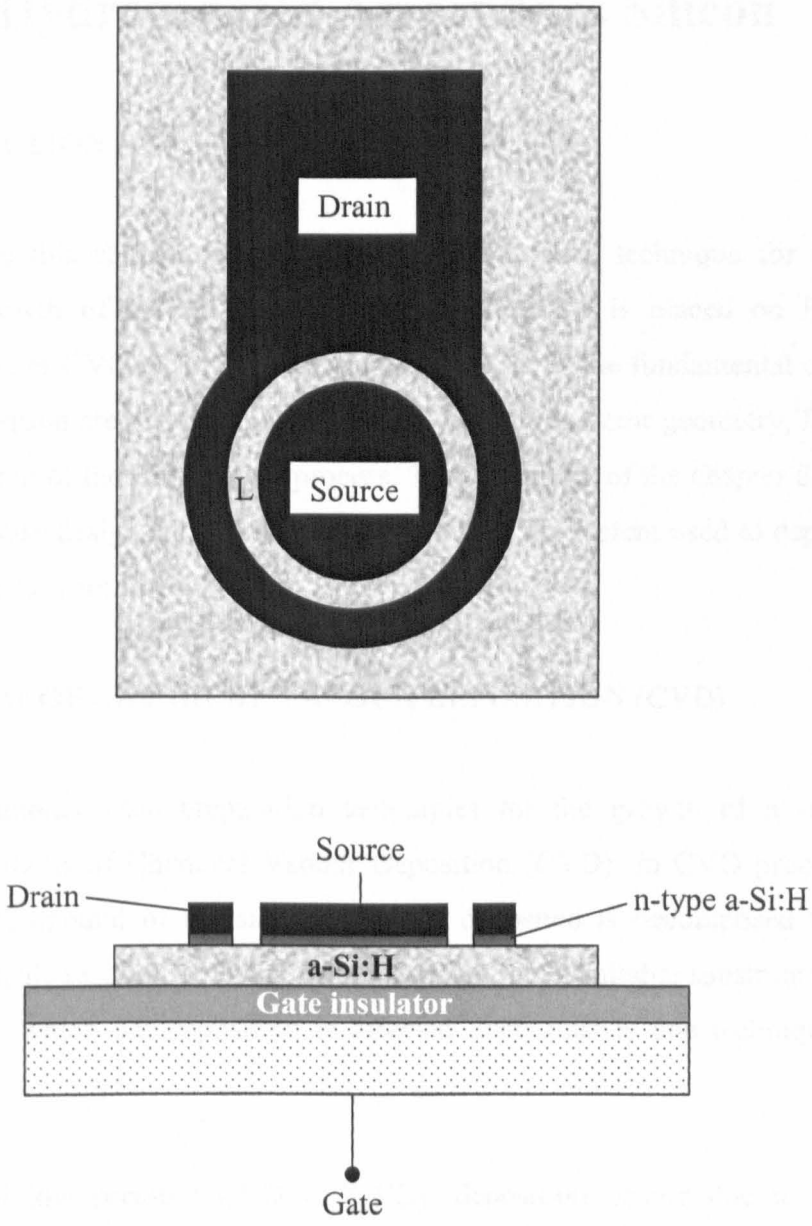

Figure 3.6 Keyhole type TFT structure

Chapter 4

Plasma Enhanced Chemical Vapour Deposition of Hydrogenated Amorphous Silicon

4.1 INTRODUCTION

The aim of the this chapter is to introduce PECVD as a technique for the low temperature growth of a-Si:H. While particular emphasis is placed on PECVD, summaries of other CVD techniques are given. Features of the fundamental concepts of plasma deposition are discussed, including the effect of reactor geometry, followed by a consideration of the film growth process. The remainder of the chapter describes the novel, in-house design and construction of the PECVD system used to deposit the a-Si:H used in this work.

4.2 OVERVIEW OF CHEMICAL VAPOUR DEPOSITION (CVD)

The most commonly used preparation techniques for the growth of a-Si:H, are essentially variations of Chemical Vapour Deposition (CVD). In CVD processes, a vapour phase compound of the substance to be deposited is decomposed to yield desired non-volatile reaction products, which deposit onto a suitable substrate surface. The method by which decomposition is effected distinguishes one technique from another.

In conventional low pressure CVD (LPCVD), deposition occurs due to thermal activation onto a substrate that is heated to temperatures of between 500 – 800 °C. Photo-Enhanced CVD utilises optical energy in the form of Infrared and Ultra Violet radiation to dissociate the precursor gas molecules, hence activating the chemical process for film deposition [107][108][109]. There are important drawbacks for both of these techniques, if the goal is producing a-Si:H for large area displays e.g. AMLCDs. The high temperatures needed for LPCVD are incompatible with the types

of substrates used in large area technologies. Moreover, the process is somewhat inefficient as considerable deposition takes place on all reactor walls. Photo-CVD has the advantage of being a low energy technique with little ion bombardment of the growing film. Also, the temperatures of deposition are compatible with a-Si:H technologies. However, materials produced by this method are expensive and the scalability of these systems, for industrial applications is a problem [110].

There have also been efforts to increase the deposition rate of a-Si:H by either designing novel deposition methods, or by modifying the source gases used so that increased levels of dissociation could be achieved leading to increased growth rates [111]. These new methods include separated plasma triode glow discharge (SPT-GD) [112], controlled plasma magnetron glow discharge (CPM-GD) [113] and electron cyclotron resonance CVD (ECR-CVD)[114]. In the case of SPT-GD, increased dissociation was achieved using a grid grounded via a variable impedance, placed just above the substrate surface. It was claimed that this resulted in a high density of radicals near the substrate and increased the deposition rate. Both CPM-GD and ECR-CVD utilise magnets, (albeit in slightly different ways), in order to suppress the arrival of electrons at the reactor walls, thus effectively increasing the generation of radicals available for deposition. As with other technologies, problems associated with up-scaling of these methods have limited their industrial application thus far. However, good quality films have been produced at low substrate temperatures [115]. To modify the source gases some groups have used disilane and other higher silanes in an effort to increase deposition rate, and rates as high as 17.4 $Å s^{-1}$ have been achieved [116]

Two further techniques that have received considerable attention in recent years are hot-wire CVD (HW-CVD) [117]-[121] and very high frequency plasma CVD (VHF-CVD)[122][123]. In HW-CVD, the source gases are thermally dissociated on a hot tungsten filament. In this way no discharge has to be maintained and the whole process is relatively simple [124]. High deposition rates (>10 $Å s^{-1}$) have been achieved at substrate temperatures commensurate with other, more widely used CVD processes [125]. Other studies have shown that a-Si:H with a very low hydrogen content and electronic properties similar to plasma deposited films can be manufactured by this method [120][126]. However, it has been reported that a-Si:H

films deposited by HW-CVD do not show any systematic correlation between deposition parameters and the resultant film properties [118]. Thus, whilst this technique looks promising, more detailed investigations of the growth and properties of HW-CVD deposited a-Si:H are necessary before the process can be established for routine industrial applications.

VHF-CVD has also been utilised to increase the deposition rate by increasing the dissociation of the source gases. The higher dissociation is attributed to the higher electron density in these types of plasmas as evidenced by the high-energy tail of the electron energy distribution [127]. As a result of this, it has been postulated from Optical Emission Spectroscopy studies (OES) that there is an increase in the flux of ions to the surface [128], which facilitates the creation of more sites for growth precursors to absorb. This process is also thought to enhance surface dehydrogenation [129].

The main reason why VHF-CVD is not thought to be suitable for large area applications is due to potential problems with uniformity. However, TFTs with comparable characteristics to those fabricated using more convention techniques have been produced [130].

Overall, by far the most studied and widely used CVD technique both for research and industrial applications, is that of Plasma Enhanced Chemical Vapour Deposition (PECVD). In the following section, this method will be described in some detail.

4.3 PLASMA ENHANCED CHEMICAL VAPOUR DEPOSITION (PECVD)

Plasmas of importance in PECVD consist of a mixture of gases in which some molecules are ionised and where energetic electrons play an important role in promoting useful chemistry at the substrate surface. The ionisation is produced by the application of sustained external electric or electromagnetic fields (E/EM) – a process that will be discussed later. Under conditions of interest in PECVD we are dealing with a plasma state, which although it may vary from place to place in the reactor, is overall in a quasi-neutral state. Taken over the entire working volume of the plasma the number of positive and negative charges is equal, so the net charge is zero.

There are however important local deviations from space-charge neutrality. For example, those responsible for the self-bias in deposition when using Radio Frequency (RF) excitation. These arise under the combined influences of the externally applied E/EM field, the different mass of the ions and electrons, diffusion, and the attractive and repulsive coulomb fields between the ions and the electrons.

The plasma generation takes place under the influence of the electric field, which acts upon free electrons produced by background radiation or other processes such as local field emission. These are then accelerated by the electric field to sufficient kinetic energy (of the order of 10 eV) to cause ionisation by collision with neutral molecules. This process can be arranged, by control of the applied field, reactor geometry and gas pressure (typically ~ 500mTorr), to yield a controlled plasma with usefully reproducible properties at the substrate.

The resultant plasma is not in thermodynamic equilibrium. However, the condition of the neutral molecules and ions in 'cold' plasmas is such that their mean kinetic energies remain, relative to the kinetic energy of any electrons present in the plasma, undisturbed by the applied electric field, being of the order of a few hundredths of an eV. This is small when compared with the energies acquired by the electrons (~ 10eV). The low mean kinetic energy associated with most of the mass in the plasma allows us to model this massive part of the plasma as 'cold' gas. The difference between the energy acquired by the electrons and the rest of the plasma arises in the acceleration between collisions; ions experience much smaller accelerations than electrons in a given field due to their much larger mass, and so between collisions gain less kinetic energy.

As a result, we can usefully think of the 'cold' plasma as consisting of two subsystems, each with different mean kinetic energies or more loosely speaking 'temperatures'. The neutral molecules and ions having a temperature determined by the input gas temperature and reactor conditions but usually corresponding to temperatures of the order of a few hundred K. This contrasts sharply with the temperature of the electrons, which is of the order of 50,000 K [133]. The neutral molecules gain energy above the ambient only by collisions with ions and electrons and remain at temperatures comparable to the ion temperature

These high-energy or 'hot' electrons promote dissociation reactions with the molecules of the source gases, producing high reaction rates at relatively low substrate temperatures. This allows the processing temperature to be much lower than in a conventional thermal process using similar chemistry. The application of an electric field is a convenient way of supplying the energy necessary to achieve the high (electron) temperatures.

4.3.1 RF DISCHARGES

The majority of work involving PECVD uses high frequency power supplies to generate the glow discharge. The reason for this is that for many applications there is a need to use insulating substrates. If such a substrate is placed in a DC plasma, the surface will acquire a 'floating' potential when the fluxes of ions and electrons to the surface become equal, regardless of the potential applied to the electrode backing the substrate. In practice, once the glow discharge is initiated the insulator will start to charge positively because it loses electrons as ions are neutralised on its surface, and the potential V, of the surface exposed to the discharge will rise towards zero. Eventually the discharge will be extinguished as soon as the insulator surface potential drops below the discharge sustaining voltage.

In order to deal with this problem, an AC discharge is used so that the positive charge accumulated during one half cycle can be neutralised by electron bombardment during the next half cycle. Low frequencies are not very effective because if the time during which the insulator charges up is much less than half the period of the AC supply, the discharge will be off most of the time. Therefore, the frequency of the applied electric field has to be sufficient to prevent the heavier ions from reaching the electrode surfaces. At such a frequency, the positively spaced charge is partially retained between the two half cycles of the alternating electric field. It has been shown that discharges can be maintained in this manner for frequencies above about 100kHz [132].

4.3.1.1 PLASMA ANATOMY

Due to their small mass and high energy, the electrons within the plasma usually diffuse towards all of the surfaces of the reactor (i.e. walls and electrodes). This leaves the bulk of the plasma positively charged and all the surfaces in contact with the plasma exhibiting a negative charge. The relative electric field between the plasma and the surrounding surface creates a thin sheath, which is particularly important in PECVD of thin films.

The most commonly used deposition geometry, and the one used in this work, is shown in Figure 4.1. The potential distribution across the electrode gap is shown for an asymmetric rector design, i.e. the electrode areas are different. The potential fall at the powered (cathode) electrode with respect to that of the grounded electrode (anode) is due not only to the difference in the areas, but also to the presence of a blocking capacitor between the RF generator and the cathode. This leads to a negative DC 'self-bias' voltage being established at the cathode. However, both electrodes are at negative potentials relative to the plasma. The blocking capacitor is introduced to enhance the asymmetry of the system, thereby reducing the ion bombardment effects at the substrate surface. It also ensures that no direct current flows through the plasma hence maintaining the plasma neutrality. It has been shown that the ratio of the time-averaged voltage drop across both electrode sheaths is related to the area ratio of the electrodes, if the sheaths are treated as ideal electrical capacitors [133]. Then,

$$\left(\frac{V_P}{V_G}\right)=\left(\frac{A_G}{A_P}\right)^n, \tag{4.1}$$

where V_P and V_G are the voltage drops across the powered and grounded electrode, and A_P and A_G are the areas of the electrodes. The value of the exponent is four in Koenig and Massel's model, and is the case for low-pressure conditions with a collisionless discharge. During PECVD conditions the exponent decreases to ≤ 2 [134]. It also depends on plasma parameters such as input power. The plasma potential V_{Pl} is equal to the voltage drop at the sheath of the grounded electrode.

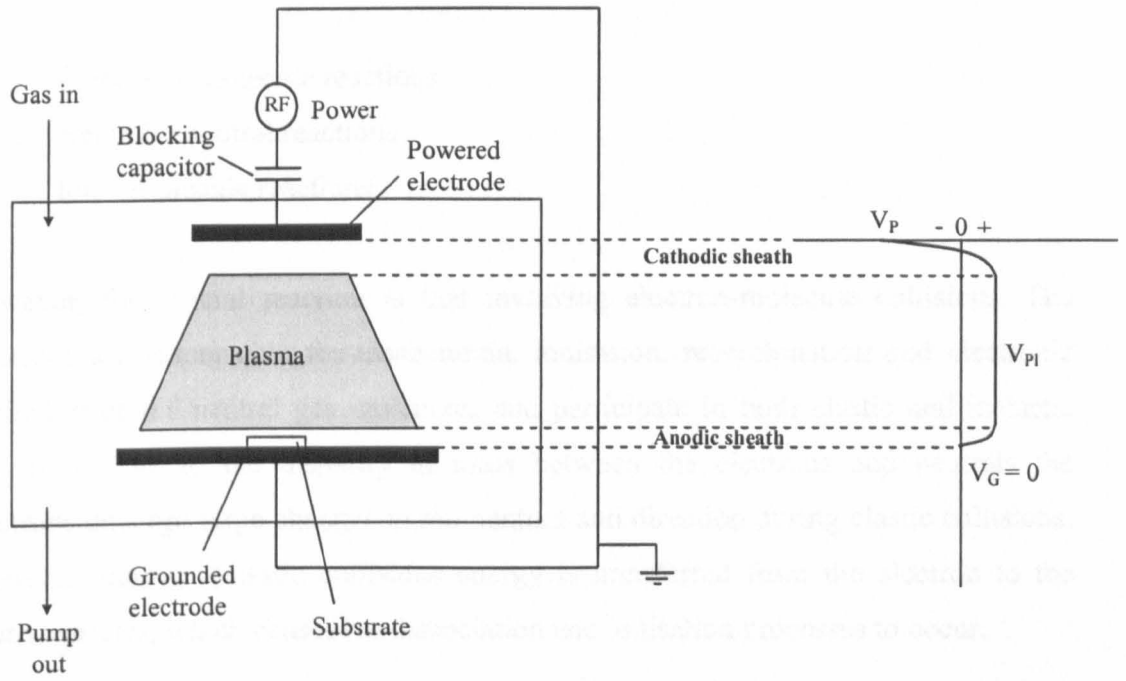

Figure 4.1. Schematic of RF discharge in parallel plate reactor with capacitive coupling of the RF generator, together with special distribution of potential voltage (plasma potential V_{PI}, voltage on powered electrode V_P and voltage on grounded electrode V_G)

The sheaths are very important as they influence the ion energy distribution and hence the ion bombardment at the growth surface. Ion bombardment can induce surface changes such as enhancement of diffusion of film-forming radicals and displacement of surface atoms. It is also heavily dependent on the plasma excitation frequency and the operating pressure of the process. At frequencies higher than 1 MHz the ions are unable to follow the AC field. The vast majority of PECVD processes are operated at an RF frequency of 13.56 MHz. There is nothing special about this particular frequency as far as this technique is concerned, but it is an agreed frequency that can radiate a certain amount of RF energy without interfering with communication systems.

4.3.1.2 GAS PHASE CHEMICAL PROCESSES

The gaseous phase reactions that take place within the plasma and that lead to the deposition of a-Si:H, can be described by the following:

1. Electron – molecule reactions
2. Neutral – neutral reactions
3. Ion – molecule reactions

However, the crucial reaction is that involving electron-molecule collisions. The electrons are responsible for dissociation, ionisation, recombination and electronic excitation of the neutral gas molecules and participate in both elastic and inelastic collisions. Due to the disparity in mass between the electrons and neutrals the electrons undergo large changes in momentum and direction during elastic collisions. However, during inelastic collisions energy is transferred from the electron to the neutral species, which causes the dissociation and ionisation processes to occur.

The electron collisions can cause the gas molecules to be excited to a higher electronic state, from which recombination to the ground state results in the emission of photons and is the origin of the plasma glow, although many transitions are in the UV region of the spectrum. The gas molecules can also be excited into higher vibrational or rotational states. However, by far the most important reactions, as far as film deposition is concerned, are those that involve the production of dissociated and ionised species.

It has been described that the most important species within the plasma are likely to be SiH_2 (silyene), SiH_3 (silyl) and H [135][136]. Examples of reactions involving these primary species that require low energies are [34],

$SiH_4 \rightarrow SiH_3 + H$	2.2 eV
$SiH_4 \rightarrow SiH_2 + H_2$	4.0 eV
$SiH_4 \rightarrow SiH_2 + 2H$	4.2 eV

After these steps, a succession of reactions takes place, which complicate the chemistry of the discharge enormously. These secondary reactions result in the formation of higher silanes from reactions between the aforementioned initial species. It must also be noted that in a typical low power plasma the fraction of molecular

species that are radicals or ions is only ~ 10^{-3}, therefore, most collisions are with silane.

e.g. $SiH_2 + SiH_4 \rightarrow Si_2H_6$ and $Si_2H_4 + H_2$

$SiH + SiH_4 \rightarrow Si_2H_3 + H_2$

$Si + SiH_4 \rightarrow Si_2H_2 + H_2$

An exhaustive list of gas-phase reactions and a discussion of plasma chemistry can be found in the literature [137][138], but these are beyond the scope of this work.

The reactions of the H atoms are also of great importance. These result in a large increase in the production of the SiH_3 radical, which is thought to be the dominant species that contributes to film growth of a-Si:H (as discussed later). The silyl radical does not react with the parent silane molecule (except in a hydrogen transfer reaction), as Si_2H_n structures are only possible with $n \leq 6$. This is borne out in results from a number of experiments summarised in Table 4.1, carried out to investigate the number densities of the various species within a silane plasma [139].

The concentrations of the film-forming radicals are determined by the parameters of the plasma that affect the electron density and energy, (i.e. pressure, RF power, generating frequency, and gas composition).

Table 4.1. The number densities of some reactive radical species in a steady state SiH_4 plasma

Radical	Detection method	Density in plasma (cm^{-3})
Si	Laser induced fluorescence	$\sim 10^8 - 10^9$
SiH	Laser induced fluorescence	$\sim 10^8 - 10^9$
SiH_2	Intra-cavity laser absorption	$\sim 10^9$
SiH_3	Infrared laser absorption	$\sim 10^{12}$

4.3.1.3 α-γ' TRANSISTION

Two important plasma regimes have been identified for RF PECVD deposited a-Si:H:

the α regime and the γ' regime [140][141][142]. The α regime occurs when electrons at the sheath edge gain energy from the sheath electric field and collide with silane molecules to produce SiH_3, SiH_2 and H radicals [143]. At low pressures, this has been termed as 'stochastic electron heating' [144], and at high pressures when the electron-molecule collision frequency is much higher than the RF frequency, the process has been referred to as 'wave riding' [145]. However, the α regime usually occurs at low silane partial pressures and low RF powers.

The γ' regime occurs when electrons attach to particles in the plasma, causing them to become negatively charged. The particles can be generated by higher pressures producing more gas phase reactions or by higher RF powers dissociating more molecules to reactive radicals [146]. This causes an electric field to build up in the plasma zone, which heats the electrons, and consequently they acquire a larger kinetic energy. This is referred to as 'Joule heating'. The impedance of the plasma then becomes resistive rather than capacitive, improving the power coupling into the plasma, which leads to more dissociation of the silane molecules and hence higher deposition rates.

The transition between the two regimes is thought to be initiated by the formation of large (or powder) particles in the gas phase that arise due to increased dissociation. Negative ions are then trapped in the plasma bulk and react with silane molecules to create larger negative ions. The charge of these particles can fluctuate, and can become positive. The clusters coalesce and become bigger due to deposition of a-Si:H on their surface [147] to form powder. These particles can also land on the substrate surface leading to the formation of unwanted voids within the a-Si:H. However, at high silane partial pressures, the particles are confined to the plasma. Although the deposition rate decreases as the silane source gas is depleted.

It has been demonstrated that particulate formation at higher process pressures can be limited by using high levels of hydrogen dilution, and in industrial applications, the γ' regime is often utilised for a-Si:H growth because of the high deposition rates associated with it [143].

4.3.2 THE DEPOSITION PROCESS OF A-Si:H

A general schematic of the processes involved in a-Si:H deposition has been given by Perrin [148] and a slightly modified version can be seen in Figure 4.2. After the source gases have entered the reactor, various electron-molecule reactions take place (excitation, dissociation, ionisation) that produce neutral radicals and both positive and negative ions. The diffusion of the radical species to the substrate surface leads to material deposition. Negative ions are confined to the bulk plasma, whilst positive ions are accelerated to the substrate by the sheaths that form above the grounded electrode. The confinement of the negative ions can lead to particulate formation as they recombine with silane radicals to become large negative ions (or small clusters) [147]. A number of surface reactions then take place, which enable film-forming radicals to diffuse to growth sites or desorb from the surface. In addition, sub-surface reactions can lead to the release of hydrogen from the network.

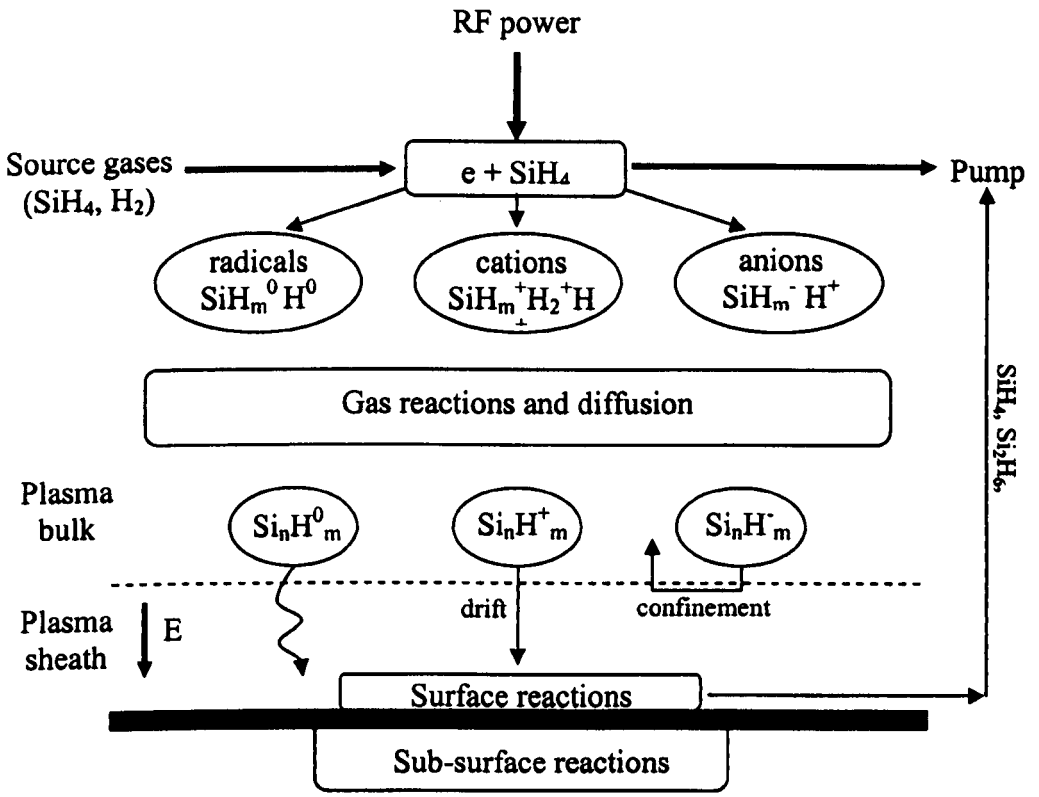

Figure 4.2 Schematic of the processes occurring during a SiH_4/H_2 discharge (after J. Perrin in Plasma Deposition of Amorphous Silicon-Based Materials, ed. G. Bruno et al (Academic Press, U. S. A., 1995) Ch. 4, p 177)

It is generally accepted that the silyl radical (SiH_3) is the predominant growth precursor in device- quality a-Si:H. Whereas silyene (SiH_2), SiH, Si and the higher order silane molecules all prove to be detrimental to film growth [149][137]. The SiH_3 radical is thought to physisorb onto an almost fully hydrogen-terminated silicon surface and diffuse long distances within the network of the a-Si:H material [150][151]. The final stage is the removal of hydrogen as each hydrogen-rich surface layer is buried to become part of the bulk a-Si:H. This final process reduces the level of hydrogen from >50% at the surface, to ~ 10% within the bulk [152].

A number of models have been proposed for the deposition of a-Si:H [153]-[159].The first was developed by Ganguly and Matsuda [153][154]. This details the absorbed SiH_3 radical reacting with the hydrogen-terminated silicon surface by abstraction or addition, which creates and removes dangling bonds. It was postulated that these reactions actually determine the dangling bond density in the bulk a-Si:H.

A further model has been suggested that is based on the greater mobility of hydrogen atoms when compared to silicon atoms [155][156]. The Si-Si network is essentially fixed up to a temperature near the crystallisation temperature of 650 °C, whereas hydrogen is mobile above ~ 200 °C, and its motion facilitates the interconversion of weak bonds, strong bonds and defects. This is a subsurface reaction, and surface processes are not included. In this model, the optimum temperature for a-Si:H deposition is above the hydrogen diffusion temperature, so weak bonds within the network can be removed as a result of hydrogen motion.

Computer simulations are the foundation for another set of models [157][158][159]. These describe the creation of the film forming species within the plasma, the reactions of these species with the substrate surface and the a-Si:H network formation. They do not discuss the formation of defects or disorder, but concentrate more on the relationship between discharge conditions and material properties such as deposition rate and hydrogen content.

It is now useful to give a description of the surface and sub-surface reactions involved in a-Si:H growth. Here it is assumed that SiH_3 is the dominant growth precursor. The basic reactions of SiH_3 with the a-Si:H are illustrated in Figure 4.3.

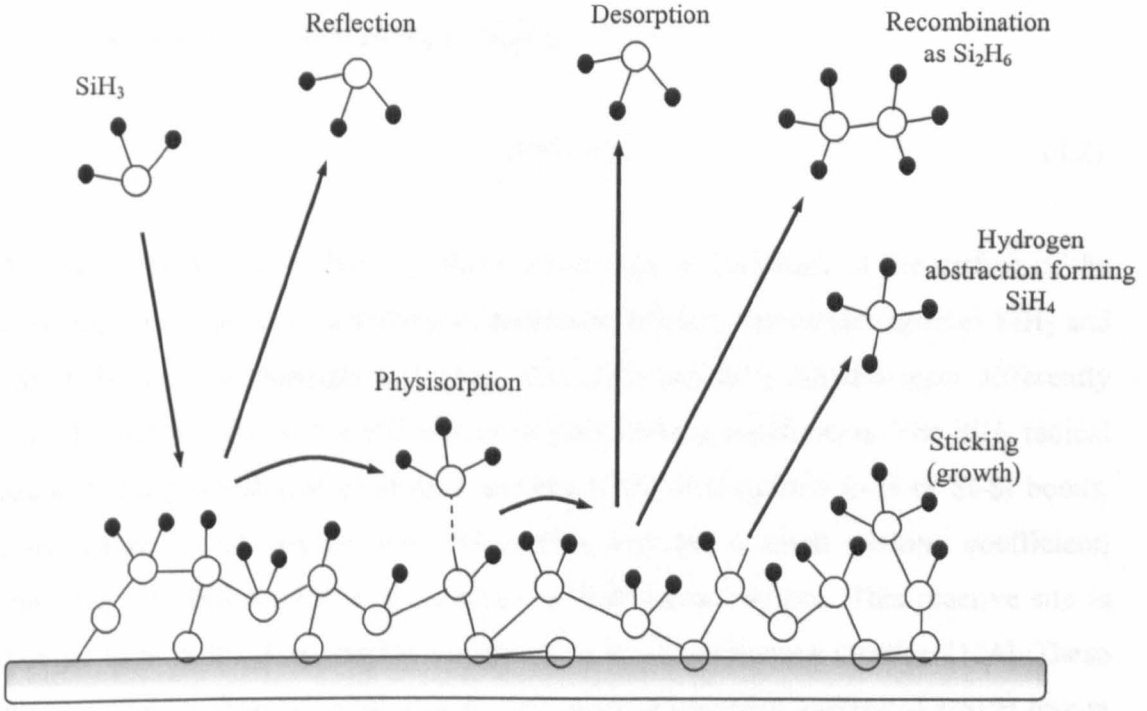

Figure 4.3. Schematic representation of surface reactions during a-Si:H growth from SiH_3 radicals (after J. Robertson, J. Appl. Phys. 87, 2608 (2000).)

The SiH_3 radical is weakly absorbed (physisorbed) on the hydrogen-saturated a-Si:H surface by a 3 centre Si-H-Si [160]. The probability for this process is the surface reaction probability β. It can then undergo a number of different processes [161]. One possibility is its diffusion over the surface from one surface hydrogen to another. During this process, it can either abstract a hydrogen atom, thus creating a dangling bond and hence an SiH_4 molecule, or stick to a surface dangling bond (chemisorbtion) and contribute to film growth. A further possibility is that the SiH_3 reacts with a second physisorbed SiH_3, forming Si_2H_6. Thus, film growth is controlled by the precursor-mediated sticking of SiH_3, the precursor mediated hydrogen abstraction by SiH_3 [162], and the surface diffusion length of the absorbed radicals [148].

A high surface mobility is necessary to reduce the surface roughness and porosity due to self-shadowing of incident species [163]. The effective β-value is determined by

two separate possibilities:

- The sticking probability s, i.e. the probability that the SiH_3 remains chemisorbed and incorporated into the a-Si:H film
- The recombination probability γ, i.e. the probability that the SiH_3 is desorbed as a gaseous species (SiH_4 or Si_2H_6),

$$\beta = s + \gamma \tag{4.2}$$

At low temperatures, ($\leq$ 200 °C), there is a change in the nature of the surface of the growing film. Instead of a hydrogen-terminated surface, the surface species SiH_2 and $-Si-H_3$ become increasingly important. The SiH_3 and SiH_2 radicals react differently with this surface due to the differences in their sticking coefficients. The SiH_2 radical has a sticking coefficient close to 1 and can insert directly into Si-H or Si-Si bonds. $Si-H_3$ cannot react directly with the surface and has a small sticking coefficient, enabling it to diffuse across the surface to find a reactive site. This reactive site is thought to be a dangling bond at a step-like or kink-like surface location [164]. These mechanisms are thought to account for the extremely smooth surface of a-Si:H grown under device quality conditions [165].

A very different view of a-Si:H growth has recently been proposed by Von Keudell and Abelson [166]. They suggested that SiH_3 can insert directly into strained Si-Si bonds on the surface, forming a five-fold coordinated bond. Evidence for this reaction has been obtained from studies undertaken by Ramalingam et al that involved molecular dynamics studies of SiH_3 impinging on a Si surface at 500 K [167]. However, it is not certain how these observations would result in film deposition because of the limited number of strained bonds at the surface, and also because it is a self-limiting process [162].

One aspect of a-Si:H film growth that has not been extensively discussed in the literature is the removal of hydrogen during the growth process [168][152]. Bulk a-Si:H only has a hydrogen concentration of between 5–20 % [169][170] compared to a

surface concentration of > 50%. Therefore, the hydrogen must be eliminated during the growth step.

Robertson has suggested that the processes that cause hydrogen elimination lead to the formation of weak Si-Si bonds that are frozen into the structure. The dangling bond defects then arise from these weak bonds by a defect pool process [152]. Ganguly and Matsuda [153][154] consider that the surface dangling bond density is formed during growth and is then buried to form the bulk material. They found a minimum in the dangling bond density, and a maximum in the surface diffusion coefficient occurring simultaneously at ~ 250 °C [153]. However, using data from in-situ ESR measurements, Yamasaki et al [171] have found that the surface defect density is much greater than the bulk defect density. Robertson [152] argues that as most of the hydrogen in the surface layer is eliminated as each surface layer is buried, ~ 50% of all bonds change from an Si-H configuration to Si-Si. Consequently, it is open to question that the surface defect density during growth (~ 10^{-6}) is buried during deposition, whilst a large proportion of bonds change their type.

Instead, it has been proposed that local bond rearrangement is the facilitating process for hydrogen elimination from the growing a-Si:H film [152]. It is assumed that hydrogen exists largely in pairs, similar to the H_2^* in c-Si. The H_2^* consists of two S-H bonds in the same direction [172][173]. It can undergo a local rearrangement with one hydrogen atom passing through two bond centre positions, at an energy of 1 eV [141]. A further local rearrangement is possible in which a hydrogen atom passes through the bond centre to combine with another hydrogen atom to form an interstitial H_2 molecule. The energy barrier for this is the bond centre site energy, and is less for a weak Si-Si bond than a strong one [172]. Thus, weak bonds aid in the elimination of hydrogen from the growing a-Si:H network. However, it is claimed that the surface diffusion model, as proposed by Ganguly and Matsuda, can be applied to interpret measurements of the surface dangling bond density without controversy [174].

4.3.2.1 THE EFFECT OF IONS

Ions can play a major part in the deposition of a-Si:H. Ion bombardment can provide

energy for the promotion of surface reactions and also lead to a reduction in the hydrogen content [175]. Depending on the regime of the discharge, ions can account for ~ 10% of the growth flux [176][141]. As described above, the α regime has a low plasma density, but there is a high ion flux within the discharge. The potential energy of ions, which is released when the ion is neutralised, is typically 10 eV, and the release of this ionisation energy is sufficient to excite atoms into excited electronic states, thereby weakening their bonds and enhancing their mobilities [177]. Ions can penetrate the film causing hydrogen elimination by displacing hydrogen atoms from subsurface Si-H bonds. The hydrogen then recombines as H_2 molecules, which diffuse back to the surface [152].

Ion bombardment may have either a beneficial or a detrimental effect on a-Si:H film growth. Light, slow ions mostly vibrationally excite surface SiH bonds. This can enhance the diffusion or desorption of weakly physisorbed species (e.g. SiH_3), but not remove a reactive radical (e.g. SiH_2) [148]. Therefore, the ion energy has to be sufficient to induce 'shot-peening' of the immobile chemisorbed species, and overcome the 'self-shadowing' effect, which is responsible for the development of surface roughness and columnar growth within the film [178]. Conversely, if the ion energy is too high, ions penetrate deeper into the growth zone and create local defects and dangling bonds, which can remain trapped within the network. In addition, they can introduce compressive stress and radiation damage to the film, which are both undesirable.

The effect of noble gases (Argon, Helium, Xenon) as dilutants of the SiH_4 source on the properties of a-Si:H gas has been studied by several workers [179][180]. It has been shown that dilution with argon and xenon decreases the production of the SiH_3 radicals, in favour of $SiH_{m<3}$ that can cause powder generation in the plasma [136][181]. In contrast, both helium and hydrogen (H_2) dilution have the reverse effect [182]. H_2 also leads to an increase in atomic hydrogen production, which can reduce the fraction of higher SiH_x groups in the surface region [183].

Studies of the optoelectronic properties of a-Si:H have shown an improvement in photoconductivity and a reduction of bulk defect density where the ion energy does

not exceed ~ 75 eV; with the best conditions being those with a large ion flux and moderate ion energies (~ 20-50 eV) [184]. The best method to achieve this is to use ultra-low pressure, magnetically confined discharges such as those utilised in Electron Cyclotron Resonance reactors. This is also an efficient way to increase the deposition rate. However, problems with scalability (as previously discussed) have, thus far, precluded techniques such as these being used extensively in industrial applications.

4.4 LOW TEMPERATURE DEPOSITION OF A-Si:H

Low temperature deposition of a-Si:H has been investigated by a number of workers, and was first reported by Moustakas et al [185]. Since then various deposition techniques have been used in an effort to produce high quality material at temperatures compatible with more rugged and inexpensive substrates [115][186]-[190].

Hishikawa et al [191] demonstrated that by lowering the deposition rate, the quality of a-Si:H films deposited at very low substrate temperatures could be improved. It was suggested that this was due to an increase in the time available for surface reactions to occur. Roca i Cabarrocas [192] emphasised the importance of limiting the polymerisation of the film forming species both in the plasma and at the surface. Material produced at a substrate temperature of 35 °C with a high monohydride fraction of bonded hydrogen has also been reported [193]. Helium dilution of the silane source gas and a post deposition anneal > 150 °C resulted in an improvement in the photosensitivity to near 10^5.

Most reports suggest that when a-Si:H is deposited at temperatures < 150 °C and optimum material structure and composition is achieved, a thermal activation can lead to good electronic properties [194]. However, in the as-deposited state, low temperature material has poorer optoelectronic properties and higher defect densities than films grown at higher temperatures. Therefore, a key commercial challenge is to re-optimise the deposition conditions in order to obtain films with good electronic properties at temperatures compatible with inexpensive substrate materials.

Towards this end, a capacitively coupled RF PECVD system has been designed in order to investigate the effect of pre-heating of the source gases for the deposition of a-Si:H at low substrate temperatures (<150 °C).

Investigations into the effects of source gas pre-heating using the PECVD technique have been carried out previously [195]-[198]. Gas heating has been achieved by a variety of techniques such as heating the cathode within the PECVD chamber [195]; heating the gas supply line both inside and outside the reactor [196][197][198]; and inserting a heated grid into the reaction vessel close to the substrate surface [139]. It has been reported that gas-heating can lead to suppression of the unwanted dissociation of SiH_4 into SiH_2 and H_2, thus reducing the likelihood of gas phase and surface polymerisation and dust formation [197].

However, this technique has yet to be employed in an investigation of a-Si:H grown at temperatures compatible with plastic substrates.

4.4.1 THE NOVEL PECVD SYSTEM

The original PECVD system (Oxford Plasma Technology μP80) present within the Emerging Technologies Research Centre could not be modified to carry out the proposed work, due to the nature of its configuration. Therefore, it was necessary to design a brand new system that would be able to facilitate the necessary investigations. However, resource constraints had to be recognised. It was necessary to utilise both the existing roots/rotary pumping combination and the RF matching network that were part of the OPT system, and incorporate them into the new design. A schematic of the new system can be seen in Figure 4.4.

The system consists of a cylindrical, planar stainless steel chamber with an internal diameter of 280mm, height 100mm and wall thickness 1cm. The upper and lower electrodes are aluminium with a separation of 3cm. The upper electrode is water-cooled by a Betta-Tech Controls CU 500 heater/chiller and is attached to the top of the chamber via four lengths of stainless steel studding. The bottom electrode is an OPT RIE 80 Plus substrate table that has copper pipes embedded within it. These are

normally used for cooling, but here they are used as a means of heating the table. A heat transfer oil (type WTP-3) is circulated through the pipes by a Betta-Tech Controls BT-175E heater/chiller, and can be heated to a temperature of 150 °C. The oil temperature is monitored by the heater unit and the substrate temperature is monitored by a K-type thermocouple attached to the central feedthrough of the table. Under steady flow conditions, the measured oil and substrate temperatures agreed to within ± 2 °C in the temperature range 25 – 150 °C. The lower electrode is grounded and the upper electrode is driven by an ENI ACG-5XL RF power generator at a frequency of 13.56MHz via a high frequency matching network.

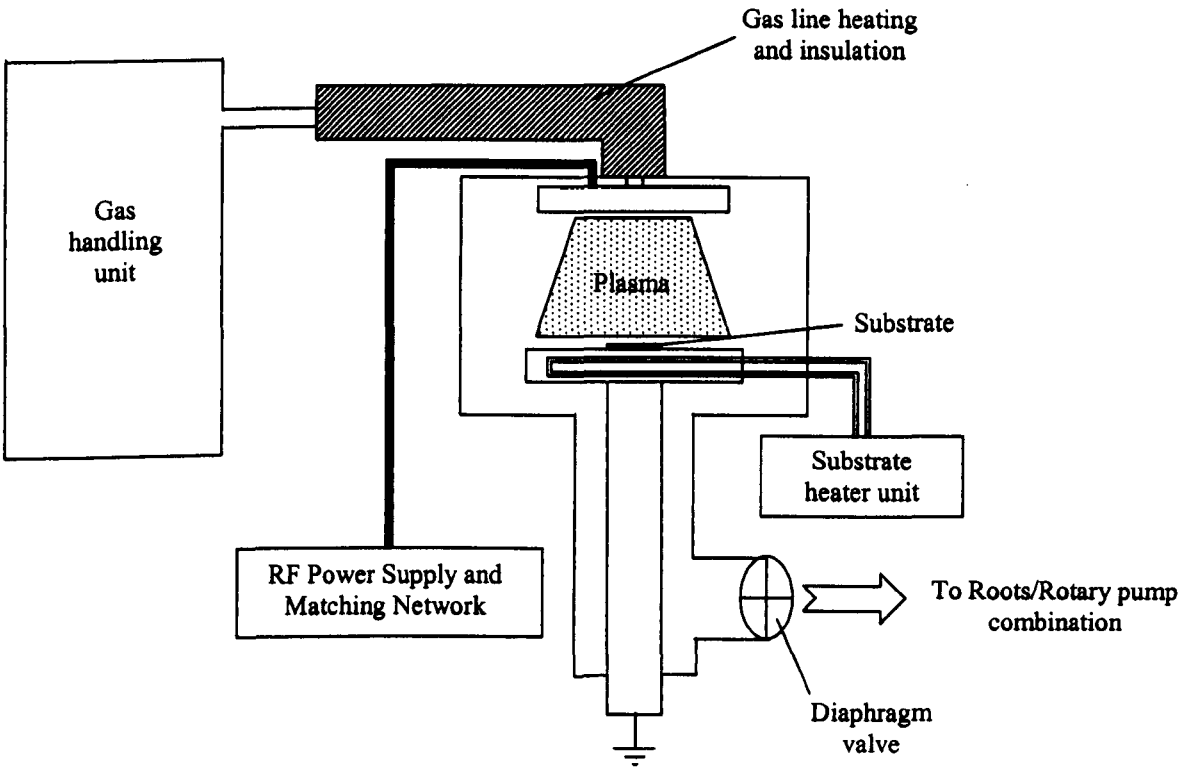

Figure 4.4 Schematic of the PECVD system designed and used in this work

The source gases enter the system through helium leak checked, 0.25mm external diameter, stainless steel tubing and can be selected by push button controls on the front of the OPT microprocessor unit. The gas flow rates are determined by Tylan FC-260 mass flow controllers (MFCs). After passing through the MFCs, the source gases are mixed in a manifold before being admitted to the chamber through a showerhead gas inlet arrangement situated centrally on the upper electrode.

The chamber is evacuated through a pumping port in the centre of the base plate. For pump down, a combination of a roots pump (Edwards Mechanical Booster EH 500) and a rotary pump (Edawards High Vacuum Pump E2-M80) is used. This combination can attain a base pressure of $< 10^{-3}$ Torr in under five minutes. When the source gases are flowing (i.e. during deposition), the pressure is set manually by adjusting an Edwards SP40K Speedivalve situated between the pumps and the chamber. An Edwards Type 600 Barocel capacitance manometer is used to monitor the pressure both during deposition and during chamber pump down. Substrate holders, also designed by the author, transport the substrates (c-Si and Corning 7059 glass) into the chamber through a frontloading door.

The gas inlet tubing is heated by Electrothermal HT9 heating tape wrapped around the pipeline and insulated by Crown & Rock Fibre H&V Pipe Insulation (SA grade), which enables the gas line to be heated to 450 °C. The temperature of the line is monitored and controlled by an Electrothermal Digital Temperature Controller that enables the temperature to be regulated to ±1 °C in the range 25 – 400 °C.

Chapter 5

Thin Film Characterisation Techniques

5.1 INTRODUCTION

A fundamental aim of this research was to investigate the effect low temperature deposition has on the properties of a-Si:H, and hence how these properties affect the performance of TFTs. The next generation of large area electronic applications will include the use of transparent, flexible substrates, which impose temperature restrictions on thin film deposition processes. Therefore, it is vitally important to understand how growth parameters modify the properties of electronic materials at temperatures compatible with such substrates. In this chapter the characterisation of a-Si:H and silicon nitride (SiN) films is reviewed and the different physical and electrical techniques are briefly discussed.

Typical a-Si:H layers used in these studies were deposited onto both single-side polished c-Si (1-5Ωcm, <100>, n-type), and Corning 7059 glass substrates to a thickness of approximately 0.5μm. Typical SiN samples were deposited onto c-Si substrates only to a thickness of approximately 1000Å. All substrates were cleaned, prior to any deposition, according to the procedures described in Appendix B.

5.2 PHYSICAL CHARACTERISATION

Using the physical characterisation techniques outlined in this section, the bonding configuration, hydrogen content, optical band gap and thickness of the PECVD films can be determined.

5.2.1 FOURIER TRANSFORM INFRARED SPECTROSCOPY (FTIR)

Much of the understanding of bonded elements in a-Si:H and SiN has been gleaned from detailed studies of the vibrational spectra from infrared absorption measurements

[199]. The exact frequency of the absorption depends on both the mass of the oscillating dipole and the strength of the bond between the atoms of that dipole. Therefore, different molecular species can be identified by their characteristic absorption frequency. Of particular interest in a-Si:H is the way in which hydrogen is bonded within the amorphous material. Hydrogen is a light atom, and as a result, the frequencies of the hydrogen modes are above those of the silicon network. Consequently, the analysis of the monohydride or polyhydride modes is relatively simple. The important absorption peaks observed in PECVD a-Si:H and a-Si:H alloys and the corresponding bonding configurations are shown in Table 5.1.

In this work, measurements were made using a Shimadzu FTIR-8300 spectrophotometer with a resolution of ±2 cm^{-1}. The scanning range used was from 400 cm^{-1} to 4000 cm^{-1}. Samples for infrared characterisation were deposited onto c-Si substrates, due to the high transparency of the material in this region. An infrared spectrum of an uncoated c-Si substrate was taken and then subtracted from the thin film test samples in order to eliminate any background contributions from the silicon.

Table 5.1 Infrared absorption frequencies for a-Si:H and a-Si:H alloys

Bonding Configuration	Absorption peak wavenumber (cm^{-1})
Si-H	630 (b), 2000 (s)
$Si-H_2$	630 (r), 890 (b), 2090 (s)
$(Si-H_2)_n$	630 (r), 850 (w), 845 (b), 890 (b), 2090 (s)
$Si-H_3$	630 (r), 860 (b), 905 (b), 2140 (s)
Si-OH	940 (s), 3380 (s)
Si-O	920 (s)
$Si-O_2$	460 (r), 805 (b), 1080 (s)
Si-N	840 (s)
N-H	1150 (b), 3350 (s)
	[b, bending; s, stretching; r, rocking; w, wagging]

Quantitative information concerning the concentration of hydrogen within a-Si:H can be extracted from FTIR spectroscopy by integrating over the absorption peak at 630 cm^{-1}. This peak is used as it includes the rocking modes of all possible Si-H bonding configurations. In this work the hydrogen concentration, C_H, was calculated using equation (5.1)

$$C_H = A_{630} \int \frac{\alpha(\omega)}{\omega} \, d\omega \tag{5.1}$$

where $A_{630} = 2.1 \times 10^{19}$ is the proportionality constant determined by Langford et al [200], ω is the wavenumber and $\alpha(\omega)$ the absorption coefficient measured at wavenumber ω. The concentrations were then normalised to at% by dividing through the atomic density of c-Si (5×10^{22} cm^{-3}) [201].

In order to distinguish between isolated Si-H bonds and other bonding configurations such as clustered monohydride and dihydride bonds, bonds on internal void surfaces, and isolated dihydride bonds, Mahan et al [202] have defined a microstructure factor, R, as described in equation (5.2).

$$R = \left(\frac{I_{2100}}{I_{2000} + I_{2100}} \right) \tag{5.2}$$

where I_{2000} and I_{2100} are the integrated absorption intensities centred around 2000 cm^{-1} and 2100 cm^{-1}. These values were calculated in a similar manner to that used for the determination of the hydrogen concentration detailed in equation (5.1). However, the proportionality constants were $A_{2000} = 9.0 \times 10^{19}$ cm^{-2} and $A_{2100} = 2.2 \times 10^{20}$ cm^{-2} respectively [200]. As previously stated, in device quality a-Si:H films hydrogen is bonded predominantly in a monohydride configuration. Therefore, an R-value equal to approximately zero would yield ideal material.

The hydrogen content of silicon nitride films and the density of Si-H and N-H bonds were also calculated using equation (5.1), but the proportionality constants $A_{SiH} = 1.4 \times 10^{20}$ cm^{-2} and $A_{NH} = 2.8 \times 10^{20}$ cm^{-2} were used [200].

5.2.2 UV/VISIBLE SPECTROSCOPY

UV/Visible spectroscopy can yield information on the optical band gap of a-Si:H films. In this work, a Unicam-UV2 UV/VIS double beam spectrometer was used with a scanning range of 200 – 900 nm. Films were deposited onto Corning 7059 substrates due to their transparency over the visible part of the spectrum, and an uncoated substrate was used as a reference sample.

Photons with energies greater than that of the band gap of a-Si:H are strongly absorbed which results in the excitation of electrons into the extended states. If a parabolic distribution for the density of states in both the conduction and valence bands is assumed, the Tauc equation (5.3) can be used to describe the energy dependence of the absorption coefficient [203].

$$[\alpha(E)h\nu] = C_{TAUC}\{h\nu - E_o\}^2 \tag{5.3}$$

where α is the absorption coefficient, $h\nu$ is the energy associated with a given wavelength, C_{TAUC} is a constant and E_o is the optical gap of the material.

Firstly, we calculate the absorption coefficient from equation (5.3)

$$\alpha = In\left(\frac{I_0}{I}\right)\left(\frac{1}{d}\right) \tag{5.4}$$

where I_0 and I are the incident and measured intensities, and d is the thickness of the deposited film. Then by letting $(h\nu)$ = E and substituting in equation (5.3) we get,

$$\alpha E = C_{TAUC}(E - E_0)^2 \tag{5.5}$$

Let $(E-E_0) = E_g$ in equation (5.5) so that,

$$\alpha E = C_{TAUC}(E_g)^2 \tag{5.6}$$

Then taking the square roots of both sides,

$$(\alpha E)^{1/2} \ \alpha \ (E_g) \tag{5.7}$$

By plotting a graph of $(\alpha E)^{1/2}$ versus E, the optical bandgap can be obtained from the intercept of the slope on the x-axis.

A typical Tauc plot derived from absorption data can be seen in Figure 5.1. Here the optical bandgap for this film was 1.73eV.

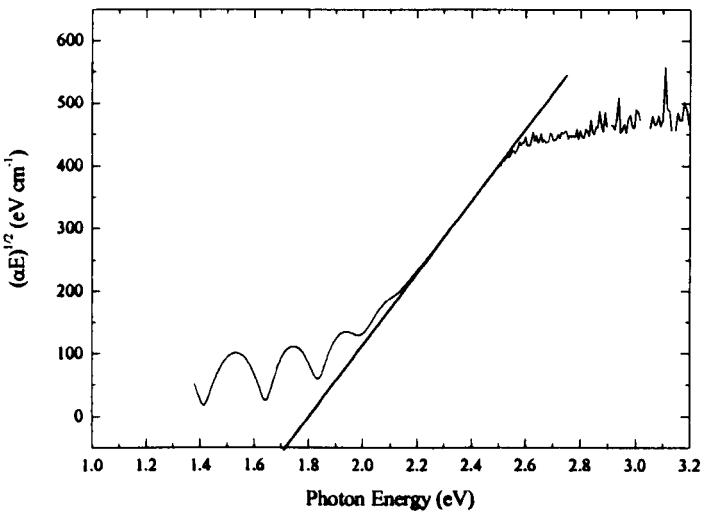

Figure 5.1 A Tauc plot for an a-Si:H film grown with source gas heating

5.2.3 FILM THICKNESS MEASUREMENT

Ellipsometry is a commonly used technique to determine thin film thickness and can provide measurements accurate to within a few angstroms. However, due to the limitations of the analysis software available, it was not possible to use this technique for the measurement of a-Si:H. The thickness of a-Si:H films deposited in this work was found by stylus profilometry, which involves the measurement of the topology of a film 'step' by mechanical movement of a diamond needle stylus across the sample surface [204]. It should be noted that a number of factors can affect the resolution of this technique: stylus penetration, surface roughness and equipment vibration.

The profilometer used in these investigations was a Tencor Alpha Step 200, which has a vertical resolution of ± 5Å. Obviously, it is imperative to create a very abrupt step to ensure an accurate measurement of film thickness. Not least as this measurement is used in a number of other calculations. Therefore, a simple lift-off technique was implemented. This involved a heavy line of ink from a felt tip, permanent marker pen being drawn onto the substrate prior to deposition. Post-deposition, the substrate was placed in acetone for ~5 minutes. The ink dissolved in the acetone, thus lifting off the film grown on top of it. The result was an abrupt step that could readily be measured by the profilometer. Providing that sufficient ink is applied to the substrate surface before film growth, this simple technique is more than adequate for the determination of film thickness.

5.2.4 ELLIPSOMETRY

Ellipsometry is a simple and non-destructive measurement technique that is used for the determination of the refractive index (R.I.) and the thickness of thin film materials, and was the chosen method here for the investigation of the SiN films deposited in this work. All measurements were taken using a Rudolph Research Auto El III ellipsometer operating with a He-Ne laser at a wavelength of 632.8 nm. The automatic measurement produced values defined to 3 significant figures, i.e. ± a few angstroms for a film thickness of 1000 Å.

For device-quality, stoichiometric films of silicon nitride (SiN) deposited by LPCVD a an R.I. value of 2.05 is expected [205].

5.2.5 ETCH RATE MEASUREMENTS

A useful measure of the physical integrity of a deposited film can be obtained using etch rate measurements. Highly strained, porous structures etch more rapidly than dense, strain-free materials. The acidic etchant chosen for the deposited silicon nitride films was buffered HF: (34.6 % (wt) NH_4F: 6.8 % (wt) HF : 58.6 % H_2O), which can etch LPCVD nitride at a rate of between 5 and 10 $Ås^{-1}$ [205]

It is important to remember that etch rate has a stronger dependence on film density than stoichiometry. Similarly, two different films can have the same refractive index value but very different densities. Therefore, it is necessary to take into account both refractive index and etch rate measurements to determine the true nature of a deposited film.

5.3 ELECTRICAL CHARACTERISATION

All electrical measurements of the a-Si:H and silicon nitride were carried out inside a light-tight box, using an HP 41040B picoammeter/voltage source controlled by a bespoke LabView environment. The a-Si:H films were deposited onto Corning 7059 substrates. A planar, aluminium gap cell was then thermally evaporated onto the surface of the films using an Edwards E306 coating system, with the dimensions being determined by a shadow mask. To investigate the electrical properties of the deposited nitride layers, MIS structures were fabricated by thermally evaporating aluminium dots of 1mm in diameter onto the upper surface of the silicon nitride. The accuracy of the picoammeter was ± 2%.

5.3.1 CONDUCTIVITY MEASUREMENTS

Photoconductivity is the change in the electrical conductivity of a material when it is exposed to electromagnetic radiation. Device quality a-Si:H has a room temperature dark conductivity of between 10^{-10} - $10^{-11}\Omega^{-1}cm^{-1}$, and a photosensitivity (the ratio of the photo- to dark-conductivity) of 5 to 6 orders of magnitude. In c-Si, illumination with photon energies higher than the bandgap promotes electrons into the extended states, thereby increasing the conductivity. The structural disorder in amorphous semiconductors relaxes the rules governing momentum conservation during photon-assisted transitions. This leads to an increase in optical absorption as compared to the crystalline state. However, the process of photo-generation of electrons is essentially the same, except that they need to be promoted above the material's mobility edge [41].

The experimental set-up used to investigate the conductivity of a-Si:H films grown in this work can be seen in Figure 5.2. The dark- and photoconductivity values were obtained by ramping the voltage across the gap cell from 0-50V at a constant rate of $1Vs^{-1}$. Resistances were calculated from the gradient of the generated I-V characteristics, and the resistivity was obtained by applying the equations described below. The light source used was an Oriel 96005 Uniform Illumination 150W solar simulator that produced a light intensity of A.M. 1.5 (100 $mWcm^{-2}$). The conductivity was then found by taking the reciprocal of the resistivity value. To ensure an accurate measurement, an average of four readings was taken for each sample.

$$\rho_{0-1} = R_{0-1}\left(\frac{A}{L}\right), \tag{5.8}$$

$$\rho_{0-2} = R_{0-2}\left(\frac{A}{2L+\Delta L}\right), \tag{5.9}$$

$$\rho_{0-3} = R_{0-3}\left(\frac{A}{3L+2\Delta L}\right), \tag{5.10}$$

where A is the product of film thickness and the length of the metal contacts. For homogenous material $\rho_{0-1} = \rho_{0-2} = \rho_{0-3}$.

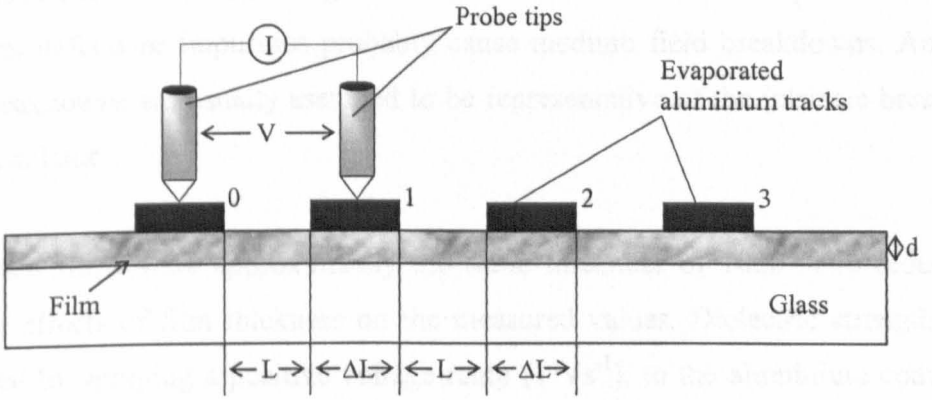

Figure 5.2 The gap cell technique used to evaluate the resistivity of a-Si:H

In an ideal MIS diode, it is assumed that the conductance of the insulating film is zero. However, in real insulators carrier conduction is possible when a sufficiently high electric field is applied to the structure. At the fields utilised in a-Si:H TFT operation

(i.e. ~ $1MVcm^{-1}$), both electron and hole conduction should be negligible at room temperature. In good quality silicon nitride, ohmic conduction is the dominant charge transfer mechanism at these electric field levels. Ohmic conduction occurs at low fields and temperatures by thermally induced hopping of electrons between energy states.

The resistivity of the nitride films was measured by applying a constant positive voltage ramp of $1Vs^{-1}$ to the top aluminium contact of the MIS structures, with the silicon substrate grounded. The film resistivity was extracted from the gradient of the I-V graph at an applied field of $1MVcm^{-1}$, which is consistent with TFT operation. For high quality silicon nitride, resistivities in the range 10^{14}-10^{15} have been quoted [205].

5.3.2 DIELECTRIC STRENGTH MEASUREMENTS

The dielectric strength of an insulating film is the maximum electric field in $MVcm^{-1}$ that can be applied across the material before breakdown occurs. This breakdown strength is limited by either thermal of electrical breakdowns. At room temperature, breakdown is almost entirely due to electrical processes.

There are three types of breakdown that can occur. Breakdowns that occur at low fields have been attributed to significant structural defects such as pinholes. Smaller structural defects or impurities probably cause medium field breakdowns. And high field breakdowns are usually assumed to be representative of the intrinsic breakdown of the insulator.

All nitride films were approximately the same thickness of 1000 Å to reduce any possible effects of film thickness on the measured values. Dielectric strengths were measured by applying a positive voltage ramp ($1\ Vs^{-1}$), to the aluminium contacts of the MIS structures with the substrate grounded until breakdown occurred. A number of MIS structures were tested on each silicon nitride sample and an average dielectric strength was calculated. High quality silicon nitride deposited by CVD has a dielectric strength of ~ $10\ MVcm^{-1}$ for a film thickness of 1000 Å [205].

5.3.3 INTERFACIAL CHARACTERISATION

The fixed charge density (Q_F cm^{-2}) of the PECVD silicon nitride and the interface state density (D_{it} $cm^{-2}eV^{-1}$) of the c-Si/nitride interface was examined using high frequency, capacitance-voltage (C-V) measurements on the MIS structures. The C-V measurements were made at a frequency of 1MHz using an HP4248 LCR meter controlled by a LabView programming environment. At this frequency, the interface states and minority carriers cannot respond quickly enough to the a.c. signal and therefore do not contribute to the measured capacitance. This measured value is due to the series combination of the fixed nitride capacitance and the semiconductor depletion layer capacitance. Even though the interface states make no direct contribution to the measured capacitance, they are still able to follow the d.c. ramping bias. Consequently, a change in the surface band-bending can occur which results in the C-V characteristic being streched-out to a certain degree.

At high frequency, the C-V graph comprises two regions – accumulation and depletion. For an n-type c-Si substrate, the application of a positive d.c bias to the top metal contact results in majority carriers (i.e. electrons) being attracted to the c-Si/insulator interface. This accumulation region produces a maximum in the measured capacitance which can be used to calculate the insulator permittivity, if the thickness of the insulator is known. As the bias is ramped to a negative value, the majority carriers are repelled from the interface and a depletion region comprised of ionised donors forms beneath the insulator. This depletion capacitance is in series with the insulator capacitance, which results in the total capacitance of the MIS structure decreasing until a certain maximum depletion width is formed. The bias is then ramped back to the positive starting voltage.

It is possible to obtain values for the fixed charge and interface state densities of the insulator by comparing the measured C-V data to the ideal characteristic [206]. The difference between the measured and the ideal flat-band voltage was used to estimate the fixed charge density using the following,

$$\Delta V = \Phi_{MS} - \frac{Q_F}{C_{max}}, \qquad (5.11)$$

where ΔV is the shift in the flat-band voltage, Φ_{MS} is the metal-semiconductor work function difference, Q_F is the fixed charge and C_{max} is the insulator capacitance per unit area. The degree of stretch-out in the characteristic allows the interface state density to be quantified [207]. High quality MIS structures of thermal oxide have fixed charge and interface state densities of 10^{10} and 10^{11} $cm^{-2}eV^{-1}$ respectively.

5.3.4 ELECTRICAL MEASUREMENT OF TFTs

All TFT characterisation measurements were performed using the same HP 4140B picoammeter and a light-tight metal box outlined above. This configuration eliminates any photo effects and provides electromagnetic shielding. The two voltage sources were connected to the gate and drain contacts while the source is grounded through the picoammeter. Contacts to the TFT were made through tungsten tipped microprobes. The chuck on which the TFT was placed is temperature controlled to provide a constant measurement temperature. A value of 40 °C was chosen as the preferred measurement temperature, as this was high enough to accommodate for any atmospheric variations in room temperature. All measurements were controlled by a LabView environment enabling all parameters to be set by the author before each test, and ensuring any measurements taken were easily repeatable.

To ensure that any gate leakage currents were negligibly small, every TFT had to be tested to confirm that the gate insulator was of sufficient quality. This was done by grounding the source and the drain and applying a constant gate voltage of 50 V. Any current flowing in this configuration was entirely due to gate leakage, and any TFT with a leakage current in excess of 1 pA was discarded. A summary of the basic characteristics measured in this work is given below.

5.3.4.1 TRANSFER CHARACTERISTICS

When measuring the gate transfer characteristic it is important to understand the processes occurring within the device during the application of the gate bias. When a positive voltage is applied to the gate contact the energy bands in the a-Si:H are pulled down at the a-Si:H/insulator interface, which draws electrons into the channel between

the source and the drain. If there is application of a prolonged gate bias, the device becomes more stressed, which can lead to threshold voltage shifts due to state creation. Conversely, if the ramping rate of the gate voltage is too quick, there is not enough time for the charge trapped in the deep states to thermalise, thus allowing the current transients to decay [208]. At low drain currents, this could cause the d.c. component of the source drain current to be dominated by transient responses.

In order to combat these problems, a voltage ramp of 1 Vs^{-1} and a small source-drain voltage (typically 2V) were used. This ensured that there was a sufficient delay between each voltage step so that the device had the opportunity to approach equilibrium. The voltage ramp was from some minimum (usually negative) value up to some maximum voltage greater than the threshold voltage of the TFT. To alleviate problems of excessive device stressing during measurement, the drain current flowing through the TFT was limited to a maximum value (typically 10nA). All measurements are a compromise between low current resolution, level of device stressing and the time taken for each measurement. Longer delay times would help thermalisation of the deep states, but would mean prolonged stressing of the device.

In the gate transfer characteristic, the gate voltage is varied whilst the drain voltage is kept constant, and the drain current is then measured. From these measurements, it is possible to extract the off current, the on/off ratio, the pre-threshold slope, threshold voltage and the field effect mobility. Drain transfer characteristics may be used to check the contacts for ohmic behaviour. The drain current is measured as the drain voltage is varied, with the gate voltage kept constant.

The characteristics can be plotted on a logarithmic or linear scale of source-drain current. A log plot can be used to deduce the sub-threshold conduction regime. A linear plot can be used to calculate the threshold voltage and the field effect mobility. The slope for the plot is proportional to the mobility and the intercept with the induced charge axis is proportional to the threshold voltage.

In this work, only linear field effect mobilities are considered. The mobility measured in the saturation region is often quoted, but a-Si:H TFTs are never operated in this

region for any practical application. Therefore, only the mobilities calculated from the linear region are included here.

5.3.4.2 OUTPUT CHARACTERISTICS

The output characteristics were measured by applying a series of above threshold, gate voltages to the TFTs. For each gate voltage the drain voltage was ramped from zero volts up to some maximum value at a ramp rate of $1Vs^{-1}$. By studying the set of curves that result, it is possible to identify any current crowding problems arising from non-ohmic source-drain contacts or a large DOS in the bulk of the a-Si:H .

5.3.5 ASSESSMENT OF TFT STABILITY

A-Si:H TFTs exhibit threshold voltage shifts after prolonged applied bias to the gate electrode. The two mechanisms thought to be responsible for this shift are charge trapping in the gate insulator, and defect creation in the a-Si:H [§ 3.5]. In device quality silicon nitride state creation in the a-Si:H layer dominates at low positive biases, whilst at high gate biases charge trapping is the pre-eminent process. In thermally grown silicon dioxide, state creation is dominant for all gate voltages. As state creation occurs in all devices it is a property of the amorphous layer rather than the insulator layer. Optimisation of the insulator can eliminate a significant proportion of instability that is the result of charge injection, but state creation instability cannot be altered to any substantial degree, regardless of any improvement in the gate insulator.

In this thesis, the stability of a-Si:H TFTs was not the primary focus of the investigations. There is no facility to produce p-channel devices within EMTERC, due to the unavailability of a suitable dopant source. In addition, the temperatures required to facilitate aluminium diffusion into an intrinsic layer of a-Si:H, hence creating a p-channel device, are higher than the target deposition temperatures for a-Si:H in this work. Therefore, it was not possible to distinguish between state creation and charge-trapping as the primary source of the instability. However, as device stability is of vital importance in both standard and low temperature TFTs, a series of investigations were undertaken using the following method.

Bias stressing experiments of selected n-channel devices were carried out in order to study the extent of any threshold voltage shift. A low, positive gate bias of 30V was used in all cases. This corresponds to an applied electric field of 1 $MVcm^{-1}$ across the gate insulator material, commensurate to the fields required for a-Si:H TFT operation. A bias of 1V was also applied to the drain contact for a series of stress times. All gate transfer measurements were made at 40 °C, and were taken both before and after stressing.

Chapter 6

Experimental optimisation of a-Si:H films grown by PECVD with source gas heating

6.1 INTRODUCTION

This chapter describes system evaluation and experimental optimisation of the low temperature PECVD a-Si:H films intended for device application within an overall thermal budget of 125 °C. The a-Si:H material was optimised empirically using a set of 'standard conditions' deduced from an extensive review of the literature and initial characterisation measurements on a number of trial samples. Each factor controlling deposition was then varied, in turn, around the 'standard' values, with the others held constant. The resultant changes in film properties were then monitored using the characterisation techniques set out in Chapter 5. The only process variables that remained constant throughout this optimisation process were the plasma excitation frequency (13.56 MHz) and the electrode separation (3 cm).

6.2 SYSTEM EVALUATION

Before any in-depth investigations could take place, it was necessary to test all aspects of the new system to ensure that process runs could be carried out adequately and reproducibly.

A primary concern was to ensure that the vacuum system was leak tight, so that the base pressure within the chamber could be as low as possible, thereby keeping the level of water vapour and atmospheric contaminants to a minimum. As the new apparatus utilised the existing root/rotary pumping combination, it would be reasonable to assume that if the minimum achievable base pressure of the novel chamber was commensurate to that of the original commercial OPT system, all vacuum connections could be said to be leak tight, to within manufacturer

specifications. This was confirmed, as the disparity between the pressure gauges in the respective systems was < 10 mTorr.

Once the integrity of the vacuum connections had been verified, it was important to check that a stable pressure could be maintained once the source gases were flowing into the reactor, via the gas inlet assembly. The use of a diaphragm valve to control process pressure might seem somewhat crude, however, as normal process pressures were between 0.1 – 1 Torr, it was perfectly adequate.

Modifications were made to the source gas line and RF signal input of the existing PECVD system, so that the low temperature chamber could utilise the same flow rate control mechanisms and RF generator unit/matching network. Whilst these modifications had no effect on flow control (the same level of regulation was achievable in both reactors), it was never possible to attain the same very low levels of reflected power in the new deposition system as compared to the OPT μP 80. This meant that in certain regions of parameter space, there was insufficient power coupled to the system to strike a plasma. This occurred when low powers (<5W) were used in conjunction with medium-high pressures (> ~ 700mTorr). For the results described here, the reflected power in the system was never more than ~ 5 % greater than that in the OPT reactor.

As has been discussed earlier, substrate temperature plays a pivotal role in the physical and electrical properties of a-Si:H grown by PECVD. Therefore, as the primary aim of this work was to investigate the effect of pre-heating the source gases on the properties of the a-Si:H films, it was important to monitor any changes in substrate temperature as a result of gas heating. It has been reported that turning on a gas heater increases substrate temperature, T_s, due to thermal radiation [196]. Consequently, to study any changes in T_s as heated gas was introduced into the chamber, a thermocouple was attached to a dummy silicon wafer by heat sink compound and any change in substrate temperature recorded. Any significant changes in T_S because of gas line heating would obviously affect the stated aim of the optimisation process. Temperatures were measured using the gas flow rates described in the 'standard conditions' in table 6.1 below, and the measurements made at room

temperature at the base pressure of the system (~ 10^{-3} Torr). **The gas line was held at the desired temperature for a period of 2 hours, and T_s measured after the heated gases had been introduced into the system for a period of 30 minutes. This allowed T_s to stabilize after the initial gas injection. The results of these tests can be seen in Figure 6.1.**

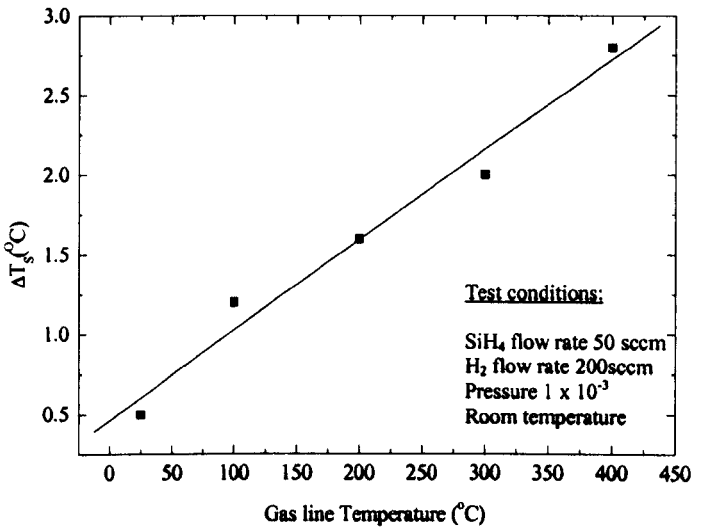

Figure 6.1 The variation in substrate temperature with gas line temperature

It is shown that there is a minimal increase in substrate temperature for all gas line temperatures. This demonstrates that T_S is relatively unaffected by thermal radiation from the gas line heater.

6.3 EXPERIMENTAL OPTIMISATION OF a-Si:H

To allow film properties to be compared as reliably as possible, all a-Si:H films were deposited to approximately the same thickness (~0.5 μm). It has been shown that the gap cell arrangement used here for conductivity measurements, can result in thickness dependent variations in the electrical properties [209]. These variations can mask changes in the film properties that could otherwise be attributed to alterations in the deposition conditions.

Table 6.1 Standard deposition conditions used during optimisation of a-Si:H

Deposition Variable	Condition
Temperature (°C)	75
Pressure (mTorr)	300
RF Power (W)	10
SiH_4 Flow Rate (sccm)	50
H_2 Flow Rate (sccm)	200

Investigation of the low temperature a-Si:H took place in two stages. The first stage involved the empirical studies using the methodology outlined above. The conditions that yielded the 'best' quality material from this phase were then used as the base conditions for the source gas heating experiments. As the in-house system was being utilised for the first time, the author felt it was vital to undertake extensive initial investigations in an effort to ascertain the efficacy of the experimental design. It was thought that this sequence of enquiry would yield the most useful information concerning the effect of pre-heated source gases as a deposition variable.

The following sections describe the effects of individual process variables on the physical and electrical properties of PECVD a-Si:H films grown in the novel system without source gas heating.

6.3.1 SILANE FLOW RATE

The flow of SiH_4 (Air Products – Semiconductor grade) into the reaction vessel varied from 10 to 100 sccm; the latter was the maximum flow rate attainable from the MFC. The change in the properties of a-Si:H with SiH_4 flow rate with all other deposition parameters held constant can be seen in Figure 6.2.

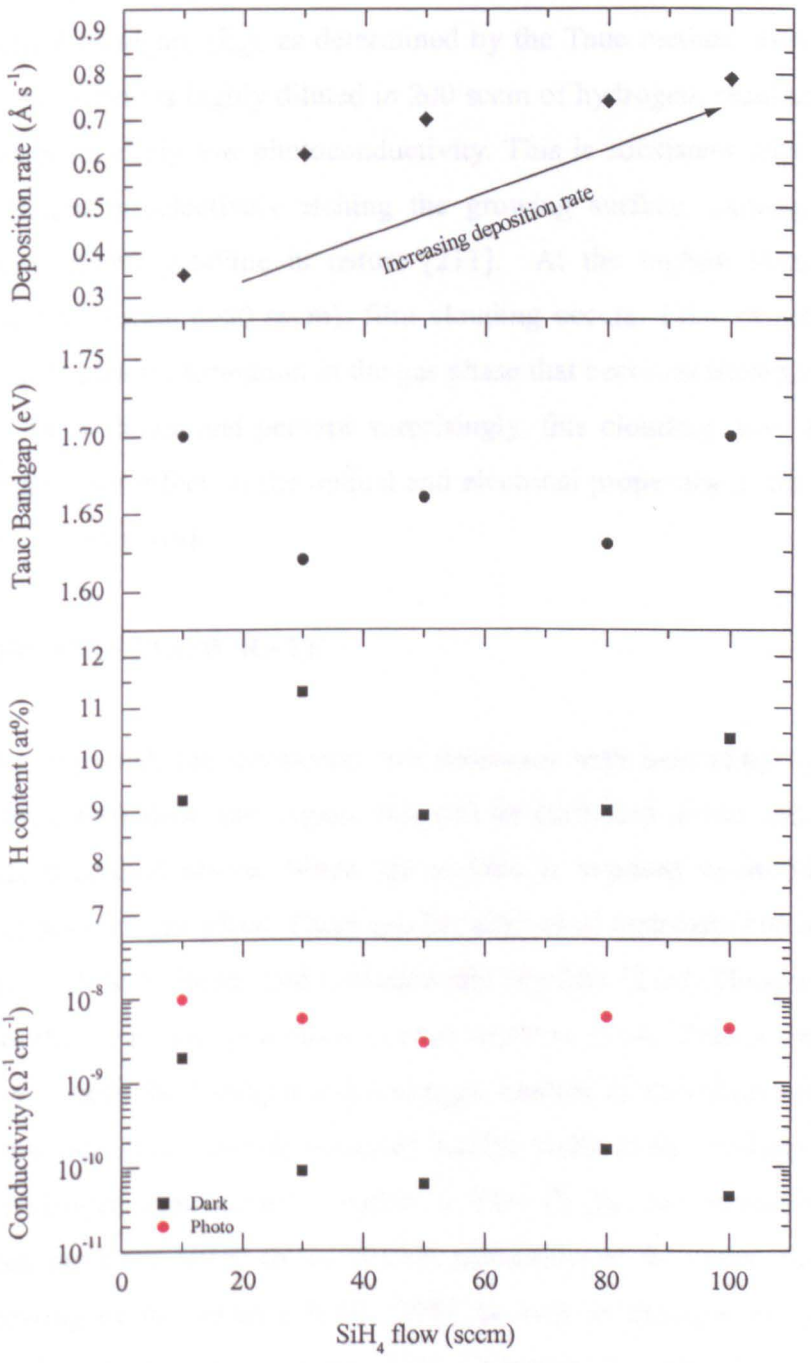

Figure 6.2 The effect of silane flow rate on the properties of a-Si:H

It can be seen that the deposition rate increases with SiH_4 flow rate. This is expected, as at higher gas flows there is reduced gas depletion within the reactor. This is determined by the gas residence time, which is a function of flow rate and reactor geometry [210].

Within the range investigated, silane flow had little effect on the hydrogen content, (C_H), or optical bandgap, (E_g), as determined by the Tauc method. However, at low flows rates, the silane is highly diluted in 200 sccm of hydrogen, resulting in material that exhibits particularly low photoconductivity. This is consistent with the idea that atomic hydrogen is selectively etching the growing surface, causing the film to become more microcrystalline in nature [211]. At the highest silane flow rates attainable in the system (>80 sccm), film clouding occurs. Film clouding has been linked to a-Si:H powder formation in the gas phase that becomes incorporated into the film [212]. As is shown and perhaps surprisingly, this clouding does not appear to have any significant effect on the optical and electrical properties of the a-Si:H films deposited during this work.

6.3.2 HYDROGEN FLOW RATE

As might be expected, the deposition rate decreases with increasing hydrogen (Air Products Grade 6.0) flow rate. Again, this can be attributed to the action of atomic hydrogen as described above. When the surface is exposed to atomic hydrogen, several reactions can take place. There can be removal of hydrogen bonded to silicon, breakage of weak Si-Si bonds and diffusion into the film [213]. These modifications can promote the formation of a more relaxed structure [214]. This is consistent with the decrease in both the bandgap and hydrogen content of the films with increasing hydrogen flow rate. It is generally accepted that the width of the bandgap is dependent upon the hydrogen concentration within a film [215]. An increasing hydrogen concentration has been linked to the upward movement of the conduction band edge and a narrowing of the valence band [216], as well as changes in the strain and disorder of the amorphous network [217]. Therefore, a reduction in the optical bandgap can be attributed to a reduction in the total hydrogen concentration. Figure 6.3 confirms that a reduction in hydrogen content results in a concurrent reduction in the optical gap and vice versa.

Films grown in a pure silane plasma have a very low photosensitivity. However, as hydrogen is included into the deposition process, the photosensitivity increases rapidly. Very-low deposition temperatures inhibit structural rearrangement of the growing surface. However, with the addition of hydrogen as a source gas, impinging

hydrogen atoms can supply energy to this surface, mediating the growth process and helping to remove or passivate defects.

It has been suggested that the film properties are governed by a competition between the rate of film growth and the rate of thermally activated surface reactions at or near the growing surface [218]. Essentially, this means that the deposition rate and the substrate temperature effectively determine the quality of the film. Therefore, at low deposition rates, there is more time for surface reactions to occur. In this work, the decreasing values of C_H and E_g with a decreasing deposition rate seem to support this theory (Figure 6.3).

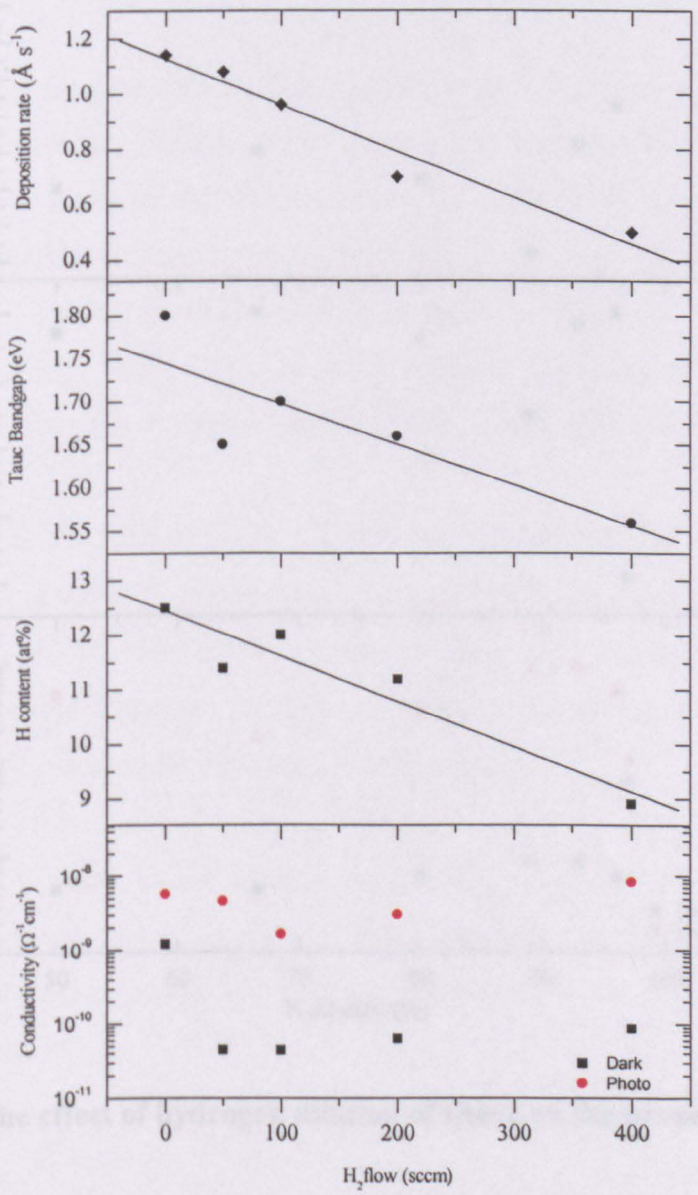

Figure 6.3 The effect of hydrogen flow rate on the properties of a-Si:H

In an effort to better understand the role of hydrogen gas within the deposition process, a series of samples were deposited at different hydrogen dilution ratios, with the dilution ratio of hydrogen, (γ), given by,

$$\gamma = \frac{H_2(sccm)}{H_2(sccm) + SiH_4(sccm)} \tag{6.1}$$

The properties of these films are summarised in Figure 6.4.

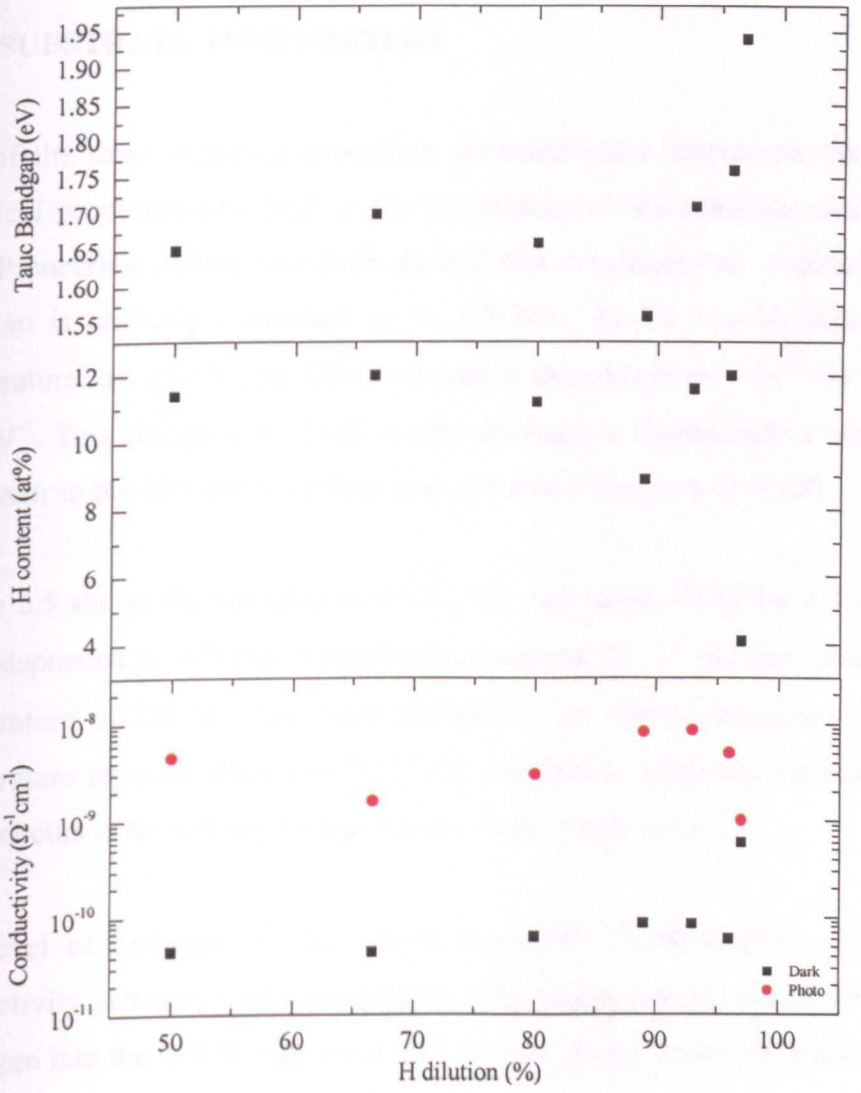

Figure 6.4 The effect of hydrogen dilution of silane on the properties of a-Si:H

As γ increases above 95%, the film undergoes an amorphous to microcrystalline transition, (μc-Si), as evidenced by the high value of Eg and the very low

photoconductivity. This transition appears to be very abrupt (within 1-2%), and is in agreement with Alpium et al [186]. That study also found that the value of γ that facilitates the change in phase of the material is also substrate temperature dependent, and increases with decreasing temperature. Exploring the properties of films deposited on the edge of crystallinity is not within the remit of this thesis. However, films deposited in this region (referred to as polymorphous silicon) have a high degree of microstructure, similar to μc-Si films, and have improved transport properties and stability with respect to a-Si:H [219].

6.3.3 SUBSTRATE TEMPERATURE

One of the most important deposition parameters that determines the physical and electrical properties of a-Si:H is the temperature of the substrate during deposition (T_S). Pioneering studies on a-Si:H showed that the density of localised states in the bandgap is critically controlled by T_S [2][220]. As T_S was increased from room temperature to ~ 250 °C, the DOS was seen to decrease from > 10^{18} $cm^{-3}eV^{-1}$ to ~10^{16} $cm^{-3}eV^{-1}$. This change in the DOS can be attributed to fundamental structural changes that occur in the film due to surface and subsurface reactions (§ 4.3.2).

Figure 6.5 shows the variation of the E_g, C_H and conductivity for a series of a-Si:H films deposited at substrate temperatures between 25 °C and the maximum system temperature of 150 °C. The linear decrease in the optical bandgap with increasing temperature reported elsewhere [221] was confirmed. Similarly, the maximum value of C_H occurs in those samples deposited at room temperature.

The level of hydrogen in the film is reasonably constant above 25 °C, yet the conductivity increases with increasing T_S. This suggests the mode of incorporation of hydrogen into the a-Si:H matrix has a pronounced effect on the electronic behaviour.

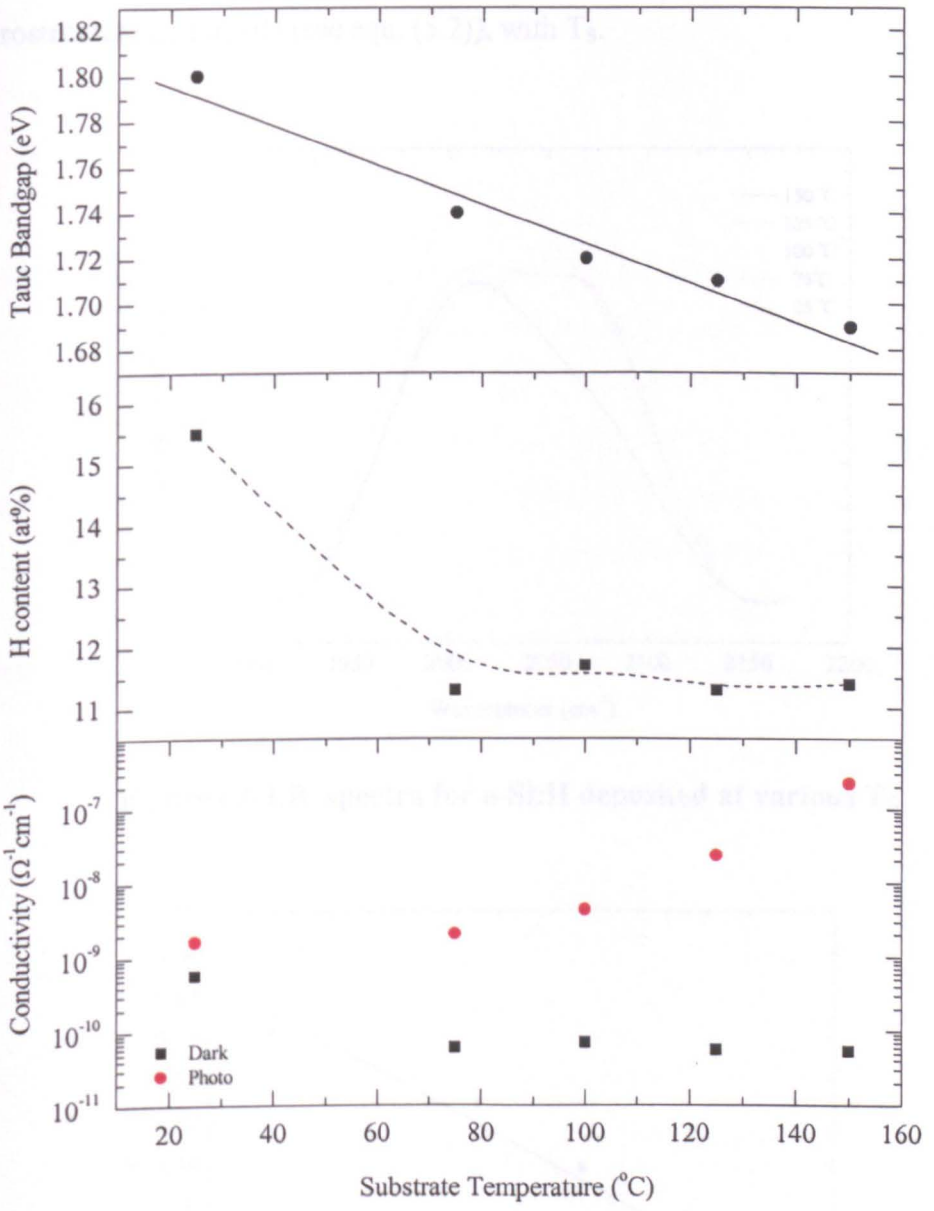

Figure 6.5 The effect of substrate temperature on the properties of a-Si:H

This is demonstrated in the I.R. spectra shown in Figure 6.6. The variation in the hydrogen bonding configuration with T_S is evident from the change in the absorption band in the range 2000 – 2100 cm^{-1}. This band includes vibrational contributions from $Si\text{-}H_2$ and $(Si\text{-}H_2)_n$ stretching modes as detailed in Table 5.1 (§ 5.2.1). As T_S increases, the peak shifts from ~ 2080 cm^{-1} to ~2010 cm^{-1}. This signifies a reduction in the level of dihydride bonding within the film, with a concurrent increase in the

monohydride fraction. This is verified in Figure 6.7 which shows the variation in microstructure factor, (R) (see equ. (5.2)), with T_S.

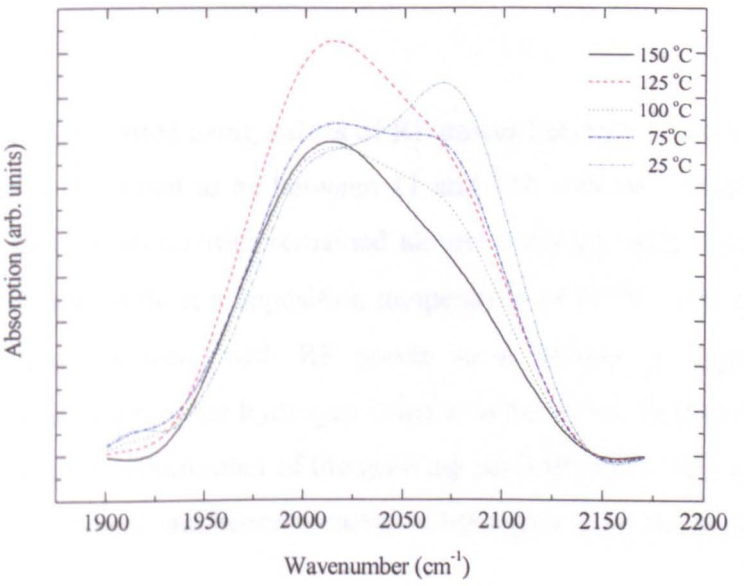

Figure 6.6 I.R. spectra for a-Si:H deposited at various T_S

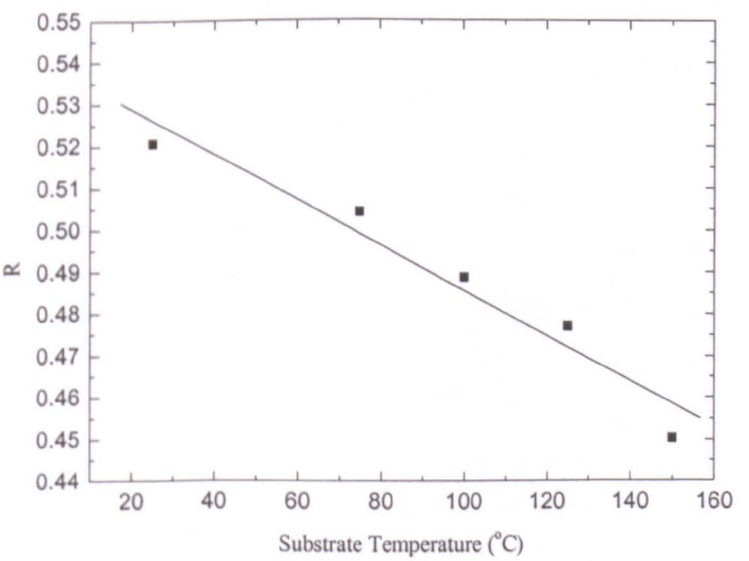

Figure 6.7 The variation in microstructure factor (R) with T_S

The low level of monohydride bonding at very low deposition temperatures, results in a comparatively high density of unpassivated dangling bonds. This leads to a degradation in the electrical properties of a-Si:H. At 25 °C the photosensitivity, (σ_D/σ_{PH}), is less than 1 order of magnitude. But as T_S reaches the maximum value of

150 °C, this increases rapidly to approximately 4 orders of magnitude as the concentration of dangling bonds is reduced.

6.3.4 POWER

A-Si:H films were deposited using values of RF power between 5 and 50 W, equating to power densities estimated to be between 11 and 110 $mWcm^{-1}$. Within this range, the dark- and photo-conductivities remained almost constant, with a photosensitivity of ~ 2 orders of magnitude at a deposition temperature of 75 °C. The Tauc band gap increases and then decreases with RF power as is shown in Figure 6.8, again demonstrating the changes in the hydrogen content of the films. Higher powers lead to an increase in the ion bombardment of the growing surface [222]. This in turn leads to increased levels of etching and hence removal of hydrogen from the material.

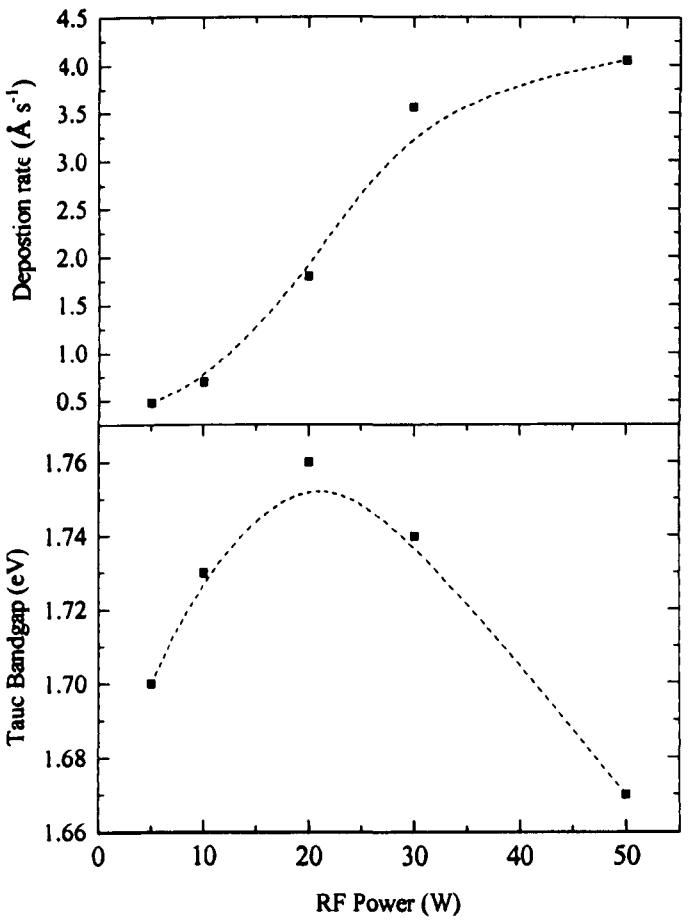

Figure 6.8 The effect of RF Power on the properties of a-Si:H

This is further demonstrated by the non-linear increase in the deposition rate. Initially, the deposition increases with RF power. This is because of the SiH_4 being strongly dissociated that results in an increase in the flux of film-forming precursors towards the substrate surface. However, at high power levels, there is a depletion of the source gas, and an increase in hydrogen flux at the substrate that reduces the deposition rate due to the etching effect of the impinging species.

Using relatively low chamber pressures (< ~ 1 Torr), the use of high RF power densities is generally avoided for the production of good quality a-Si:H. Strongly dissociated silane contains a majority of SiH_2 units which causes an increase in the DOS [223]. In addition, more highly reactive species are involved in the deposition and gas phase reactions leading to polymerisation and powder or dust formation. These reactive species have a high sticking coefficient and low surface mobility [34], which can result in porous, low quality material, with a columnar morphology [224] and poor electronic properties.

6.3.5 PRESSURE

The chamber pressure determines the mean free path for collisions of the gas molecules and influences whether the reactions are at the growing surface or in the gas phase [34]. Higher pressures result in a shorter mean free path and more gas phase reactions [225]. This also leads to a reduction in ion bombardment of the growing surface, and results in a transition between the α and γ regimes (§ 4.3.1.3). Figure 6.9 shows the variation in the deposition rate with chamber pressure. After an initial increase between 100 and 300 mTorr, the deposition rate decreases as more dissociative reactions take place, and the silane source gas is depleted.

Within the range investigated, there was no significant pressure dependence of the a-Si:H material properties. However, it should be noted that it was during pressure investigations that the most problems occurred with effectively matching the RF signal. Unfortunately, this prevented any pressures above 1 Torr being explored, as the reflected power was too high to efficiently couple the desired power to the system.

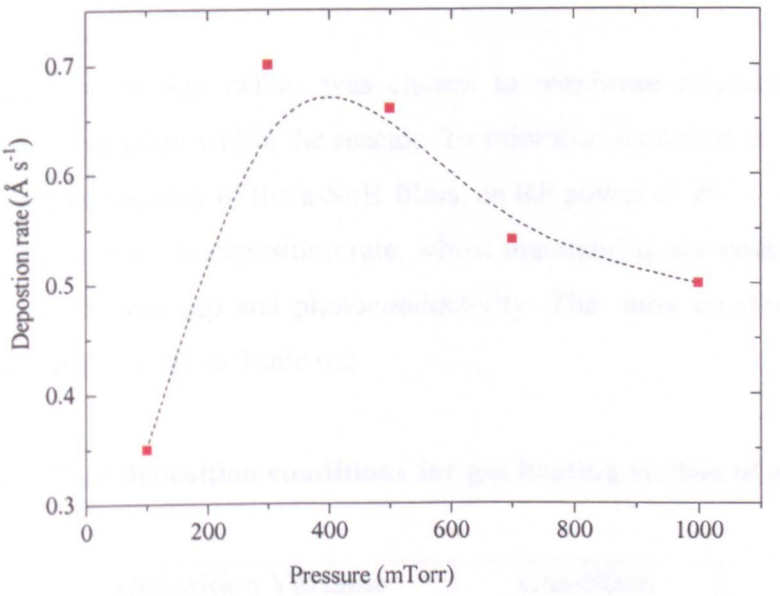

Figure 6.9 The variation of deposition rate with chamber pressure (line drawn as guide for the eye

6.4 SUMMARY OF INITIAL OPTIMISATION

In choosing the initial optimised deposition parameters, a number of factors had to be considered. Firstly, and most important, was the substrate temperature during deposition. During the evaluation process, it became clear that producing satisfactory films under 100 °C would not be possible within the explored parameter space. From conductivity measurements, the maximum photosensitivity achieved was ~ 2 orders of magnitude at 75 °C, regardless of any changes made to other parameters. Therefore, the substrate temperature chosen was determined by the maximum photolithographic processing temperature for TFTs incorporating these films that were to be fabricated in EMTERC. This was 125 °C, and was the hard bake temperature of the photoresist.

For the remaining parameters, a compromise had to be made between material properties and deposition rate. For very high levels of hydrogen flow rate (> 90%) and hence high dilution of the silane, the physical and electrical properties are poor, with a high Tauc bandgap, and very low photosensitivity. The same is true for low hydrogen dilution, even though the deposition rate approaches its maximum values.

Consequently, a dilution of silane of 90% was chosen, with the flow rate capabilities of the MFCs determining the exact flow rates of the source gases.

A chamber pressure of 300 mTorr was chosen to maximise deposition rate and minimise powder formation within the reactor. To minimise inclusion of Si-H_2, hence reducing the level of porosity of the a-Si:H films, an RF power of 20 W was selected. This resulted in a reasonable deposition rate, whilst maintaining acceptable values for hydrogen content, optical gap and photoconductivity. The 'base conditions' for the gas heating tests are detailed in Table 6.2.

Table 6.2 Base deposition conditions for gas heating studies of a-Si:H

Deposition Variable	Condition
Temperature (°C)	125
Pressure (mTorr)	300
RF Power (W)	20
SiH_4 Flow Rate (sccm)	40
H_2 Flow Rate (sccm)	400

6.5 SOURCE GAS HEATING INVESTIGATIONS

Using these base conditions, a series of samples was deposited using gas line temperatures ranging from room temperature to 400 °C, as measured by the thermocouple attached to the input gas line. The results of these process runs and the changes in material properties with gas line temperature can be seen in Figure 6.10. Within the limits explored, changes in gas line temperature have no measurable effect on the deposition rate of the a-Si:H material, with the average deposition rate being approximately 1.05 $Å s^{-1}$. This is contrary to previous work, where the deposition rate was found to decrease with increasing gas line temperature [197]. Lower deposition rates can mean greater time on the growing surface for the film-forming radicals to find their optimum bonding site. Any changes in deposition rate of a film with process parameters must therefore be carefully considered. The fact that gas heating does not

significantly affect the deposition rate of the a-Si:H in this work demonstrates that any changes in the physical and electrical properties of the material cannot be attributed to variations in deposition rate within the explored parameter space.

The reduction in the level of hydrogen reduces the optical gap of the material, which also leads to an increase in the photoconductivity. These results suggest that the application of thermal energy to the film-forming precursors modifies the growth process.

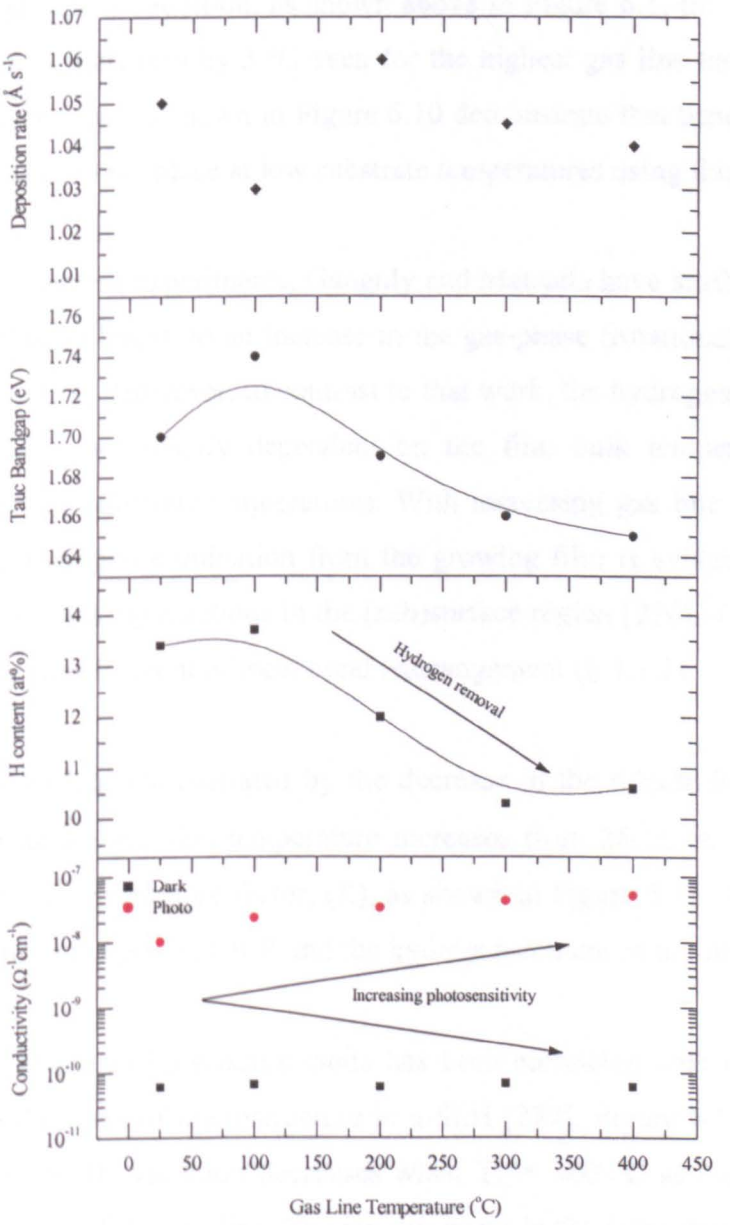

Figure 6.10 The effect of gas line temperature on the properties of a-Si:H

As the growth temperature is lowered, the surface diffusion length of the precursors also decreases. This prevents the adsorbed species from finding their energetically favourable sites, and results in poor quality material. This has been attributed to a reduction in the surface diffusion coefficient and the staying time of the precursor on the surface [153]. Therefore, it appears that preheating the source gases enhances the diffusion of species on the growing surface. Ordinarily, in order to obtain a larger diffusion coefficient, and hence a less defective material, the surface temperature is raised. However, the surface temperature remained constant at 125 °C throughout these investigations. In addition, as shown above in Figure 6.1, the substrate surface temperature only increased by 3 °C even for the highest gas line temperature of 400 °C. Therefore, the results shown in Figure 6.10 demonstrate that beneficial deposition phase reactions can take place at low substrate temperatures using this technique.

Using cathode-heating experiments, Ganguly and Matsuda have attributed an increase in surface diffusion length to an increase in the gas-phase (rotational) temperature of the precursors [153]. However, in contrast to that work, the hydrogen content of films deposited here is not wholly dependent on the film bulk temperature (which is determined by the substrate temperature). With increasing gas line temperature, the promotion of hydrogen elimination from the growing film is evident, suggesting an increase in cross-linking reactions in the (sub)surface region [226]. This is in addition to the possible enhancement of local bond rearrangement (§ 4.3.2).

This effect is further demonstrated by the decrease in the dihydride (SiH_2) bonding configuration as the gas line temperature increases from 25 °C to 400 °C, and the decrease in the microstructure factor, (R), as shown in Figure 6.11. The SiH_2 content is calculated from the product of R and the hydrogen content in the films.

The intensity of the Si-H_2 scissors mode has been correlated with the void fraction and therefore the level of microstructure in a-Si:H [227]. Figure 6.12 shows that the intensity of the Si-H_2 vibration decreases when T_L = 400 °C as compared to when there is no heating of the gas line. The improvement in the microstructure factor with a heated source gas line illustrates the reduction in the void fraction, and is similar to previous work [197].

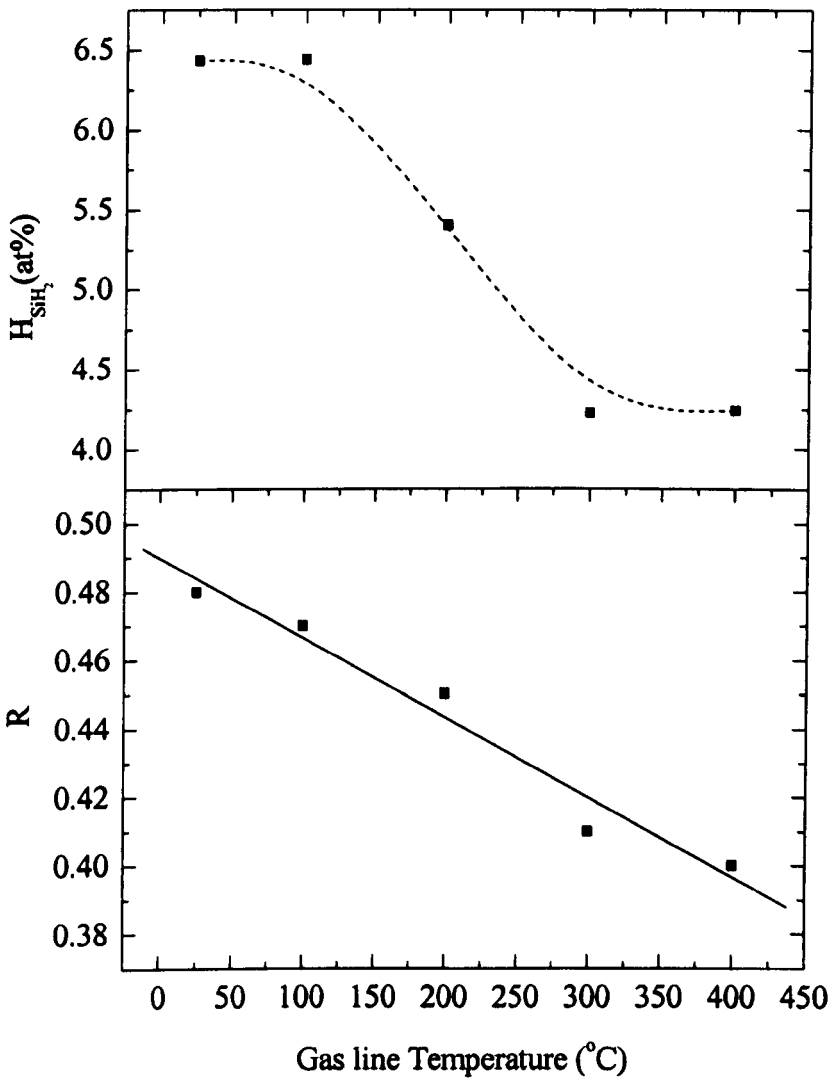

Figure 6.11 The effect of gas line temperature on dihydride content and microstructure factor (R)

In those studies, a combination of cathode heating and pre-heating of the source gases was used at a substrate temperature of 180 °C. It was argued that preheating the gas mixture raised it to a higher vibrational energy state so that the reaction $SiH_4 \rightarrow SiH_3 + H$ was energetically more favourable than $SiH_4 \rightarrow SiH_2 + H_2$. This then reduced the level of gas phase polymerisation within the reactor, which appeared to improve the properties of the deposited films.

A reduction of polymeric deposits on the walls of the chamber with gas heating was also of feature of this work. However, without any in-situ diagnostic facilities, it was

not possible to determine the individual contribution of the various gaseous species in the plasma.

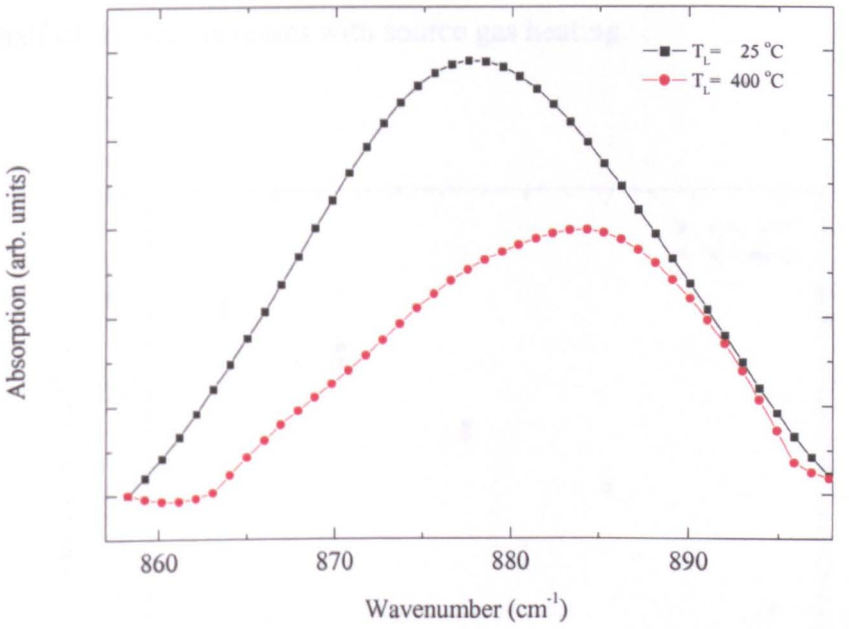

Figure 6.12 IR absorption spectra of Si-H_2 scissors mode for a-Si:H films grown with T_L = 25 °C and 400 °C

Above or near room temperature, good quality a-Si:H, with a low density of localised states in the energy gap has a thermally activated dark conductivity consistent with extended state conduction (§ 2.4.2). The approximate position of the Fermi level can be determined by measuring the activation energy (E_A), of the dark conductivity using the following relation,

$$\sigma = \sigma_0 \exp[-(E_A)/kT] \qquad (6.2)$$

where σ_0 is the conductivity prefactor, k is Boltzmann's constant and T the measurement temperature. Arrhenius plots for a-Si:H films deposited with different T_L values can be seen in Figure 6.13. The calculated activation energies are 0.73 and 0.77 eV for T_L = 400 and 25 °C respectively. The variation in activation energy with T_L is further illustrated in Figure 6.14. It can been seen that the a-Si:H material becomes slightly more n-type with increasing T_L. The defect pool model states that only defects with the lowest activation energies actually form (§ 2.5.4). Therefore, as

the Fermi level moves closer to the mobility edge (hence making the material more n-type), the density of defect states in the lower half of the energy gap increases. Consequently, from Figure 6.14, it could be argued that the density of defects in the lower half of the gap increases with source gas heating.

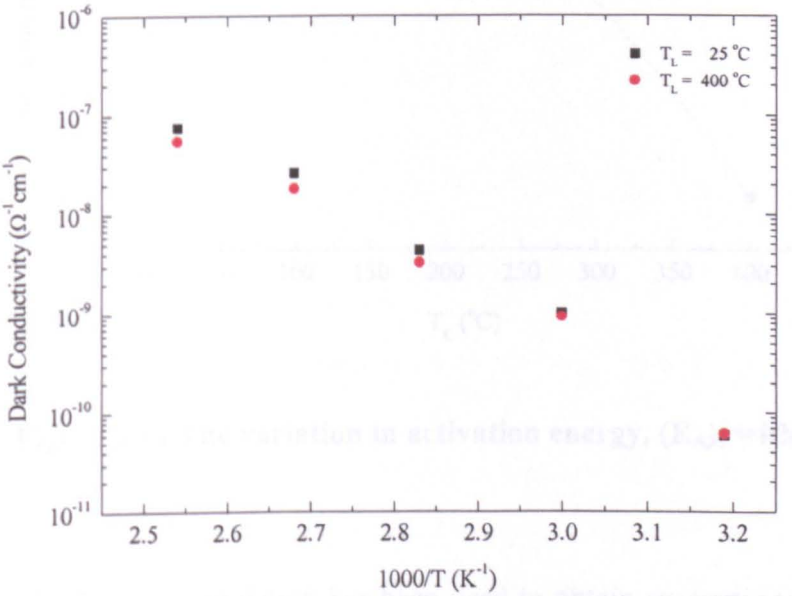

Figure 6.13 Arrhenius plots for a-Si:H deposited with different values of T_L

In order to test this hypothesis, it would be necessary to undertake some experiments to accurately measure the defect density throughout the bandgap. However, the results presented here demonstrate the intrinsically n-type nature of the low temperature a-Si:H films deposited in this work (assuming an optical bandgap of ~ 1.70 eV).

An aspect of a-Si:H that is fundamental to its electrical properties, is the range of structural disorder. Without experimental facilities such as Photothermal Deflection Spectroscopy (PDS) or the Constant Photocurrent Method (CPM) being available, it was not possible to investigate the exponential slope of the valence band tail and hence evaluate the Urbach energy values of the films. In good quality a-Si:H, the Urbach edge is usually between 50 – 100 meV, and increases with higher levels of structural disorder. Nevertheless, by using the UV/VIS optical absorption data, it is possible to assess the range of disorder in amorphous materials [228].

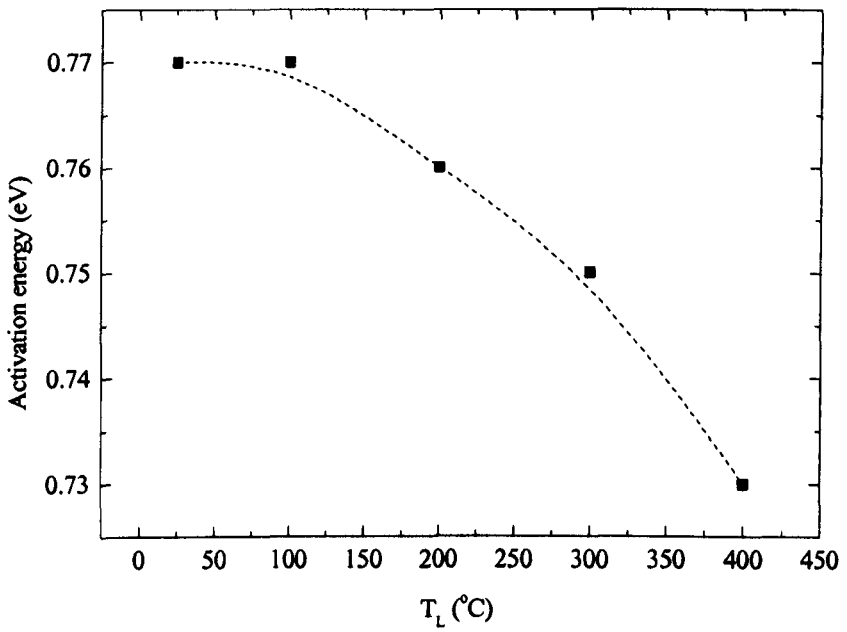

Figure 6.14 The variation in activation energy, (E_A), with T_L

Previously, the Tauc extrapolation has been used to obtain an empirical value for the optical bandgap (§ 5.2.2), using the following relation (§ equ. 5.3),

$$[\alpha(E)h\nu] = C_{TAUC}\{h\nu - E_o\}^2$$

However, the slope of the extrapolation, C_{TAUC}, is also taken as a measure of the intermediate range order, with greater order corresponding to larger C_{TAUC} [229][230][231]. Figure 6.15 illustrates the relationship between C_{TAUC} and gas line temperature T_L.

It can be seen that C_{TAUC} is approximately 500 $cm^{-1/2}eV^{-1/2}$ for $T_L \leq 200$ °C, but then increases to a maximum of 521 $cm^{-1/2}eV^{-1/2}$ at $T_L = 400$ °C. This suggests that the amorphous network becomes more ordered as the hydrogen content decreases with an increasing T_L. To investigate this further, the optical characteristic, B, was calculated ($B = C_{TAUC}^2$). This describes the shape of the band edges and is related to the level of disorder [228]. The correlation between B and the hydrogen content and bonding configuration is shown in Figures 6.16 and 6.17.

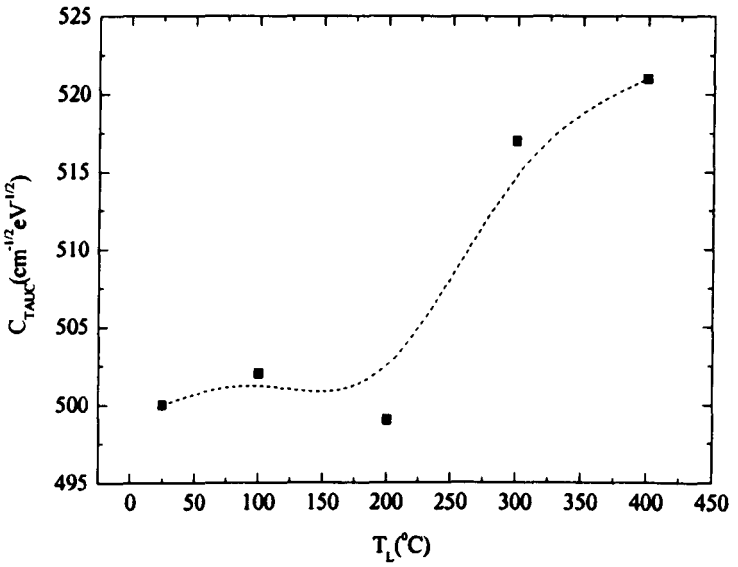

Figure 6.15 The variation of C_{TAUC} with T_L

An increase in the hydrogen content results in a decrease of B. It then follows that the same relationship exists between B and the microstructure factor, as the concentration of clustered monohydride and dihydride bonds increases. This is logical given the results detailed above.

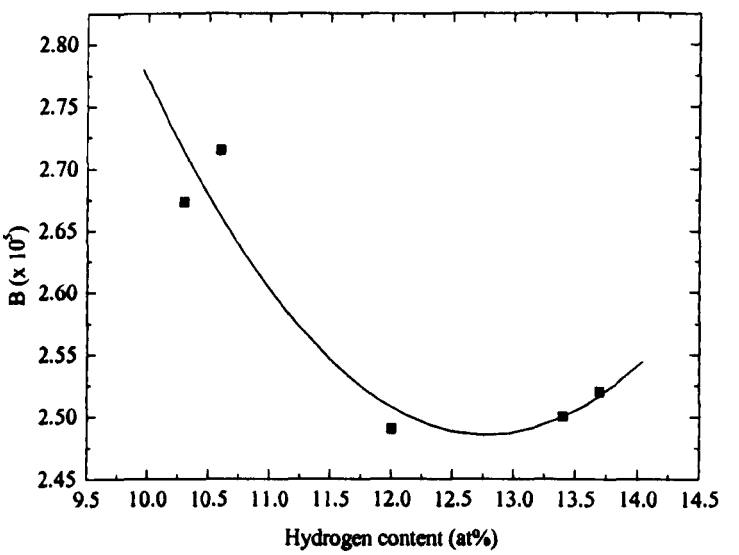

Figure 6.16 The relationship between optical characteristic, B, and hydrogen

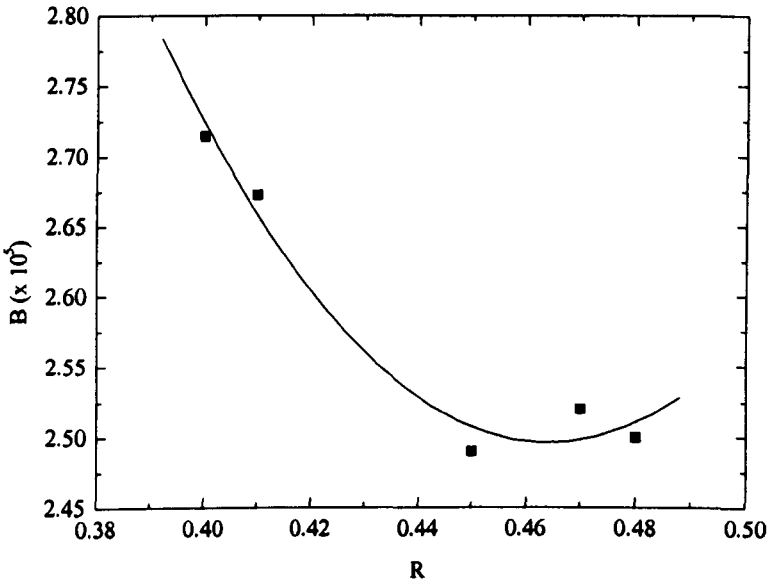

Figure 6.17 The relationship between optical characteristic, B, and microstructure factor R

The implication is that there is a narrowing of the band tail state distribution and consequently a sharpening of the band edges with increasing T_L. This correlates well with the observed increase in photoconductivity of films deposited with source gas heating.

6.6 PROPERTIES OF OPTIMISED A-Si:H GROWN WITH SOURCE GAS HEATING

The properties of the optimised a-Si:H layers grown with source gas heating at 125 °C are detailed in table 6.3, and are compared with films deposited at 300 °C.

A number of the properties of the material deposited with source gas heating are commensurate to that of the high temperature film. However, the obvious discrepancy is the photosensitivity value. It is far lower than would be predicted simply by looking at the other material properties.

Table 6.3 Comparison of material properties for standard and gas-heated a-Si:H

Material parameter	300°C PECVD	125 °C GH-PECVD
Tauc Bandgap (eV)	1.75	1.66
Hydrogen content (at%)	10	10.5
Activation energy (eV)	0.85	0.73
Dark conductivity ($\Omega^{-1}cm^{-1}$)	1×10^{-11}	6×10^{-11}
Photosensitivity	$\sim 1 \times 10^{6}$	$\sim 1 \times 10^{3}$

This suggests that the mid-gap density of states in the low temperature, gas heated film is higher relative to the standard temperature film. Therefore, in an effort to understand more thoroughly the properties of the gas heated a-Si:H, and the possibility of its use in device applications, a series of TFTs were fabricated incorporating this material. The results of these investigations are detailed later in this thesis (§ 8).

Chapter 7

Plasma Enhanced Chemical Vapour Deposition of Silicon Nitride

7.1 INTRODUCTION

As the aim of this work is to produce device-quality a-Si:H at a low thermal budget (<150 °C), it is important to be able to investigate the properties of this material in working devices. However, as there is no stated objective to produce a completely low-temperature TFT, it is not necessary here to investigate gate dielectrics with a comparable thermal budget. Therefore, in order for device characteristics to be assessed with reference only to the low-temperature active layer, the TFT gate dielectric should be a high-quality, standard material.

One of the most widely used insulating materials in microelectronic devices, and in particular in TFTs, is silicon nitride (SiN). The purpose of this chapter is to describe the experimental optimisation of the SiN material used in this work. The optimisation procedure for this systematic study was similar to that used for the deposition of the gas-heated a-Si:H detailed previously (§ 6). A set of standard conditions were chosen and the deposition parameters were varied individually around the standard values with the others kept constant, with the exception of the substrate temperature which was held at 300 °C. Any changes in film properties were investigated using the aforementioned characterisation techniques (§ 5).

7.2 PECVD SILICON NITRIDE

SiN is a very important material within the semiconductor industry, finding uses in solar-cell technology as an anti-reflection coating, and applied to other large-area and optoelectronic devices such as 2D imagers, scanners and detectors [232]. However, it is its use within display technologies, and specifically AMLCDs that is of primary

concern here. Indeed, as SiN is the preferred gate dielectric for a-Si:H TFTs on account of it giving better device performance than other insulating materials [233], almost all commercial AMLCDs use a combination of a-Si:H as the active channel layer and SiN as the gate insulator.

Whilst SiN can be prepared in a number of different ways including reactive sputtering, ion implantation, thermal nitridation of silicon and more recently ECR-PECVD, the methods most commonly used are LPCVD and PECVD. Although, the relatively high temperature of the LPCVD process (700-900 °C) precludes its use in display-based applications. The lower temperatures utilised in the PECVD process (<400 °C) hence make it the most commonly used deposition technique for SiN within this technology area. There are also obvious benefits (e.g. processing compatibility) to using the same growth method for both the gate dielectric and channel layers.

However, PECVD-grown SiN should not be considered to be the same as stoichiometric Si_3N_4 [234]. Due to the low temperatures used during deposition, the hydrogen-containing pre-cursor molecules are not completed decomposed. This results in relatively large concentrations of hydrogen (15-40 at.%) being incorporated into the films [234]. This is substantially higher than typical values found for stoichiometric Si_3N_4 grown by LPCVD (2-3 at%) [235). The exact nature and concentration of hydrogen incorporation is dependent on the specific details of the process parameters. And as with a-Si:H, the concentration decreases as the deposition temperature increases [236]. Moreover, different pre-cursor gas mixtures can significantly affect the resultant material properties.

SiN films deposited using a SiH_4 and N_2 gas mixture tend to be silicon-rich due to the large difference in the dissociation energies for silane (3.1eV) and nitrogen (9.9eV) molecules [237]. This disparity in reactivity can result in the film stoichiometry varying enormously with the plasma generating power and deposition pressure. However, it has been suggested that a SiH_4:N_2 process results in less hydrogen incorporation [238]. Indeed, nitride stoichiometry can be improved if the ratio of

SiH_4:N_2 is kept low or high power densities are used, but this leads to rather low deposition rates (0.05 - 0.2 nm s^{-1}) [239].

It has been shown that for high-quality SiN to be deposited by PECVD, it is necessary to produce aminosilane radicals (SiN_xH_y) in the plasma [240]. However, this is not achievable using a gas mixture of SiH_4 and N_2 because of the high stability of the N_2. As a result, it is thought that Si-N bonds are only formed in the film during the growth process rather than in the gas phase. Therefore, it is more common for highly reactive ammonia (NH_3) to be included in the growth process in an effort to produce the necessary aminosilane pre-cursors. These molecules adsorb on the film surface with a low sticking coefficient, which promotes the growth of a dense and compact film [241]. One possible reaction pathway leading to SiN deposition is ammonia abstraction [241].

$$3Si(NH_2)_4 \rightarrow Si_3N_4 + 8NH_3 \qquad (7.1)$$

This reaction can take place at the surface or in the sub-surface region of the growing film. NH_2 groups split-off from the Si atom and react with H from nearby N-H bonds, thereby forming NH_3, thus facilitating cross-linking between Si and N. The efficiency of this reaction is expected to depend on substrate temperature.

The reduction of the difference in the dissociation energies means that nitrides deposited using SiH_4:NH_3 gas mixtures have an improved stoichiometry as compared to those produced with N_2. The disadvantage of this methodology is that it can lead to an increase in the hydrogen incorporated into the deposited films. Hence, any subsequent loss of hydrogen can result in stability issues [242]. Yet, this problem can be addressed by increasing the NH_3:SiH_4 ratio to produce nitrogen-rich films. The majority of hydrogen (>90%) is then bonded to nitrogen atoms, thereby improving the film's stability.

By taking into account the relative advantages and disadvantages of the potential source-gases used for SiN deposition, a mixture of SiH_4, NH_3 and N_2 was chosen for the optimisation of the standard-temperature SiN used in this work. This combination

of gases is frequently used for the industrial production of device-quality PECVD SiN [243].

7.3 OPTIMISATION OF PECVD SILICON NITRIDE

As already stated, in order to investigate the effects of gas-heating on the properties of low-temperature a-Si:H, it was decided that the SiN used here would be grown at standard temperatures (300 °C). Therefore, this necessitated the use of a separate PECVD reactor, as the newly designed system was only capable of reaching 150 °C. Consequently, the chamber that was used was part of the Oxford Plasma Technology μP 80 system that controlled the processing for the low-temperature a-Si:H work.

The experimental arrangement between the two reactors was very similar. The main difference was that the upper electrode of the OPT reactor forms the top of the chamber, rather than being suspended from lengths of stainless steel studding (§ 4.4). The lower electrode was heated by a buried heater and formed a table on which substrates could be placed. This temperature was monitored by a type-K thermocouple connected to a microprocessor-based Honeywell Class 94 temperature controller, which can maintain the substrate temperature at any pre-set point between 25 °C and 400 °C to within ±1°C. Two pressure gauges were attached to the system; a Edwards Type 600 Barocel capacitance manometer used during depositions covered the pressure range 1-2000 mTorr and a Penning CP-25EK which was used to monitor the base pressure of the system. The chamber dimensions, gas delivery mechanisms, pump combination, RF generator connections and process control were identical to the low-temperature system. The deposition pressure was set manually via the microprocessor unit by adjusting the conductance of a throttle valve situated between the pumps and the chamber.

The set of base conditions used for SiN optimisation were derived after extensive reading of the literature and by the characterisation of several trial samples. These are detailed in Table 7.1 below.

Table 7.1 Base SiN Deposition Conditions

Deposition Variable	Condition
Temperature (°C)	300
Pressure (mTorr)	350
RF Power (W)	20
SiH_4 Flow Rate (sccm)	20
NH_3 Flow Rate (sccm)	40
N_2 Flow Rate (sccm)	100

The N_2 mass flow controller that was part of the gas-handling unit had a relatively low maximum flow rate (200 sccm). This placed some limitations on the extent to which this particular process parameter could be varied. Therefore, in an effort to investigate the effect of the different gas flow rates on the material properties of SiN, it was decided that the ratio of SiH_4:(NH3 + N2) would be studied in addition to the variation in SiH_4 flow rate. All deposited nitride samples were of approximately the same thickness (1000 Å) to reduce the effects of film thickness on the measured physical and electrical properties.

7.3.1 DEPOSITION RATE

The deposition rate of the SiN was affected by all of the process variables to a certain extent, and within the limits defined by the system. The increase in the deposition rate with increasing RF power and pressure can be attributed to an increase in the concentration of film-forming radicals as more gaseous-phase reactions take place. As these variables are increased further the deposition rate begins to level off, which can be explained in terms of saturation effects and more non-film forming gas-phase reactions occurring. The relationship between these two factors is illustrated below in Figure 7.1 (a). In addition, as the silane flow rate is increased, the deposition rate increases almost linearly as would be expected given the increase in supply of silane molecules into the reactor. (Figure 7.1(b)). Conversely, as the SiH_4 :(NH_3 + N_2) gas ratio increases the deposition rate can be seen to decrease. This is logical given the

diluting effect of N_2 gas in the PECVD deposition process of SiN and the possibility that the N_2 reaches the surface where it has an etching effect.

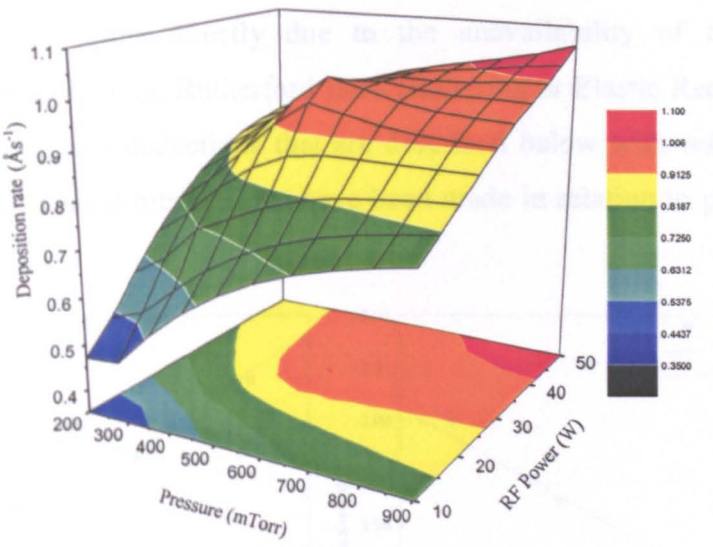

(a)

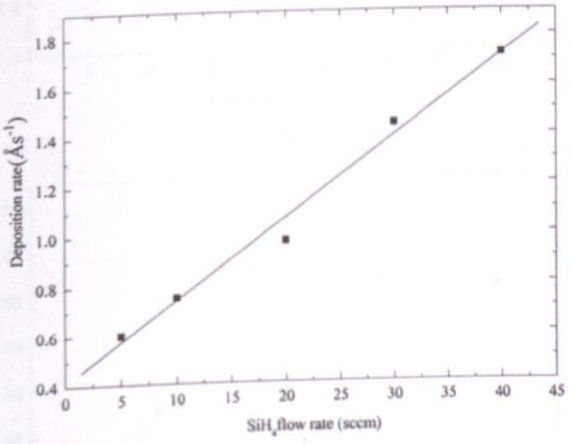

(b)

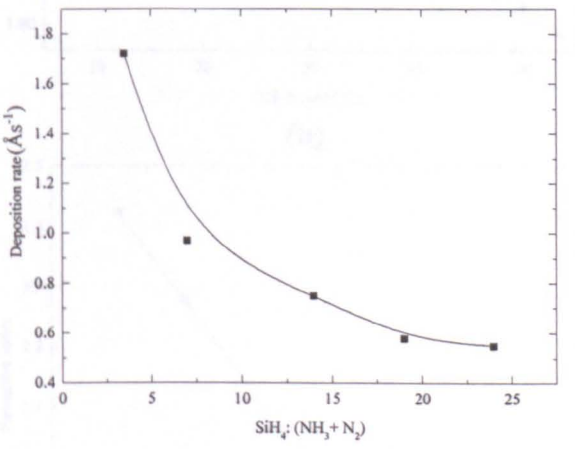

(c)

Figure 7.1 (a) - (c) The relationship between deposition rate and the process variables

7.3.2 PHYSICAL CHARACTERISATION

The physical properties of the PECVD SiN are determined by all of the deposition variables to varying degrees. Here, the physical characterisation procedure was based

upon complimentary refractive index (R.I.) and etch rate measurements (E.R). However, it is important to remember that when using R.I. as a determinant of film composition that it is possible for different material compositions to result in the same value for the R.I. [244]. In addition, I.R. spectroscopy was used to investigate impurity and hydrogen concentrations. It was not possible in this work to quantify the stoichiometry of the films directly due to the unavailability of the particular measurement techniques, (e.g. Rutherford Back Scattering or Elastic Recoil Detection Analysis). Therefore, any deductions that are described below with reference to the N:Si ratio of the deposited nitride films have been made in relation to previous work in the literature.

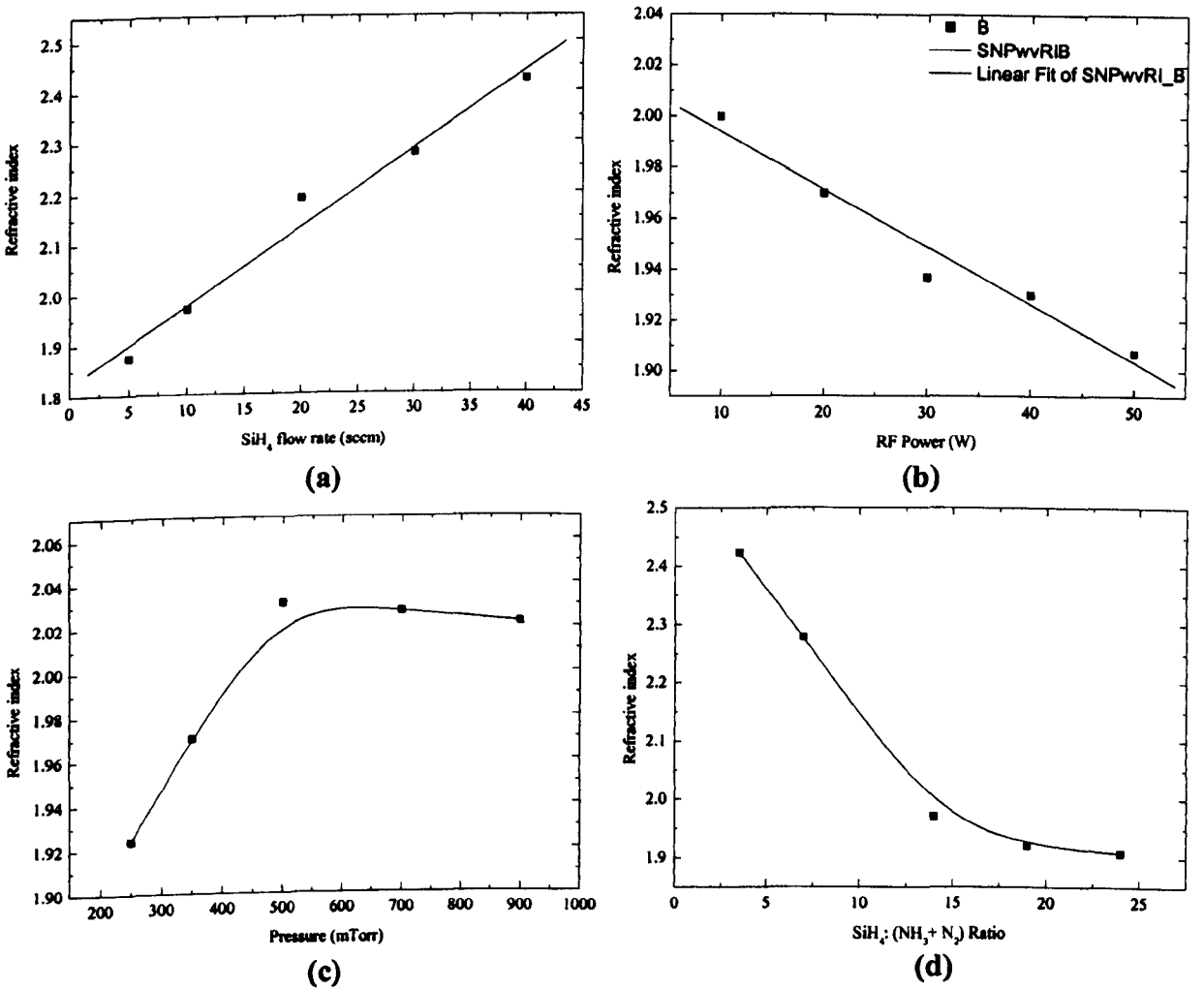

Figure 7.2 (a) – (d) The variation in Refractive Index with process variables

Figure 7.2 shows the effects of the process variables on the R.I. of the SiN layers. It can be seen that an increase in the SiH_4 flow rate is accompanied by an increase in the R.I. An R.I. value of below 1.97 can be an indication that the nitride is nitrogen-rich

[245]. This assumption is reasonable given the increase in supply of silane precursors at higher flow rates. Indeed, it has been reported that the R.I. varies linearly with a change in N:Si ratio, with R.I. increasing with a reduction in N:Si [246].

The decrease in the R.I. value with increasing RF power is probably due to an improvement in the stoichiometry as the ratio between N-containing radicals and silicon hydrides increases at higher power densities. In contrast, as the deposition pressure is increased, there is a rapid rise in R.I. to 2.02 at 500 mTorr, indicating that the nitride is becoming silicon rich. Thereafter, pressure has little effect within the limits of this study. Higher gas ratios result in the R.I. value decreasing from ~ 2.4 with a SiH_4:(NH_3 + N_2) ratio of 3.5, to ~ 1.9 at a ratio of 24. Given that the composition of the deposited films critically depends on the gas phase composition, this variation is understandable. This trend has also been observed elsewhere in PECVD processes utilising both SiH_4-NH_3 [246] and SiH_4-N_2 gas combinations [247].

To investigate these matters further, FTIR spectroscopy was utilised in an effort to corroborate changes in film composition to variations in the R.I. value. The IR spectra were also used to evaluate the hydrogen content (C_H) of the nitride films. No oxygen-related impurities were evident in the spectra and the only resonant modes present were the primary absorption peaks at ~ 840 cm^{-1} (Si-N), ~ 2100 $_{cm}$-1 (Si-H_x) and 3350 cm^{-1} (N-H).

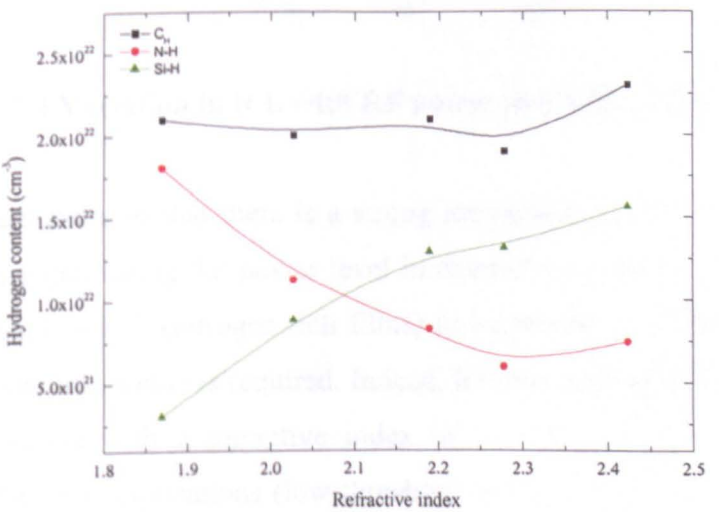

Figure 7.3 Correlation between concentration of Si-H and N-H bonds and R.I.

There was very little variation in the overall hydrogen content with changes in the deposition parameters, with C_H being of the order ~ 2.0 x 10^{22} cm^{-3}. However, there were definite changes in the concentrations of Si-H and N-H bonds as the R.I. increases, thus becoming more silicon-rich. Some combined results of the calculated C_H values and the measured R.I. are shown in Figure 7.3 above. These changes are evident as the concentration of N-H bonds is higher than Si-H bonds at low R.I. values, and vice versa.

Overall, the parameters that have the greatest effect on the R.I are the RF power value and the ratio of SiH_4 to NH_3 and N_2. The interaction between these two parameters and their combined effect on the R.I can be seen in Figure 7.4.

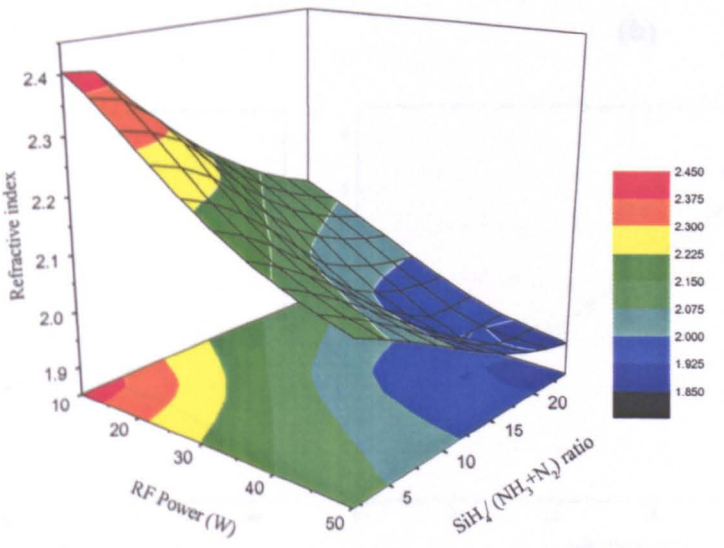

Figure 7.4 Variation in R.I. with RF power and SiH_4: (NH_3 + N_2) ratio

Figure 7.4 demonstrates that there is a strong interaction between the gas flow ratio and the plasma generating RF power level in determining the R.I. of the SiN layers. For SiN with a low R.I. (nitrogen-rich films) to be produced, a relatively high SiH_4: (NH_3 + N_2) ratio and power is required. Indeed, it is has been described elsewhere that it is nitride layers with a refractive index of ~ 1.90 that prove to be the most appropriate for TFT applications (low threshold voltage, increased resistivity) [248]. However, as previously described, R.I. on its own should not be taken as a indication of stoichiometry for a dielectric layer. Therefore, investigations of the E.R. of the

deposited nitrides were also undertaken in an effort to understand if improvements in film stoichiometry were actually occurring or variations in R.I were a consequence of changes in film density. The variation in E.R. of the SIN films with the process parameters can be seen in Figure 7.5.

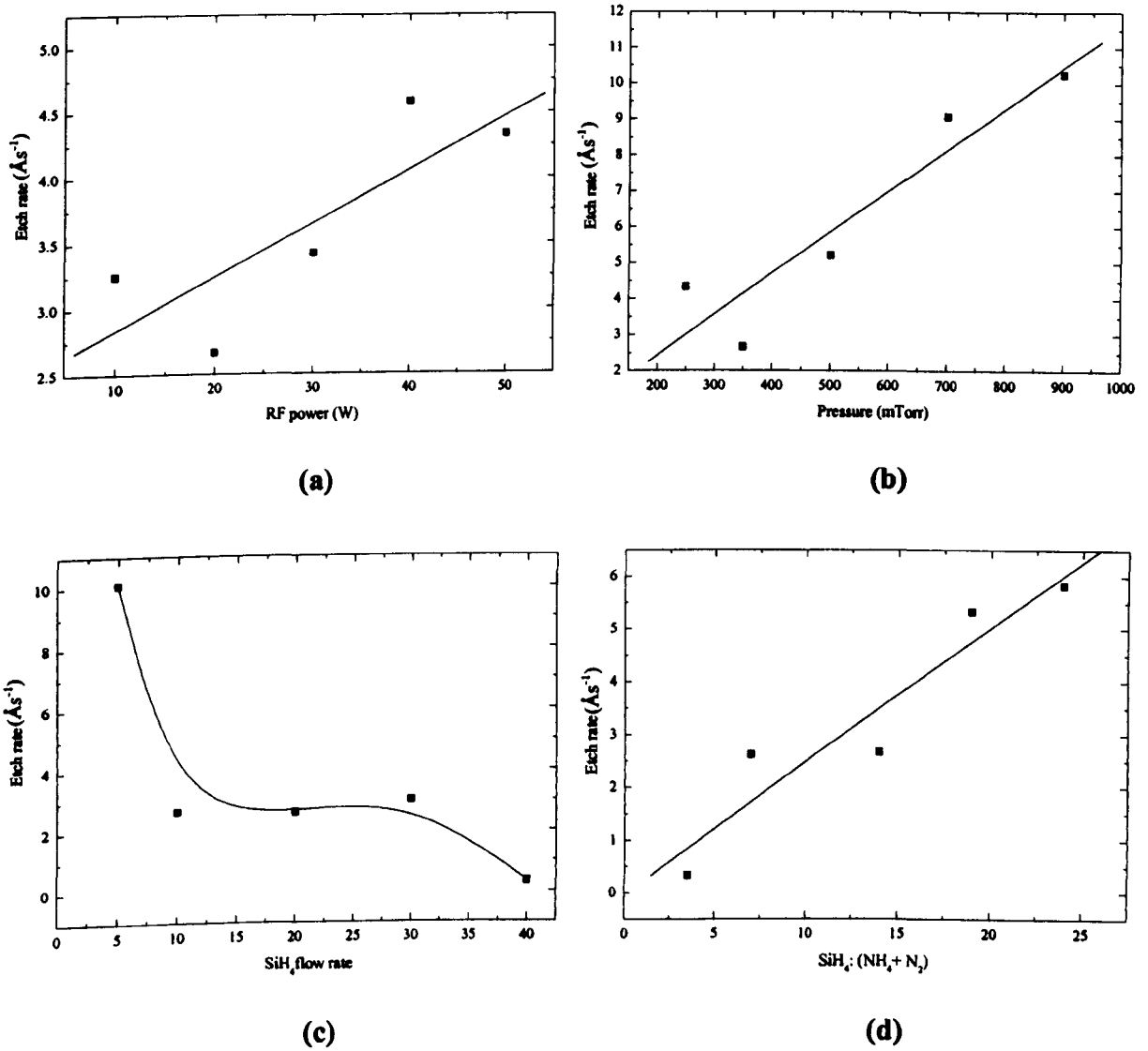

Figure 7.5 (a) – (d) The variation in Etch Rate with process variables

The relatively rapid increase in the E.R. with increasing pressure can be partly attributed to increased deposition rates which lead to greater porosity of the deposited layers. An increase in E. R. can also be observed at higher power densities, although this increase is much less marked (< 2 $Å s^{-1}$ over the range of powers used). However, the results can also be explained by considering changes to the plasma species during

deposition. At higher pressures, the mean free path of all of the gaseous species is reduced, promoting more gas phase reactions. Consequently, this leads to a higher rate of aminosilane production and hence more nitrogen incorporation. As a result, there is a deficiency of silicon atoms in the amorphous network and hence a less dense film. Higher powers lead to more dissociation of the ammonia molecules resulting in a similar increase in aminosilane production. The decrease in the E.R. with increasing SiH_4 flow rate is a result of an increase in the concentration of Si atoms in the growing film, and correlates well with the concurrent increase in the R.I. at high concentrations of SiH_4 molecules in the gas phase.

After an initial dramatic reduction in the E.R. as the SiH_4 flow increases from 5 sccm to 10 sccm, there is little change until a flow rate of 40 sccm is used, at which point the E.R. is very low, indicating an increase in the density of the film. Conversely, an increase in the SiH_4: (NH_3+N_2) ratio results in an increase in the E.R. This can again be attributed to an increase in the concentration of N atoms (and N-H bonds) in the SiN layers.

When considering the E.R. data in conjunction with changes in the R.I, it is evident that there is a high degree of interdependency between the process variables. Therefore, in order to fully optimise the physical properties of the deposited SiN films, it is necessary to carefully balance the deposition conditions. The results suggest that a median value for the SiH_4 : (NH_3+N_2) ratio is needed to optimise the physical properties. Increasing the gas ratio improves the film stoichiometry but reduces the film density. However at high gas ratios ($> \sim 1:20$) the SiN layers become increasingly porous with an etch rate of ~ 10 $Å s^{-1}$. In addition, the deposition pressure must be kept relatively low (350 mTorr) and a system power of >20W must be utilised in order to produce dense films with acceptable stoichiometry.

7.3.3 BULK ELECTRICAL CHARACTERISATION

The bulk electrical properties of the SiN are determined by most of the deposition parameters to varying degrees. However, they show little dependence on the chamber pressure. The relationship between the deposition variables and film resistivity is shown in Figure 7.6 (a) – (c). Each of the data points shown are mean values

calculated from a minimum of 10 separate measurements of MIS structures on each SiN sample.

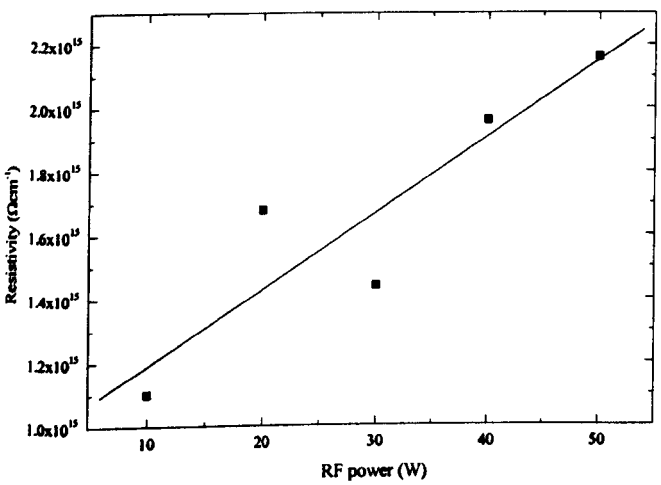

(a)

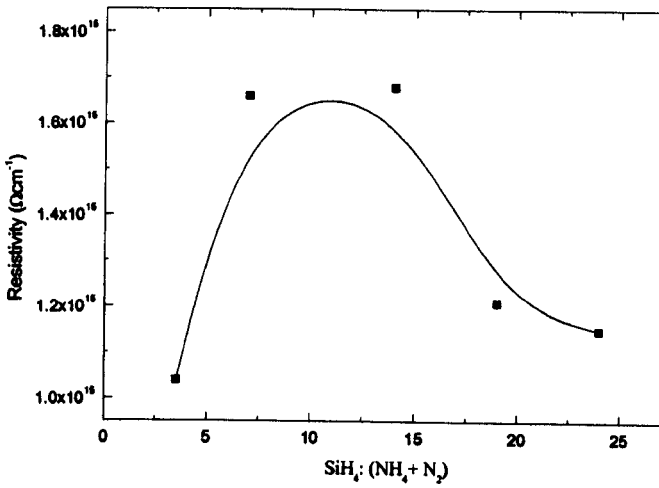

(b)

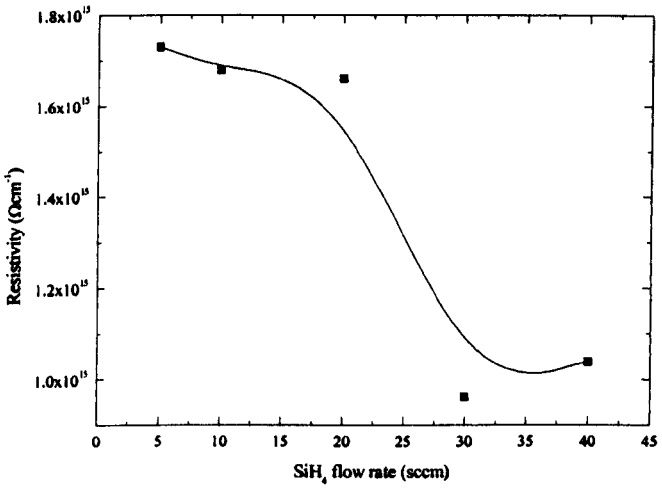

(c)

Figure 7.6 (a) – (c) The variation in Resistivity with process variables

As the system power is increased, there is a concurrent increase in resistivity up to a maximum of 2.16 x 10^{15} Ωcm, as the film stoichiometry improves in conjunction with a slight increase in film porosity. The relationship between the resistivity and the SiH_4: (NH_3+N_2) ratio is more complicated as after an initial rise, there is a subsequent reduction in resistivity as the concentration of (NH_3 + N_2) within the reactor increases. At high flow rates of (NH_3 + N_2), and hence high ratios of (NH_3 + N_2) to

SiH_4, the E.R. results detailed above indicate that these films are highly porous with an increased dangling-bond density, which would explain the sudden reduction in resistivity. Similarly, as the SiH_4 flow rate increases, the resistivity reduces significantly as the concentration of Si atoms in the amorphous matrix increases. In order to obtain TFTs with a high stability and high mobility, it is imperative that there is a low density of localised states in the band gap of SiN. Silicon dangling bonds are a major source of trapping centres in both stoichiometric and N-rich SiN, and are thought to be located close to midgap [249][250]. In addition, weak Si-Si bonds can also be found in SiN, with their associated electronic states located in the broad valence band-tail where they act as hole-trapping and multiple-trapping transport centres [251].

The dielectric strength of the PECVD SiN was largely independent of all of the process variables, with breakdown only occurring at electric fields in excess of 10 $MVcm^{-1}$. An applied electric field of approximately 1 $MVcm^{-1}$ across the gate insulator is typically used for TFTs in AMLCDs, which is well within the capability of the SiN thin films produced here.

In summary, optimisation of the bulk electrical properties requires a high power (50W), a relatively low SiH_4 flow rate (10 sccm) but only a median SiH_4: (NH_3+N_2) ratio (1:14).

7.3.4 INTERFACIAL CHARACTERISATION

The interfacial properties of the MIS test structures depend critically on the cleanliness and surface preparation of the substrate surface. In an effort to address this issue, all substrates were prepared in a clean room environment in a manner described in Appendix B. Within the explored ranges of the process variables, the interfacial properties are essentially independent of the deposition conditions. Using the high-frequency C-V technique detailed earlier (§ 5.3.3), typical fixed charge and interface trap densities are $4x10^{12}$ cm^{-2} and 10^{11} $cm^{-2}eV^{-1}$ respectively, with an average hysteresis in the C-V curve of 2 V. This hysteresis can be attributed to hole trapping in the SiN layer.

7.3.5 PROPERTIES OF OPTMISED PECVD SILICON NITRIDE

When optimising a material a careful balance has to be struck between all of the deposition variables. Consequently, both the electrical and the physical characteristics have to be considered in conjunction, so that undue emphasis isn't placed upon the moderate effect of one particular variable on a specific material property. Therefore, an optimal SiN layer must be both dense and have a low refractive index (~1.90), whilst also being highly resistive. Thus, by using the results and discussions detailed above, it is possible to produce an optimised SiN material whose physical and electrical properties are described in Table 7.2.

Table 7.2 Typical Properties of the Optimised PECVD Silicon Nitride

Film Property	SiN
Deposition rate ($Å s^{-1}$)	0.79
Etch rate – Buff. HF ($Å s^{-1}$)	4.3
Hydrogen Content (at%)	22
Refractive Index	1.90
Dielectric Strength ($MV cm^{-1}$)	10
Resistivity (Ωcm)	10^{15}
Fixed Charge Density (cm^{-2})	$4x10^{12}$
Interface State Density ($cm^{-2}eV^{-1}$)	10^{11}
C-V Hysteresis (V)	2

These results suggest that a low SiH_4 flow rate, a median SiH_4: (NH_3+N_2) ratio and a relatively high power together with a low pressure fulfil the above criteria for the deposition of high quality SiN at 300 °C. The optimised SiN deposition conditions are shown in Table 7.3.

Table 7.3 Optimised Silicon Nitride Deposition Conditions

Deposition Variable	Condition
Temperature (°C)	300
Pressure (mTorr)	350
RF Power (W)	50
SiH_4 Flow Rate (sccm)	10
NH_3 Flow Rate (sccm)	40
N_2 Flow Rate (sccm)	100

Although it was not an aim of this work to optimise SiN material at low temperatures (<150 °C), in order to understand fully the nature and characteristics of the low temperature, gas-heated a-Si:H, it was vital that a high-quality gate insulator could be readily produced. The excellent physical and electrical properties of the PECVD SiN detailed above demonstrate that it is suitable for incorporation into TFTs using the optimised gas-heated a-Si:H described earlier, thus enabling further investigation of the low temperature material to take place.

However, it would be instructive to briefly discuss the possibility of the production of a completely low thermal budget TFT. The problems associated with reducing the growth temperature for the deposition of a-Si:H have already been discussed in some detail previously (§ 4.4; 6) and can also reasonably be applied to the production of n^+ a-Si:H. But the effect of a low thermal budget on the quality of the gate dielectric is of equal importance. This discussion will be restricted to problems associated with the low temperature deposition of SiN for reasons previously outlined concerning its suitability for a-Si:H TFT operation (§ 7.2).

7.4 TOWARDS COMPLETE TFTs PRODUCED AT A LOW THERMAL BUDGET

It has been stated above that a combination of SiH_4, NH_3 and N_2 gases is preferable when depositing SiN by PECVD (§ 7.2). However, if it is grown in this way using low substrate temperatures (<150 °C), the resultant film can be very hydrogen rich

and consequently can have poor electrical properties [252}. As with a-Si:H, the low temperature reduces the mobility of the deposition species on the growing film surface, thus preventing them from finding their optimal bonding site. Therefore, it is necessary to heat the substrate to over 250 °C in order for this excess hydrogen to be removed.

A further problem associated with low temperature deposition of SiN is the increase in porosity of the material. This can lead to such films easily oxidising even at room temperature [253]. This oxidation stems from the formation of Si-O bonds resulting from the percolation of ambient moisture and oxygen into the porous film, followed by the conversion of Si-N bonds into the chemically more stable Si-O bonds [254]. Indeed, a porous SiN film can be completely converted to silicon oxide over a period of time [255].

Therefore, the challenge is to create a deposition environment where the more stable bonds are able to form and where the hydrogen content can be maintained at an acceptable level. This essentially means providing sufficient energy to the adsorbed species in the growing film whilst simultaneously preventing the creation of defects.

An appreciable amount of work has been undertaken recently to reduce the temperature of deposition of SiN whilst maintaining material density [see 13-21 in 255]. And particular emphasis has been placed on the use of energetic ion bombardment during deposition to compensate for the reduction in direct thermal energy applied to the substrate. This has been achieved using either low frequency or radio-frequency biasing of the substrate electrode during deposition, or modified CVD techniques such as ECR-PECVD.

Some encouraging results using these techniques have been achieved. Both the density and deposition rate of SiN has been shown to increase with the use of ion bombardment [255]; electrical properties comparable to higher temperature layers have also been demonstrated [115]. However problems still exist such as the feasibility of transferring some methods into a production environment. Despite this, improvements in process techniques, the utilisation of novel chemistry, as well as

increasing understanding of the deposition processes of both active and insulating layers, all contribute to the possible future production of industrially-viable, low temperature TFTs for large area electronic applications.

Chapter 8

The performance of TFTs using low temperature PECVD a-Si:H

8.1 INTRODUCTION

Whilst some results described previously are encouraging, they do not establish that a-Si:H deposited with gas heating at low temperature can be used successfully in device applications. In this chapter, the performance of TFTs incorporating active and doped layers of a-Si:H deposited by PECVD with source gas heating is described.

The fabrication process used for all devices is detailed in Appendix C, and the maximum processing temperature for the a-Si:H layers was 125 °C as determined by the hard bake temperature of the positive photoresist used in the photolithographic procedure. All devices discussed in this chapter have a W/L ratio of 125 and a gate insulator thickness of 300 nm. The relative permittivity of the optimised PECVD silicon nitride (SiN) layer deposited at 300 °C is assumed to be 6.4, following previous work [227]. The effect of processing on these materials has not been investigated.

8.2 GAS HEATED A-Si:H TFT CHARACTERISTICS (GH-TFTs)

All measurements of device characteristics were made at 40 °C (313 K) as described in § 5.3.2. All the data in this chapter pertains to devices with the same gate insulator material (SiN) and W/L ratio, so the characteristics need not be normalised; only plots detailing the raw current-voltage data are shown.

8.2.1 TRANSFER CHARACTERISTICS

A typical linear gate transfer characteristic for a TFT incorporating gas-heated active

and doped layers of a-Si:H is shown in Figure 8.1. The switching action of the transistor can be clearly seen with this device exhibiting an OFF current of ~ 10^{-12} A and a switching ratio of approximately 10^5.

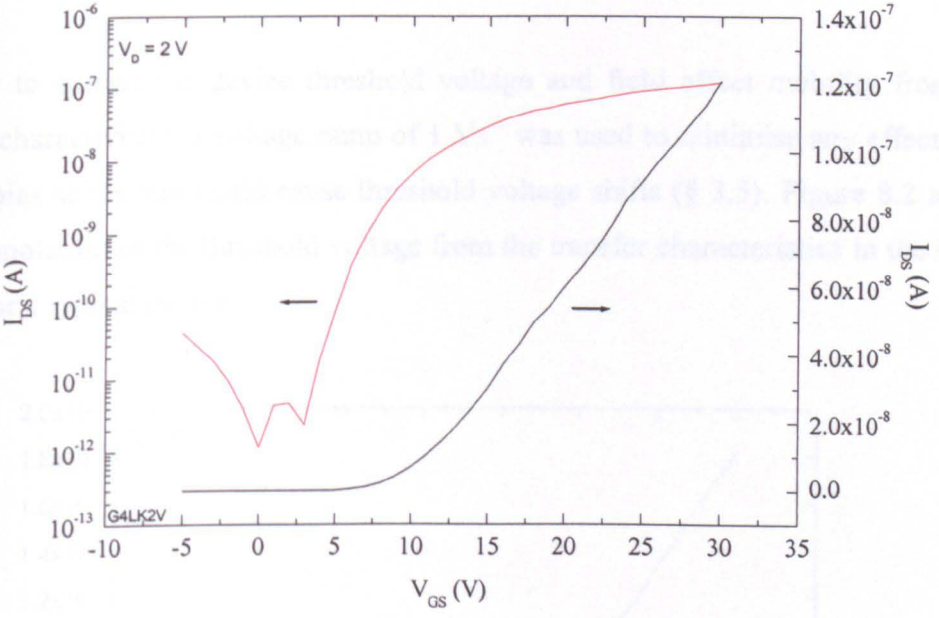

Figure 8.1 Transfer characteristic of TFT using gas heated active and doped layers of a-Si:H

These values are comparable to a-Si:H TFTs fabricated at higher temperatures, however, the switching ratio is around an order of magnitude smaller.

The switching speed of a TFT is quantified in terms of the inverse slope of the steepest portion of the semi-logarithmic transfer characteristic (S), and is described by,

$$S = \frac{dV_{GS}}{d\log(I_{DS})} \tag{8.1}$$

S is therefore an indication of the density of states in the upper half of the bandgap, (i.e. between mid-gap and the conduction band mobility edge), as all the states in this energy range must be filled prior to the TFT turning on (§ 3.4.1). Consequently, S

increases as the number of defects in the upper part of the bandgap increases, and TFT 'switch on' occurs over a larger voltage range. In these devices, S is typically 1.3 ± 0.4 Vdecade^{-1}, suggesting that the density of effects in the upper part of the bandgap of the a-Si:H. may be tolerable.

In order to extract the device threshold voltage and field effect mobility from the transfer characteristic, a voltage ramp of 1 Vs^{-1} was used to minimise any effects due to gate bias stress that could cause threshold voltage shifts (§ 3.5). Figure 8.2 shows the extrapolation of the threshold voltage from the transfer characteristics in the linear region for a typical device.

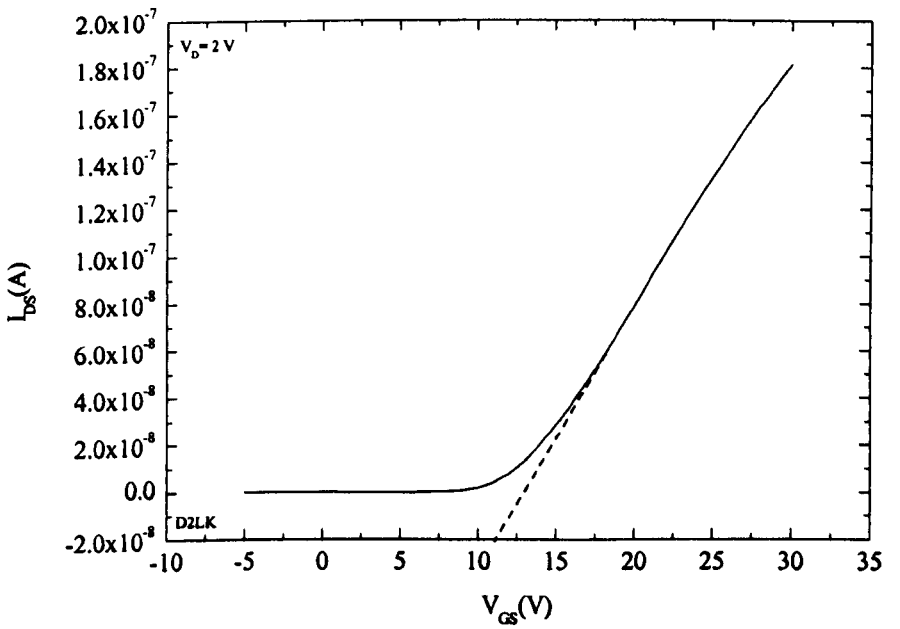

Figure 8.2 Extrapolation of the threshold voltage for a typical device

Here the threshold voltage is 11.1 V and the linear mobility is found to be 3.4 x 10^{-3} cm^{2}V^{-1}s^{-1}. Both the values for threshold voltage and the field effect mobility for this device are appreciably inferior to those of standard TFTs, being higher and much lower respectively. The mobility depends primarily on the density of localised conduction band tail states (§ 3.4.1); therefore, the concentration of tail states in that region must be relatively high. This correlates well with data described previously relating to the level of disorder in this material (§ 6.5).

The mobility of an a-Si:H TFT is thermally activated with an activation energy which is dependent on the width of the conduction band tail (§ 3.4.1). Therefore, a series of gate transfer characteristics were measured at different temperatures and the mobilities extracted. The results are shown in Figure 8.3.

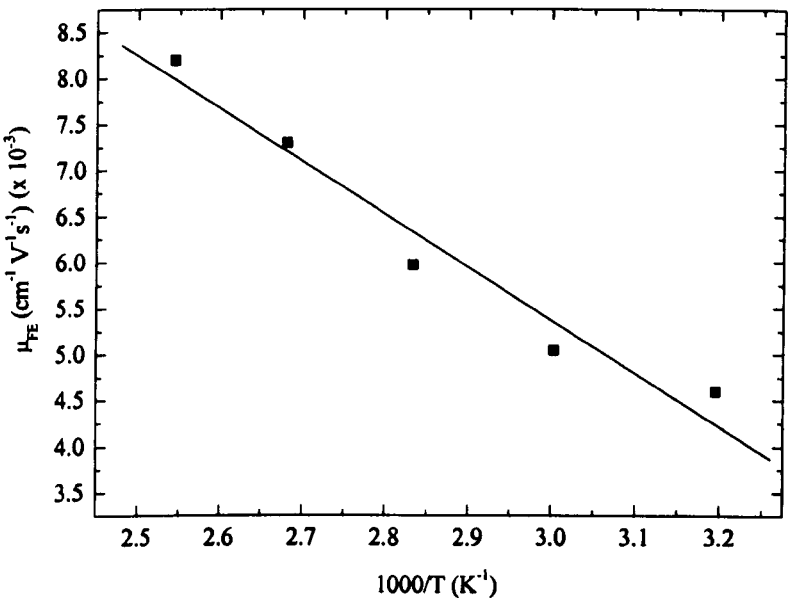

Figure 8.3 Thermal activation of the field effect mobility

The mobility shows an Arrhenius dependence with temperature, and in this case, an activation energy of mobility of 0.096 ±0.005 eV.

8.2.2 OUTPUT CHARACTERISTICS

Figure 8.4 shows a series of output characteristics for a gas-heated a-Si:H TFT. An important observation is the absence of current crowding at low drain voltages.

The good n-channel saturation and ohmicity, common to all fabricated devices, demonstrates the thermal stability of the Al/n^+a-Si:H/i-a-Si:H contact scheme (§ 3.6). In addition, these results also strongly suggest that the dopant activation in the low-temperature doped a-Si:H deposited by gas heating is adequate to facilitate device operation.

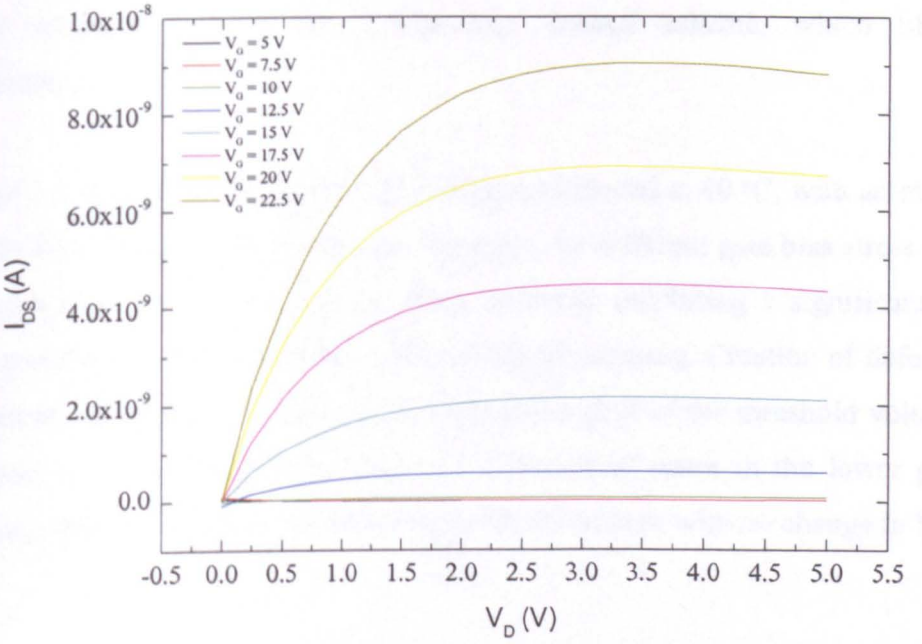

Figure 8.4 Output characteristics for a typical gas heated a-Si:H TFT

8.2.3 GAS HEATED A-Si:H TFT STABILITY

Device stability was investigated as described in § 5.3.5. The standard method used to identify the different instability mechanisms in a-Si:H TFTs involves experiments with ambipolar TFTs [93]. An ambipolar TFT is one which shows both electron and hold accumulation layers, under positive and negative gate voltage respectively.

Alternatively, separate n-channel and p-channel devices can be fabricated. P-channel transistors can be manufactured either by depositing aluminium directly onto the intrinsic a-Si:H layer, followed by a low temperature anneal, or doping an intermediate contact layer p-type. The latter method was not feasible as there was no way to deposit p-type material in the EMTERC laboratory. Aluminium diffuses into the top of the undoped layer, doping it p-type. However, the annealing temperature (~ >150 °C) is higher than the deposition temperature of the optimised a-Si:H. Therefore, as this would change the properties of the deposited material, and as TFT stability was not a particular focus of this work, experiments involving p-channel devices were not carried out. Consequently, it was not possible to differentiate between state creation in

the a-Si:H and charge trapping in the gate dielectric (§ 3.5) because of the n^+ a-Si:H layer incorporated into the source-drain contact scheme, which blocks hole conduction.

Figure 8.5 shows gate transfer characteristics measured at 40 °C, with an electric field of 1 $MVcm^{-1}$ applied across the gate insulator, for different gate bias stress times. The results show that the devices are rather unstable, exhibiting a significant threshold voltage shift even for relatively short periods of stressing. Creation of defect states in the upper part of the bandgap leads to a positive shift of the threshold voltage and an increase in the sub-threshold slope (S). Creation of states in the lower part of the bandgap leads to a positive shift in the threshold voltage with no change in S.

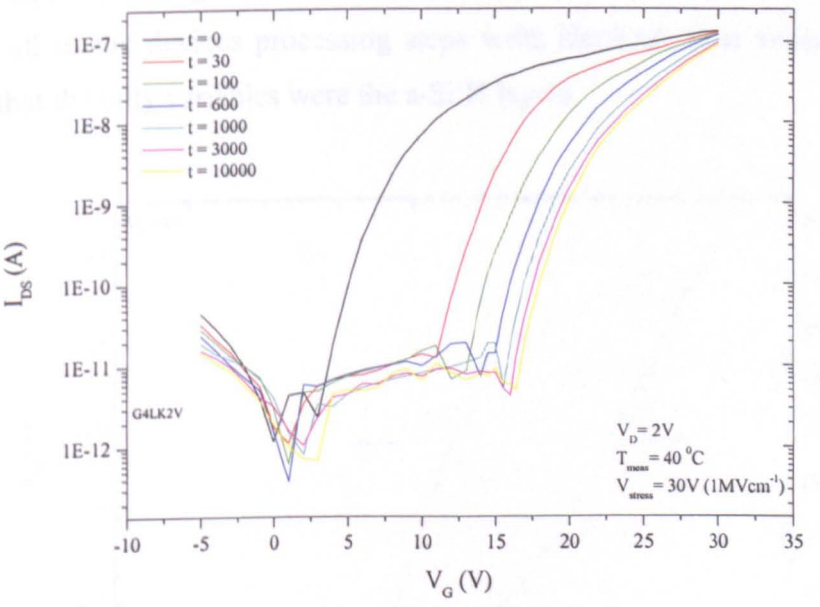

Figure 8.5 The shift in the gate transfer characteristics with gate bias stress time

As is evident from Figure 8.5, the value of S does not change significantly after bias stressing. This suggests that the newly created states must be located in the lower part of the bandgap. This is consistent with the idea that the created states are Si dangling bonds, which are formed by the breaking of weak Si-Si bonds [60]. The substantial shift in the threshold voltage even for short stressing times indicates that there is a considerable density of strained or weak Si-Si bonds in the gas-heated material.

In an effort to better understand and establish the effect of source gas heating on the properties of a-Si:H, a batch of TFTs were fabricated incorporating channel and doped a-Si:H layers deposited using the optimised base conditions detailed earlier (§ Table 6.1), but without gas heating. The insulating material was the same high-temperature silicon nitride (300 °C) that was used for the GH-TFTs, thus keeping the number of possible variables to a minimum. The results of these experiments can be found in the following section.

8.3 COMPARISON WITH ROOM TEMPERATURE A-Si:H TFTs (RT-TFTs)

Figure 8.6 shows a typical gate transfer characteristic for an a-Si:H TFT fabricated without gas heating of the active or doped layers. The gate insulator material was SiN and was deposited using the same recipe as was used for the gas-heated devices. In addition, all of the devices processing steps were identical, thus ensuring as far as possible that the only variables were the a-Si:H layers.

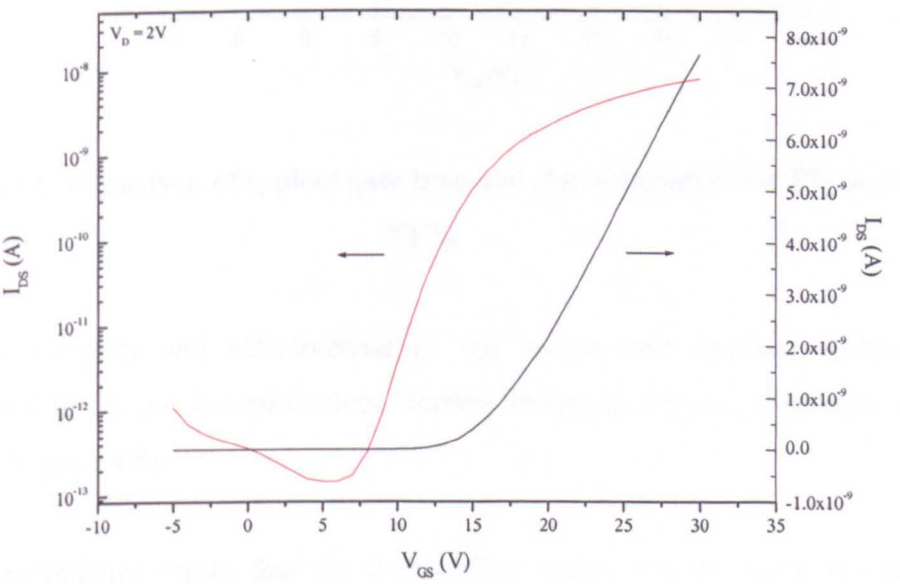

Figure 8.6 A typical gate transfer characteristic for an a-Si:H TFT using unheated active and doped layers of a-Si:H

Devices fabricated without gas heated a-Si:H layers exhibit inferior characteristics, which given the inferior properties of the room-temperature material might be

expected. Indeed, they are significantly worse than those of the gas heated devices, with this device having a mobility of 2.3 x 10^{-4} cm^2 $V^{-1}s^{-1}$ and a threshold voltage of 16 V. In order to compare the performance of both RT and GH-TFTs more clearly, typical gate transfer characteristics for the two sets of devices are shown in Figure 8.7. The increase in threshold voltage and reduction in on-current can be clearly seen.

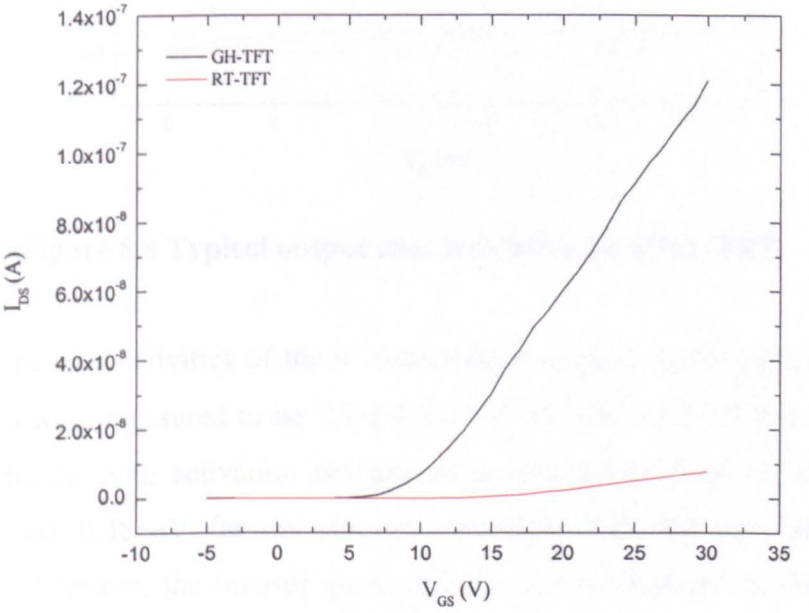

Figure 8.7 Comparison of typical gate transfer characteristics for RT and GH-TFTs

Whilst the integrity and effectiveness of the source-drain contact scheme was demonstrated in the gas-heated devices, current crowding effects are evident for the RT- TFTs (Figure 8.8).

These characteristics imply that the bulk defect density of the room temperature intrinsic a-Si:H is sufficiently high to prevent effective carrier injection from the doped layer. With an increase in the density of defect states in the bandgap, there is a concurrent increase in the effective resistance of the bulk intrinsic layer, which results in a higher trapping probability (§ 3.6). As a result, current crowding can occur in the device, quite independently of the ohmic source-drain contacts. The fact that the ohmicity of this contact scheme has been demonstrated suggests that a high bulk defect density could be the cause of the poor properties.

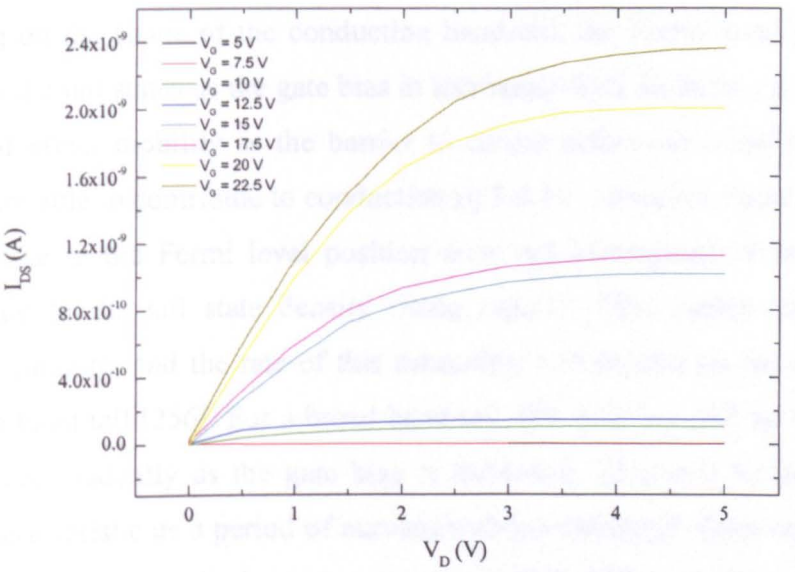

Figure 8.8 Typical output characteristics for a RT-TFT

In addition, the conductivities of the n^+ source-drain contact layers for both the GH and RT-TFTs were measured to be $7.1 \pm 0.5 \times 10^{-5}\ \Omega^{-1}cm^{-1}$ and $5.7 \pm 0.5 \times 10^{-5}\ \Omega^{-1}cm^{-1}$ respectively, with activation energies of conduction of 0.44 eV for the gas-heated film and 0.48 eV for the material deposited with the gas line at room temperature. Therefore, the inferior quality of the contact material in the RT-TFTs will also contribute to poor device performance.

An alternative explanation could be a high interface state density between the a-Si:H layer deposited without gas heating, and the high temperature SiN gate insulator. The performance of a TFT is highly dependent on the quality of the silicon/insulator interface, as the conducting channel is in close proximity to this interface. Therefore, the density of localised states in this region can have a substantial effect on the device properties.

It was demonstrated earlier that the level of disorder in the a-Si:H deposited in this work decreases as the temperature of the source gas line increases (§ 6.5). Therefore, it is possible that variations in the bonding configuration could play a part in defining the shape of the conduction band-tail in the interfacial region, and hence can directly affect the mobility of the carriers. By studying the transfer characteristics just above threshold, it is possible to gather more information about the distribution of the tail states.

Depending on the shape of the conduction band-tail, the Fermi level can be moved higher into the tail states as the gate bias in increased. This leads to a gradual increase in the field effect mobility as the barrier to carrier activation is reduced and more electrons are able to contribute to conduction (§ 3.4.1). However, there comes a point when the rise in the Fermi level position does not correspond to the rise in gate voltage, due to the tail state density rising rapidly. This causes the mobility to effectively saturate, and the rate of this saturation will depend on the breadth of the conduction band tail [256]. For a broad band-tail, the mobility will be lower and will saturate more gradually as the gate bias is increased. This will be manifest in the transfer characteristic as a period of curvature above threshold. Conversely, a narrow conduction band-tail results in an increased rate of mobility saturation and minimal curvature in the characteristic. Figure 8.9 shows abbreviated transfer characteristics for typical GH a-Si:H and RT a-Si:H TFTs.

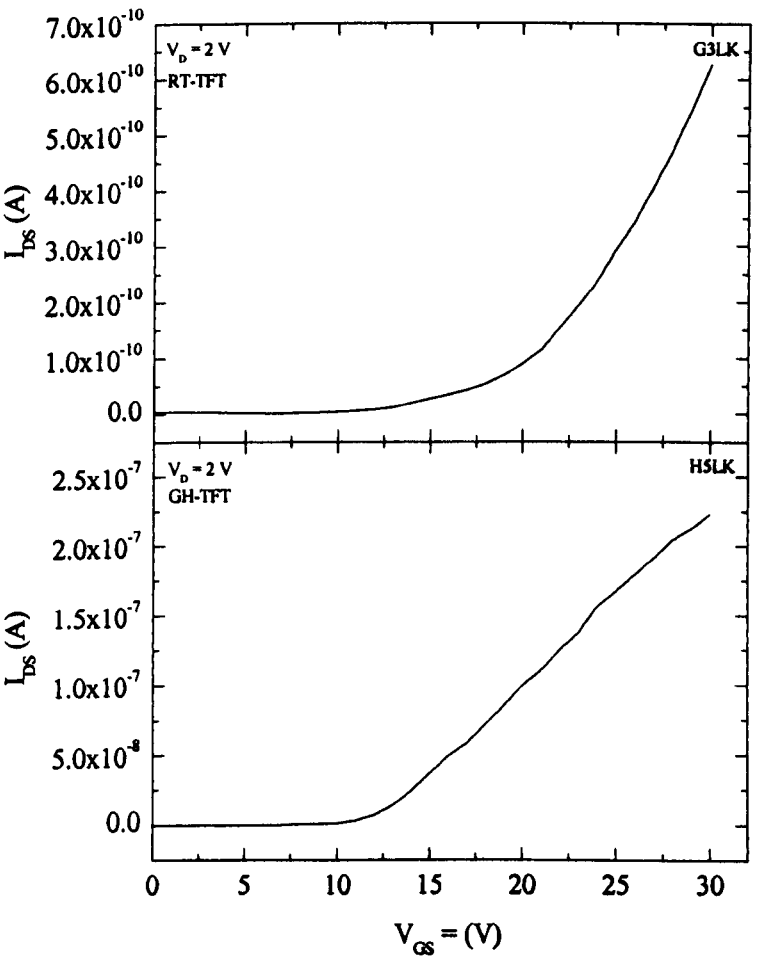

Figure 8.9 Transfer characteristics for GH-TFTs and RT-TFTs in the threshold region

The curvature of the transfer characteristic of the RT-TFT is significantly broader, i.e. it extends over a greater bias range, than that of the GH-TFT. This suggests that the a-Si:H film deposited without gas heating is more disordered than the gas heated film. In fact, the activation energy of mobility for the above device is 0.107 eV signifying a broader conduction band tail width, which is consistent with the theory proposed here.

To investigate the gate bias dependence of the field effect mobility in more detail, the gradient of the linear transfer characteristic was calculated at various gate biases above the device threshold voltage. The gradient was obtained by fitting a straight line through the experimental data over a 2 V sampling region which was then shifted along the transfer characteristic. The mobility was then calculated as before. Figure 8.10 shows the variations in mobility with increasing gate bias above threshold for typical RT-TFTs and GH-TFTs.

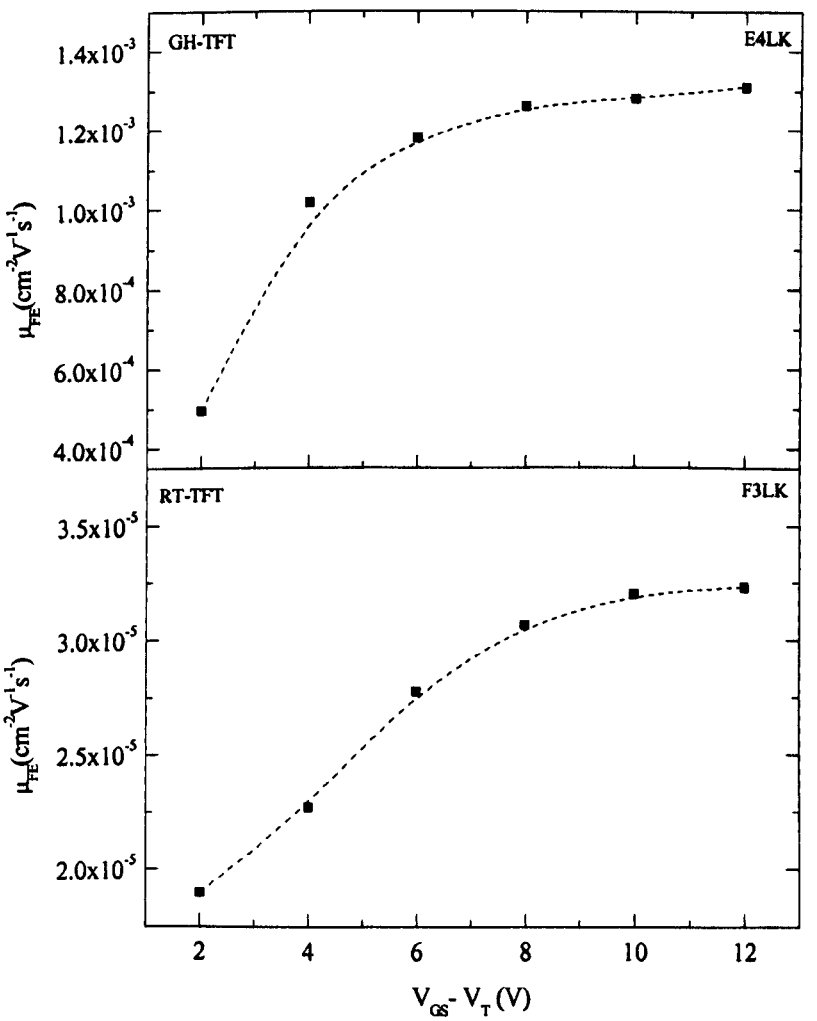

Figure 8.10 Variation in field effect mobility with above threshold gate bias

The more rapid saturation of the mobility for the GH-TFT correlates well with the reduced curvature of the transfer characteristics above threshold shown in Figure 8.8. This supports the view of a narrower conduction band-tail in the gas-heated a-Si:H layer. For an in-depth discussion on stability issues in a-Si:H TFTs see [256].

The SiN and a-Si:H layers were deposited in different chambers (§ 3.8), and therefore, as the EMTERC systems are not part of a multi-chamber assembly, there was some unavoidable exposure to air between the insulator and a-Si:H depositions. This was the case for devices fabricated both with and without heating of the source gases. Hence, any problems associated with airborne contaminants affecting the insulator surface should affect both sets of devices. However, it is possible that there are disparities between the insulator surfaces. Therefore, as surface effects due to gas adsorption depend on the surface nature, it would be difficult to state with any certainty that atmospheric contamination is a cause of the inferior properties of the RT-TFTs.

There is also the possibility that exposure of the SiN layer to high energy ions at the start of the a-Si:H deposition, could increase the concentration of interface trapping states due to plasma damage of the surface. However, the plasma parameters (RF power, chamber pressure, gas flows) were the same in both cases, so the energy of the impinging ions should be similar. One method of investigating the possibility of lattice mismatch and any resultant effects would be to use a different gate insulator instead of the SiN. If the poor characteristics of the TFTs are a consequence of material incompatibility, then a significant change in the transfer characteristics could be expected. It was the intention of the author to carry out these studies, but fundamental equipment failure prevented this work from taking place in the timeframe available. This should be a priority in future work.

Chapter 9

Conclusions and Future Work

This chapter summarises the major outcomes of this thesis, and some suggestions for future work are proposed.

9.1 CONTRIBUTIONS

The main objectives of this work were to design and build a PECVD system that included the facility of source gas pre-heating, and to improve the quality of a-Si:H films at temperatures compatible with low cost, plastic substrates.

Optimised a-Si:H films deposited at 125 °C with source gas heating (gas line = 400 °C) have been successfully incorporated into inverted staggered TFTs, with a high temperature (300 °C) SiN layer as the gate insulator. N^+a-Si:H material was deposited at the same substrate and gas line temperatures as the intrinsic film. Adequate dopant activation of the n^+ layer, and the ohmicity of the Al/n^+a-Si:H/a-Si:H source-drain contact scheme has been demonstrated.

In response to the work in this thesis, the system has recently been modified to include a facility to control the ion bombardment energy during the deposition process. This is done through the application of a low power, low frequency RF electric field to the substrate. Consequently, source gas heating can now be used in conjunction with the dual-RF system to facilitate further work on the manufacture of a-Si:H at substrate temperatures compatible with plastic substrates.

9.2 CONCLUSIONS

Despite severe technical problems, a novel, low temperature deposition system has been effectively demonstrated, and thin films of a-Si:H have been successfully manufactured in the new reactor by the PECVD technique. The physical properties of

these layers have been characterised by FTIR, UV/VIS spectroscopy and surface profilometry. Electrical measurements (I-V) were carried out using a Labview controlled environment and an HP 4140B picoammeter/voltage source.

Some of the key physical properties of the a-Si:H films deposited at low temperatures (<150 °C) with source gas heating bear favourable comparison with material deposited at higher, more typical temperatures (~ 250-300 °C).

Increased thermal energy in the gas mixture enhances the diffusion of the film forming SiH_3 radical on the growing film surface. This improves the structural order of the film and leads to the promotion of hydrogen elimination and an increase in cross-linking reactions at or near the surface. Consequently, the hydrogen content of PECVD a-Si:H is reduced as the temperature of the source gas line is increased.

It was found that pre-heating the source gases had no measurable effect on the deposition rate of the a-Si:H material within the parameter space explored. In addition, there was no significant increase in the surface temperature of the substrate, even at the highest gas-line temperature of 400°C. Low deposition rates and high substrate temperatures can improve the quality of a-Si:H by enhancing the growth process. A decrease in the deposition rate can result in greater time for the film-forming radicals to find an optimum bonding site. And a higher substrate temperature leads to greater diffusion of the precursors on the growing surface and the removal of excess hydrogen from the film. Therefore, these results taken together suggest that beneficial deposition phase reactions can take place at low substrate temperatures using the source gas heating technique.

The reduction in the concentration of hydrogen was accompanied by an improvement in the microstructure factor (R), resulting from an increase in the monohydride fraction. The presence of di- and poly-hydrides can lead to the formation of microvoids within the a-Si:H network. The consequence of which is porous, poor quality material with a significant hydrogen content and a low photoconductivity. This problem is exacerbated when low deposition temperatures are used. However,

the correlation between R and the void fraction, demonstrates that material density can also be enhanced by using this technique.

In addition, the structural improvement is manifest in the level of disorder in the amorphous matrix of the gas heated material. Values of C_{TAUC} and B were both found to increase with gas-line temperature, and their relation to hydrogen content and R established.

Whilst the physical characteristics of the films deposited in this work approach those of high temperature films, the electrical properties are inferior. The maximum photosensitivity achieved for the optimised film was approximately 3-4 orders of magnitude. This is appreciably worse than that of device-quality films and can be attributed to a higher density of deep defect states in the gas-heated films. These are thought to be Si dangling bonds and attributable to the low deposition temperatures employed during the investigations.

The static performance of devices incorporating channel and doped layers of a-Si:H deposited with gas line pre-heating (GH-TFTs) was compared to that of devices fabricated with the source gas line at room temperature (RT-TFTs). All of the thin film layers incorporated into both sets of devices were deposited using identical PECVD recipes. The superior characteristics of the GH-TFTs are consistent with a lower density of states in the upper part of the a-Si:H bandgap for the gas-heated material.

As the values of the field effect mobility and the thermal activation energy of the mobility are dependent on the shape of the conduction band tail, it can also be concluded that the width of the band tail is reduced when the a-Si:H is deposited with gas heating. As the density of tail states is determined by the degree of disorder within the amorphous network, this fact correlates well UV/VIS spectroscopic measurements.

9.3 FUTURE WORK

Despite the demonstrated superiority of the GH-TFTs, all devices produced to date

exhibit very low field effect mobilities and unacceptable instability. Therefore, these issues need to be explored further.

One possible reason could be degradation of the silane source gas [257]. Over a period, silane can dimerise resulting in a significant Si_2H_6 content, which has an adverse effect on material properties. This is also true of phosphine gas, used to deposit n^+ a-Si:H. Thus, it is strongly recommended that both the silane and phosphine cylinders currently used in EMTERC be changed before any further investigations are undertaken.

Further analysis of the performance of TFTs incorporating gas heated a-Si:H, but using different gate insulator layers would clearly be of value. This would make it possible to investigate the interface between the source-drain channel layer and the gate insulator. Of special interest would be to analyse the performance of devices with low temperature insulating layers; in particular, silicon dioxide grown by liquid phase deposition (LPD). This material has been thoroughly studied within EMTERC [258] and results from material grown at 48 °C suggest that it has the potential to be a device quality insulator for large area substrates.

It would be instructive to use methods such as the constant photocurrent method (CPM) to investigate the slope of the valence band tail and hence evaluate the Urbach energy of the optimised film. This may yield definitive evidence of the improvement in structural order attributed to gas heating intimated in this work.

The work detailed in this thesis could also be used as a basis to investigate the production of a-Si:H at low substrate temperatures using a combination of gas heating and dual-RF excitation.

References

Presentations and Publications containing my own research

[1] M. Manhas, D. P. Oxley, R. B. M. Cross, M. M. De Souza and E. M. Sankara Narayanan, Presentation at 'Chelsea Conference on Amorphous and Organic Semiconductors, London (2001)

[2] Y. Z. Xu, R. B. M. Cross, M. Manhas, F. J. Clough, M. M. DeSouza, E. M. Sankara Narayanan, D. Flores, J. Rebollo, M. Vellehi and J. Millan, Applied Physics Letters 80 (2002) 2192

[3] M. Munier, S. K. Manhas, D. Chandr Sekhar, S. Krishnan, R. B. M. Cross, E. M. Sankara Narayanan, M. M. DeSouza, D. Flores, J. Rebollo, M. Vellehi and J. Millan, Proc. 9th International Symposium on Physical and Failure Analysis of Integrated Circuits, Singapore (2002)

[4] R. B. M. Cross, D. P. Oxley, E. M. Sankara Narayanan, Presentation at 'Amorphous and Thin Film Semiconductors', Cambridge (2003)

[5] R. B. M. Cross, D. P. Oxley, E. M. Sankara Narayanan, Electron Device Letters (in submission)

Other references – listed in order of appearance in the text

[1] R.C. Chittick, J.H. Alexander and H.F. Sterling, J. Electrochemical Society **116** (1969) 77

[2] W. E. Spear and P.G. LeComber, J. Non-Crystalline Solids **8-10** (1972) 727

[3] W. E. Spear and P.G. LeComber, Solid State Communications, **17** (1975) 1193

[4] D. E. Carlson and C. R. Wronski, Applied Physics Letters **28** (1976) 671

[5] P. Nath, C. Vogeli, A. Singh, L. Slominsky, J. Call, M. Walters and S. Guha, Proc. 2nd World Conference on PV Solar Energy Conversion, (1998) 2538-2541

[6] V. Pérez-Méndez, G. Cho, J. Drewery, T. Jing, S.N. Kaplan, S. Qureshi, D. Wildermuth, I. Fujieda and R.A. Street, J. Non-Crystalline Solids **137 & 138** (1991) 1291-1296

[7] R.A. Street, X.D. Wu, R. Weisfield, S. Ready, R. Apte, M. Nguyen and P. Nylen, Proc. 9th Workshop on room-temperature semiconductors, X- and γ-ray detectors, Grenoble 18-22 Sept. (1995)

[8] M. Hack, H. Tuan, J. Shaw, M. Shur and P. Yap, Mater. Res. Soc. Symp. Proc. **95** (1987) 457

[9] B. J. Lechner, F. J. Marlowe, E. O. Nester and J. Tults, Proc of the IEEE **59** (1971) 1566

[10] S. Hotta, S. Nagata, Y. Miyata, K. Yokoyama, K. Adachi, T. Chikamura, M. Yoshiyama, A, Nisikawa and K. Kawasaki, SID Digest (1986) 296

[11] F. C. Matacotta and G. Ottaviani, Ed., *Science and Technology of Thin Films*, (World Scientific Publishing, Singapore, 1995)

[12] J. Kanicki, Ed., *Amorphous and Microcrystalline Semiconductor Devices - Materials and Device Physics* (Artech House, Norwood, MA, U.S.A., 1992)

[13] R. Young, *FPD Update*, 3 No.1 (Semiconductor Equipment and Materials International, Winter, 2003)

[14] P. C. Taylor, in *Semiconductors and Semimetals*, Ed. J. I. Pankove **21C** (Academic, Orlando, Fla., U.S.A., 1984) 99

[15] E. A. Davis and N. F. Mott, Philosophical Magazine **22** (1970) 1065

[16] N. H. Nickel and W. B. Jackson, J. of Non-Crystalline Solids **164-166** Part 1 (1993) 281

[17] E. A. Davis, J. of Non-Crystalline Solids **198-200** (1996) 1

[18] A. Shin, J-L, Yeh and S-C. Lee, J. of Applied Physics **88** (2000) 1684

[19] A. H. Mahan, D. L. Williamson, B. P. Nelson and R. S. Crandall, Sol. Cells **27**, (1989) 465

[20] H. Meiling, M. J. van den Boogaard, R. E. I. Schropp, J. Bezemer, and W. F. van der Weg, Mater. Res. Soc. Symp. Proc. **192** (1990) 645

[21] S. Acco, D. L. Williamson, W. G. J. H. M. van Sark, W. C. Sinke, W. F. van der Weg, A. Polman, and S. Roorda, Phys. Rev. **B 58** (1998) 12853

[22] A. H. Mahan, D. L. Williamson, B. P. Nelson, and R. S. Crandall, Phys. Rev. B **40** (1989) 12024

[23] S. Acco, W. Beyer, E. E. Van Faassen, and W. F. van der Weg, J. Appl. Phys. **82** (1997) 2862

[24] R. S. Crandall, X. Liu, and E. Iwaniczko, J. Non-Crystalline Solids **227-230** (1998) 23

[25] E. A. Davis and N. F. Mott, Philosophical Magazine **22** (1970) 903

[26] N. F. Mott, Philosophical Magazine **22** (1970) 7

[27] W. Beyer, A, Medeisis and H. Mell, Communications on Physics **2** (1977) 121

[28] N. F Mott, Advances in Physics **16** (1967) 49

[29] D. Adler, Physical Review Letters 41 (1978) 1755

[30] R. A. Street, Physical Review Letters **49** (1982) 1187

[31] R. A. Street, J. Non-Crystalline Solids **77&78** (1985) 1

[32] G. Krötz, J. Wind, H. Stitzl, G. Müller, S. Kalbitzer and H. Mannsperger Philosophical Magazine B **63** (1991) 101

[33] G. Müller, H. Mannsperger and S. Kalbitzer, Philosophical Magazine B **53** (1986) 935

[34] R. A. Street, *Hydrogenated Amorphous Silicon*, Cambridge Solid State Science Series (Cambridge University Press, Cambridge, U.K., 1991)

[35] D. L. Staebler and C. R. Wronski, Applied physics Letters **31** (1977) 292

[36] Z. E. Smith and S. Wagner, in *Amorphous Silicon and Related Materials*, Ed. H. Fritzsche (World Scientific, Singapore, 1989) 409

[37] Z. E. Smith, in *Properties of Amorphous Silicon*, **16.2** (INSPEC, The Institution of Electrical Engineers, London, 1989) 518

[38] G. Müller, H. Mannsperger and S. Kalbitzer, Applied Physics A **39** (1986) 243

[39] G. Müller, Applied Physics A **45** (1988) 41

[40] R. A. Steet, Physica B **170** (1991) 69

[41] M. Stutzmann, W. B. Jackson, and C. C. Tsai, Phys. Rev. B 32 (1985) 23

[42] S. Yamasaki and J. Isoya, J. Non-Crystalline. Solids **164-166** (1993) 169

[43] C. Godet, P. Morin, and P. Roca i Cabarrocas, J. Non-Crystalline Solids **198-200** (1996) 449

[44] S. Zafar and E. A. Schi_, Phys. Rev. B **40** (1989) 5235

[45] C. Manfredotti, F. Fizzotti, M. Boero, P. Pastorino, P. Polesello, and E. Vittone, Phys. Rev. B **50** (1994) 18046

[46] H. M. Branz, Solid State Commun. **105** (1998) 387

[47] R. Biswas, Q. Li, B. C. Pan, and Y. Yoon, Mater. Res. Soc. Symp. Proc. **467** (1997) 135

[48] W. Jackson, C. C. Tsai and R. Thompson, J. Non-Crystalline Solids **114** (1989) 396

[49] M. J. Powell, R. B. Wehrspohn and S. C. Deane, J. Non-Crystalline Solids **299-302** (2002) 556

[50] H. Dersch, J. Stuke and J. Beicher, Applied Physics Letters 38 (1981) 456

[51] R. A. Street, J. Kakalios, C. C. Tsai, W. B. Jackson, Philosophical Magazine B **56** (1987) 305

[52] W. B. Jackson and J. Kakalios, in *Amorphous Silicon and Related Materials*, Ed. H. Fritzsche (World Scientific, Singapore, 1989) 247

[53] R. A. Street, J. Kakalios, C. C. Tsaiand T. M. Hayes, Phys. Rev. B **35** (1987) 1316

[54] R. A. Street and J. Kakalios, Philosophical Magazine B **54** (1986) L21

[55] R. A. Street, M. Hack and W. B. Jackson, Phys. Rev. B **37** (1988) 4209

[56] J. Stuke, J. Non-Crystalline Solids **97&98** (1987) 1

[57] Y. Bar-Yam, D. Adler and J. D. Joannopoulos, Phys. Rev. Letters **57** (1986) 467

[58] Z. E. Smith and S. Wagner, in *Amorphous Silicon and Related Materials*, Ed. H. Fritzsche (World Scientific, Singapore, 1989) 409

[59] K. Winer, Phys. Rev. B **41** (1990) 12150

[60] M. J. Powell and S. C. Deane, Phys. Rev. B **48** (1993) 10815

[61] S. C. Deane and M. J. Powell, J. Non-Crystalline Solids **198-200** (1996) 295

[62] M. Stutzmann, Philosophical Magazine B **56** (1987) 63

[63] M. J. Powell, C. van Berkel, J. R. Hughes, Applied Physics Letters **54** (1989) 1323

[64] J. E. Lilienfeld, U. S. Patent No. 1 745 175 (1930)

[65] O. Heil, British Patent No. 439 457 (1935)

[66] D. Khang and M. M. Atalla, I. R. E. Solid State Device Research Conference (Pittsburg, Pa., 1960)

[67] P. K. Weimer, Proc. of the IRE **50** (1962) 1462

[68] T. P. Brody, J. A. Asars and G. D. Dixon, IEEE Transactions on Electron Devices, **20** (1973) 995

[69] R. W. Dutton and R. S. Muller, Proc. of the IEEE **59** (1971) 1511

[70] D. Lile and J. C. Anderson, Solid State Electronics **12** (1969) 735

[71] P. Migliorato and D. B. Meakin, Applied Surface Science **30** (1987) 353

[72] T. Nishimura, A. Ishizu, T. Matsumoto and Y. Akasaka, Mater. Res. Soc. Symp. Proc. **33** (1984) 221

[73] P.G. LeComber, W. E. Spear and A. Ghaith, IEE Electronics Letters **15** (1979) 179

[74] H. C. Tuan, M. J. Thompson, N. M. Johnson and R. A. Lujan, IEE Electron Device Letters **3** (1982) 357

[75] M. J. Powell, IEEE Transactions on Electron Devices **36** (1989) 2753

[76] M. J. Powell and J. W. Orton, Applied Physics Letters **45** (1984) 171

[77] G. w. Neudeck and A. K. Malhorta, J. Applied Physics **56** (1984) 396

[78] S. Kishida, Y. Naruke, Y. Uchida and M. Matsumura, Japanese J. Applied Physics **22** (1983) 511

[79] M. J. Powell, Philosophical Magazine B **43** (1981) 93

[80] M. J. Powell, B. C. Easton and D. H. Nicholls, J. Applied Physics **53** (1982) 5068

[81] M. J. Powell and J. Pritchard, J. Applied Physics **54** (1984) 3244

[82] M. Shur and M. Hack, J. Applied Physics **55** (1984) 3831

[83] I. Chen, J. Applied Physics **56** (1984) 396

[84] T. Leroux, Solid State Electronics **29** (1986) 47

[85] S. C. Deane and M. J. Powell, J. Applied Physics **74** (1993) 6655

[86] M. J. Powell, Applied Physics Letters **43** (1986) 597

[87] R. A. Street and C. C. Tsai, Applied Physics Letters **48** (1986) 1672

[88] A. R. Hepburn, J. M. Marshall, C. Main, M. J. Powell and C. van Berkel, Phys. Rev. Letters **56** (1986) 2215

[89] R. E. I. Schropp and J. F. Verwey, Applied Physics Letters **59** (1987) 185

[90] W. B. Jackson and M. D. Moyer, Phys. Rev. B **36** (1987) 6217

[91] C. van Berkel and M. J. Powell, Applied Physics Letters **51** (1987) 1094

[92] H. Koelmans and H. C. De Graaff, Solid State Electronics **10** (1967)

[93] M. J. Powell, C. van Berkel, J. R. Hughes, Applied Physics Letters 54 (1989) 1323

[94] R. A. Street, Solar Cells **24** (1988) 211

[95] M. J. Powell, I. D. French and J. R. Hughes, J. Non-Crystalline Solids **114** (1989) 642

[96] M. J. Powell C. van Berkel and I. D. French, Non-Crystalline Solids **97&98** (1987) 321

[97] M. J. Powell C. van Berkel, I. D. French and D. H. Nicholls, Applied Physics Letters **51** (1987) 1242

[98] R. E. I. Schropp, J. W. C. Veltkamp, J. Snijder and J. F. Verwey, IEEE Transactions on Electron Devices 32 (1985) 1757

[99] R. J. Nemanich, in *Semiconductors and Semimetals*, Ed. J. I. Pankove **21C** (Academic, Orlando, Fla., U.S.A., 1984) 375

[100] M. J. Powell, in *Properties of Amorphous Silicon*, **19.4** (INSPEC, The Institution of Electrical Engineers, London, 1989) 598

[101] T. Chikamura, S. Hotta and S. Nagata, Mater. Res. Soc. Symp. Proc. 95 (1987) 421

[102] R. E. I. Schropp and J. F. Verwey, Mater. Res. Soc. Symp. Proc. **95** (1987) 489

[103] S. Ishihara, M. Kitagawa and T. Hirao, J Applied Physics **62** (1987) 837

[104] S. Ishihara, Thin Solid Films **182** (1989) 229

[105] D. H. Zhang, B. Chen and D. Haneman, Thin Solid Films **208** (1992) 87

[106] M. Shahidul Haque, H. A. Naseem, W. D. Brown and S. S. Ang, , Mater. Res. Soc. Symp. Proc. **258** (1992) 1037

[107] A. Yamada, M. Konagai and K. Takahashi, Japanese J. of Applied Physics **24** (1985) 1586

[108] P. K. Boyer, G. A. Roche, W. H. Ritchie and G. J. Collins Applied Physics Letters **40** (1982) 716

[109] M. Meunier, T. R. Gattuso, D. Adler and J. S. Haggerty, Applied Physics Lettters **43** (1983) 273

[110] M. Konagai, Mater. Res. Soc. Symp. Proc. **70** (1986) 257

[111] Y. S. Tsuo and W. Luft, Applied Physics Communications **10** (1990) 71

[112] M. Tanaka, K. Ninomya, N. Nakamura, S. Tsuda, S. Nakano, M. Ohnishi and Y. Kuwano, Japanese J. Applied Physics **27** (1988) 14

[113] M. Ohnishi, N. Nishiwaki, K. Uchihashi, K. Yoshida, M. Tanaka, K. Ninomiya, M. Nishikuni, N. Nakamura, S. Tsuda, S. Nakano T. Yazaki, Y. Kuwano, Japanese J. Applied Physics **27** (1988) 40

[114] S. Kato and T. Akoi, J. Non-Crystalline Solids **77&78** (1985) 813

[115] A. J. Flewitt, A. P. Dyson, J. Robertson and W. I. Milne, Proc. Electrochemical Society, **2000-31** (2001) 25

[116] H. Chatham and P. K. Bhat, in *Amorphous Silicon Technology – 1989*, Ed. A. Madan, M. J. Thompson, P. C. Taylor, Y. Hamakawa and P. G. LeComber (Mater. Res. Soc. Symp. Proc. **149** (San Diego, CA., 1989) 447

[117] H. Weismann, A. K. Ghosh, T. McMahon and M. Strongin J. Applied Physics **50** (1979) 3752

[118] H. Matsumura, Japanese J. Applied Physics **25/2** (1986) L949

[119] J. Doyle, R. Robertson, G. H. Lin, M. Z. He and A. Gallagher, Applied Physics Letters **64** (1988) 3215

[120] A. H Mahan, J. Carapella, B. P. Nelson, R. S. Crandall and I. Balberg, J. Applied Physics **69** (1991) 6728

[121] R. Bruggeman, A. Hierzenbergger, P. Reinig, M. Rojahan, M. B. Schubert, S. Schweizer, H. N. Wanka and I. Zrinscak, J. Non-Crystalline Solids **227-230** (1998) 982

[122] H. Curtins, N. Wyrsch and A. Shah, Electronics Letters **23** (1987) 228

[123] S. Oda and M. Yasukawa, J. Non-Crystalline Solids **137&138** (1991) 677

[124] S. R. Jadkar, J. V. Sali, S. T. Kshrisagar and M. G. Takwale, Thin Solid Films **437** (2003) 18

[125] B. Stannowski and R. E. I. Schropp, Thin Solid Films **383** (2001) 125

[126] H. Matsumura, J. Applied Physics 65 (1989) 4396

[127] C. Mukherjee, C. Anandan, T. Seth, P.N. Dixit and R. Bhattacharyya, Thin Solid Films **423** (2003) 18

[128] M. Heintz and R. Zedlitz, J. Non-Crystalline Solids **164-166** (1993) 55

[129] M. Heintz, R. Zedlitz and G. H. Bauer, J. Physics D: Applied Physics **26** (1993) 1781

[130] B. Stannowski and R. E. I. Schropp, SAFE2001 (Semiconductor Advances for Future Electronics) Nov. 2001, Veldhoven, The Netherlands

[131] G. Bruno, P. Cappezzuto and G. Cicala, in *Plasma Deposition of Amorphous Silicon-Based Materials*, Ed. G. Bruno, P. Cappezzuto and A. Madan (Academic Press, Boston, MA, U.S.A., 1995) 4

[132] G. K. Wehner, Advances in Electronics and Electron Physics **VII** (1955) 253

[133] H. R. Koenig and L. I. Maissel, IBM J. Research and Development **14** (1970) 168

[134] M. V. Alves, M. A. Liebermann, V. Vahedi, and C. K. Birdsall, J. Applied. Physics. **69** (1991) 3823

[135] F. J. Kampas and R. W. Griffith, J. Applied Physics **52** (1981) 1285

[136] R. Robertson and A. Gallagher, J. Applied Physics **59** (1986) 3402

[137] J. Perrin, O. Leroy and M. C. Bordage, Contributions to Plasma Physics **36** (1995) 3

[138] M. J. Kushner, Mater. Res. Soc. Symp. Proc. **68** (1986) 293

[139] A. Matsuda, Plasma Physics and Controlled Fusion **39** (1997) A431

[140] V. A. Godyak and A. S. Khanneh, IEEE Transactions on Plasma Science **PS-14** (1986) 112

[141] J. Perrin, P. Roca i Cabarrocas, B. Allain, and J.-M. Friedt, Japanese J. Applied Physics **27** (1988) 2041

[142] J. L. Andujar, E. Bertran, A. Canillas, C. Roch, and J. L. Morenza, J. Vacuum Science Technology A **9** (1991) 2216

[143] R. B. Werhspohn, S. C. Deane, I. D. French, I. Gale, J. Hewett and M. J. Powell, J. Applied Physics **87** (2000) 144

[144] C. G. Goedde, A. J. Lichtenberg and M. A. Lieberman, J. Applied Physics **64** (1988) 4375

[145] M. J. Kushner, IEEE Transactions on Plasma Science **PS-14** (1986) 188

[146] P. Roca i Cabarrocas, P. Gay and A. Hadjadj, J. Vacuum Science Technology A **14** (1996) 655

[147] A. A. Howling, J.-L. Dorier, and C. Hollenstein, Appl. Phys. Lett. **62** (1993) 1341

[148] J. Perrin, in *Plasma Deposition of Amorphous Silicon-Based Materials*, Ed. G. Bruno, P. Capezzuto, and A. Madan (Academic Press, Boston, MA, U.S.A., 1995) 177

[149] K. Tanaka and A. Matsuda, Material Science Reports **2** (1987) 139

[150] A. Gallagher, J. Applied Physics **63** (1988) 2406)

[151] A. J. Flewitt, J. Robertson and W. I. Milne, J. Applied Physics **85** (1999) 8032

[152] J. Robertson, J. Applied Physics **87** (2000) 2608

[153] G. Ganguly and A. Matsuda, Physical Review B **47** (1993) 3661

[154] G. Ganguly and A. Matsuda, J. Non-Crystalline Solids **164** (1993) 31

[155] K. Winer, Physical Review B **41** (1990) 7952

[156] R. A. Street, Physical Review B **43** (1991) 2454: **44** (1991) 10610

[157] K. Gleason, K. S. Wang, M. K. Chen and J. A. Reimer J. Applied Physics **61** (1987) 2866

[158] M. J. Kushner, J. Applied Physics **63** (1988) 2532

[159] T. Shirafuji, S. Nakajiuma, Y. F. Wang, T. Genji and K. Tachibana, Japanese J. Applied Physics Part 1 **32** (1993) 1546

[160] J. Robertson, J. Non-Crystalline Solids **266-269** (2000) 79

[161] J. Perrin, M. Shiratani, P. Kae-Nune, H. Videlot, J. Jolly and J. Guillon, J. Vacuum Science Technology A **16** (1998) 278

[162] W. M. M. Kessels, A. H. M. Smets, D. C. Marra, E. S. Aydil, D. C. Schram and M. C. M. van de Sanden, Thin Solid Films **383** (2001) 154

[163] M. J. Kushner, J. Applied Physics **62** (1987) 4763: M. J. McCaughney and M. J. Kushner, J. Applied Physics **65** (1989) 186

[164] A. J. Flewitt, J. Robertson, and W. I. Milne, J. Non-Cryst. Solids **266-269** (2000) 74

[165] A. S. Ferlauto, R. J. Koval, C. R. Wronski and R. W. Collins, Applied Physics Letters **80** (2002) 2666

[166] A. Von Keudell and J. R. Abelson Physical Review B **59** (1999) 5791

[167] S. Ramalingam, D. Maroudas, and E. S. Aydill, J. Applied Physics. **86** (1999) 2872

[168] M. C. M. van de Sanden, W. M. M. Kessels, R. J. Severens and D. C. Schram, Plasma Physics and Controlled Fusion 41 (1999) A365

[169] W. Beyer, J. Non-Crystalline Solids **198** (1996) 40

[170] J. C. Knights, J. Non-Crystalline Solids **32** (1977) 393

[171] S. Yamasaki, T. Umeda, J. Isoya, and K. Tanaka, Applied Physics Letters **70** (1997) 1137

[172] J. Robertson, C. W. Chen, M. J. Powell, and S. C. Deane, J. Non-Crystalline Solids **227-230** (1998) 138

[173] K. J. Chang and J. D. Chadi, Physical Review B **40** (1990) 11644

[174] R. W. Collins and A. S. Ferlauto, Current Opinion in Solid State and Materials Science **6** (2002) 425

[175] H. Aguas, R. Martins and E. Fortunato, Vacuum **60** (2001) 247

[176] J. Perrin, J. Non-Crystalline Solids **137** (1991) 639

[177] J. W. Rabalais, A. H. Al-Bayati, K. J. Boyd, D. Marton, J. Kulik, Z. Zhang, and W. K. Chu, Physical Review B **53** (1996) 10781

[178] J. C. Knights, *The Physics Of Hydrogenated Amorphous Silicon I: Structure, Preparation and Devices*, Eds. J. D. Joannopoulos and G. Lucovsky, Topics in Applied Physics 55 (Springer Verlag, Berlin, 1983) 5

[179] P. Roca i Cabarrocas, Mater. Res. Soc. Symp. Proc. **149** (1989) 33

[180] U. Kroll, F. Finger, J. Dutta, H. Keppner, A. Shah, A. Howling, J. L. Dorier and C. Hollenstein, Mater. Res. Soc. Symp. Proc. **258** (1992) 135

[181] D. Mataras, S. Cavadias and D. Rapakoulias, J. Applied Physics **66** (1989) 119

[182] N. Itabashi, N. Nishikawa, M. Magane, T. Goto, A. Matsuda, C. Yamada and E. Hirota, Japanese J. Applied Physics **29** (1990) 585

[183] Y. Miyoshi, Y/ Yoshida, S. Miyazaki and M. Hirose, J. Non-Crystalline Solids **198** (1996) 102

[184] P. Roca i Cabarrocas, P. Morin, V. Chu, J. P. Conde, J. Z. Liu, H. R. Park and S. Wagner, J. Applied Physics 69 (1991) 2942

[185] T. D. Moustakas, D. A. Anderson and W. Paul, Solid State Communications 23 (1977) 155

[186] P. Alpium and V. Chu, J. Applied Physics 86 (1999) 3812

[187] M. B. Schubert, Thin Solid Films **337** (1999) 240

[188] H. Gleskova, S. Wagner, V. Gasparik and P. Kovac J. Electrochemical Society **148** (7) (2001) G370

[189] A. Sazonov, A. Nathan and D. Striakhilev, J Non-Cryst. Solids **266-269** (2000) 1329

[190] C.-S. Yang, L. L. Smith, C.. B. Arthur and G. N. Parsons J. Vacuum Science Technology B **18** (2000) 683

[191] Y. Hishikawa, S. Tsuge, N. Nakamura, S. Tsuda, S. Nakano and Y. Kuwano, J. Applied Physics 69 (1991) 508

[192] P. Roca i Cabarrocas, Applied Physics Letters 65 (1994) 1674

[193] E. Srinivasan, D. A. Lloyd and G. N. Parsons, J. Vacuum Science Technology A 15 (1997) 77

[194] G. N. Parsons, J. Non-Crystalline Solids 266-269 (2000) 23

[195] A. Matsuda, S. Yokoyama, and K. Tanaka, Applied Physics Letters **53** (1988) 1489

[196] Y. Hishikawa, M. Sasaki, S. Tsuge and S. Tsuda, Japanese J. of Applied Physics Part 1 **33** (1994) 4373

[197] D. Das, S. Chattopadhyay, A. K. Barua and R. Banerjee, J. Applied Physics **78** (1995) 3193

[198] T. Arai and H. Shirai J. Applied Physics . **80** (1996) 4976.

[199] M. H. Brodsky, M. Cardona and J. J. Cuomo, Physical Review B **16** (1977) 3556

[200] A. A. Langford, M. L. Fleet, B. P. Nelson, W. A. Lanford and N. Maley, Physical Review B **45** (1992) 13367

[201] H. Shanks, C. J. Fang, L. Ley, M. Cardona, F. J. Demond and S. Kablitzer, Physica Status Solidi B **100** (1980) 43

[202] A. H. Mahan, P. Raboisson and R. Tsu, Applied Physics Letters **50** (1987) 335

[203] J. Tauc, R. Grigorovici and A. Vancu, Physica Status Solidi **15** (1966) 627

[204] M. Ohring, *The Material Science of Thin Films*, (Academic Press, Boston, MA. USA, 1992)

[205] S. M. Sze, *Physics of Semiconductor Devices*, (Wiley-Interscience, New York, 1981)

[206] E.H Nicollian and J. R Brews, *MOS Physics and Technology*, (Wiley, New York, 1982)

[207] L. M. Terman, Solid State Electronics, **5** (1962) 285

[208] C. van Berkel, J. R. Hughes and M. J. Powell, Mater. Res. Soc. Symp. Proc. **95** (1987) 445

[209] H. Fritzsche, Solar Energy Materials **3** (1980) 447

[210] G. Turban, Y. Catherine, and B. Grolleau, Thin Solid Films **60** (1979) 147

[211] C. C. Tsai, G. B. Anderson, and R. Thompson, J. Non-Cryst. Solids **137-138** (1991) 637

[212] S. Nishikawa, H. Kakinuma, T. Watanabe and K. Nihei, Japanese J. of Applied Physics **24** (1985) 639

[213] H. Shirai, J. Hanna and I. Shimizu, Japanese J. of Applied Physics **30** (1991) L881

[214] G. N. Parsons, J. J. Boland and J. C. Tsang, Japanese J. of Applied Physics **32** (1992) 1943

[215] G. Kaniadakis, in *Properties of Amorphous Silicon*, **8.1&8.2** (INSPEC, The Institution of Electrical Engineers, London, 1989) 269

[216] E. N. Economou and D. A. Papaconstantopoulos, Physical Review B **23** (1981) 2042

[217] G. D. Cody, T. Tiedje, B. Abeles, B. Brooks and Y. Goldstein, Physical Review Letters **47** (1981) 1480

[218] S. Okamoto, Y. Hishikawa, and S. Tsuda, Japanese J. of Applied Physics **35** (1996) 26

[219] P. Roca i Cabarrocas, S. Hamma, S. N. Sharma, G. Viera, E. Bertran and J. Costa, J. Non-Crystalline Solids **227-230** (1998) 871

[220] A. Madan, P. G. LeComber and W. E. Spear, J. Non-Crystalline Solids **20** (1976) 239

[221] J. Shirafuji, M. Kuwagaki, T. Sato and Y. Inuishi, Japanese J. of Applied Physics **23** (1984) 1278

[222] G. Llavareda, C. Nunes de Carvalho, A. Amaral, J. P. Comde, M. Viera and V. Chu, Vacuum **64** (2002) 245

[223] A. Madan, in *Plasma Deposition of Amorphous Silicon-Based Materials*, Ed. G. Bruno, P. Capezzuto, and A. Madan (Academic Press, Boston, MA, U.S.A., 1995) 264

[224] R. A. Street, J. C. Knights, and D. K. Biegelsen, Phys. Rev. B **19** (1978) 3027

[225] M. H. Brodsky, Thin Solid Films 10 **(1987)** L23

[226] A. Gallagher, Mater. Res. Soc. Symp. Proc.**70** (1986) 3

[227] S. Chattopadhyay, S. N. Sharma, R. Banerjee, D. M. Bhusari, S. T. Kshirsagar, Y. Chen and D. L. Williamson, J. of Applied Physics **76** (1994) 5208

[228] N. F. Mott and E. A. Davis, Electronic Processes in Non-Crystalline Materials, 2nd Ed. (Clarendon, Oxford, 1979) 289

[229] J. Robertson, Philosophical Magazine B **69** (1994) 307

[230] I. Sakata, Y. Hayashi, M. Yamanka and H. Karasawa, J. of Applied Physics **52** (1981) 4334

[231] J. Biullot and M. P. Schmidt, Physica Status Solidi B **143** (1987) 345

[232] Y. Kuo, Vacuum **51** (1998) 741

[233] M. J. Powell, Applied Physics Letters **60** (1992) 207

[234] F. H. P. M. Habraken and A. E. T. Kuiper, Mat. Sci. and Engineer.: Reports **12** (1994) 123

[235] W. M. Arnold Bik, Ph.D. thesis, Utrecht (1992)

[236] W. A. P. Claassen, W. J. G. N. Valkenburg, M. F. C. Willensen and W. M. van de Wijgert, J. Electrochem. Soc. **132** (1985) 893

[237] B. Gorowitz, T. B. Gorczyca and R. J. Saia, Solid State Technology **28** (1985) 197

[238] R. Chow, W. A. Lanford, W. Ke-Ming and R. S. Rosler, J. Applied Physics **53** (1982) 5630

[239] E. Bertran, J. M. Lopez-Villegas, J. L. Andujar, J. Campmany, A. Canillias and J. R. Morante, J. Non-Crystalline Solids **137/138** (1991) 895

[240] D. T. Murley, R. A. G. Gibson, B. Dunnet, A. Goodyear and I. D. French, J. Non-Crystalline Solids **187** (1995) 324

[241] D. L. Smith, J. Vac. Sci. Technol. A **11**, 1842 (1993)

[242] B. L. Jones, J. Non-Crystalline Solids **77&78** (1985) 957

[243] R. S. Rosler, W. C. Benzing and J. Baldo, Solid State Technology **6** (1976) 45

[244] G. M. Samuelson and K. M. Mar, J. Electrochem. Soc. **129** (1982) 1773

[245] W. A. P. Claassen, W. J. G. N. Valkenburg, F. H. P. M. Habraken and Y. Tamminga, J. Electrochem. Soc. **130** (1983) 2419

[246] E. A. Taft, J. Electrochem. Soc. **118** (1971) 1341

[247] K. M. Mar and G. M. Samuelson, Solid State Technology **23** (1980) 137

[248] Y. Kuo, J. Electrochem. Soc. **142** (1995) 186

[249] J. Robertson and M. J. Powell, Applied Physics Letters **44** (1984) 415

[250] D. T. Krick, P.M.Lenahan, and J. Kanicki, Physical Review Letters **38** (1988) 8226

[251] J. Robertson, Phil. Mag. B **63** (1991) 47

[252] J. Kanicki and N. Voke, Mat. Res. Soc. Symp. Proc,. **68** (1986) 167

[253] Y. Kuo and H. H. Lee, Vacuum **66** (2002) 299

[254] F. J. H. van Assche, W. M. M. Kessels, R. Vangheluwe, W.S. Mischke, M. Evers and M. C. M. van de Sanden, Thin Solid Films **484** (2005) 46

[255] J. W. A. M. Gielen, P. R. M. Kleuskens, M. C. M. van de Sanden, L. J. Ijzendoom, D. C. Schroam, E. H. A. Dekempeneer and J. Meneve, J. Applied Physics **80** (1996) 5986

[256] F. J. Clough, Ph.D. Thesis, Cambridge (1991)

[257] A. J. Flewitt, Private Communication, Cambridge University Engineering Department

[258] M. Manhas, D. P. Oxley, R. B. M. Cross, M. M. De Souza and E. M. Sankara Narayanan, Presentation at 'Chelsea Conference on Amorphous and Organic Semiconductors, London (2001)

Appendix A

Schematics of novel PECVD system

Vacuum Chamber - Plan View

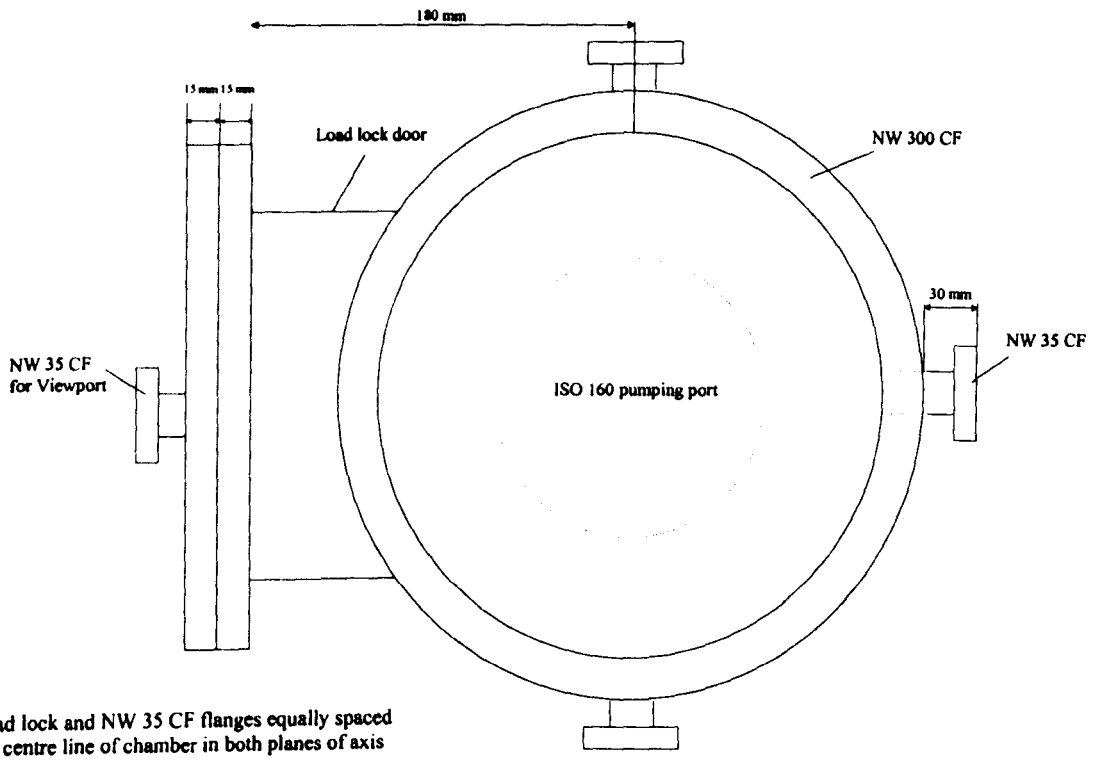

Load lock and NW 35 CF flanges equally spaced on centre line of chamber in both planes of axis

Vacuum Chamber - Main dimensions

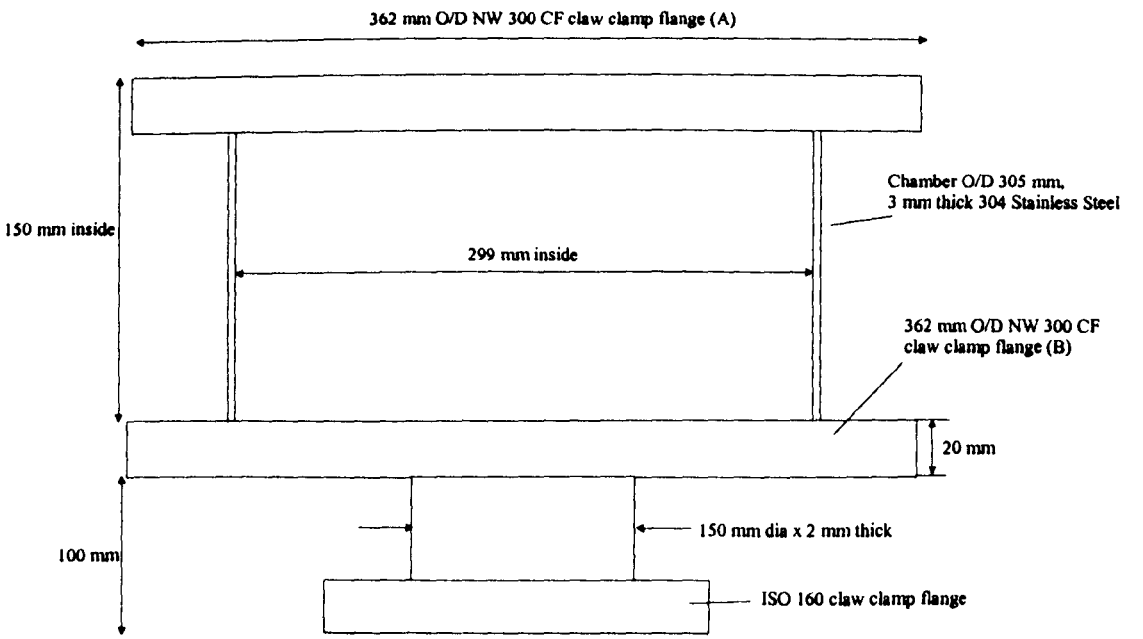

Vacuum Chamber Lid

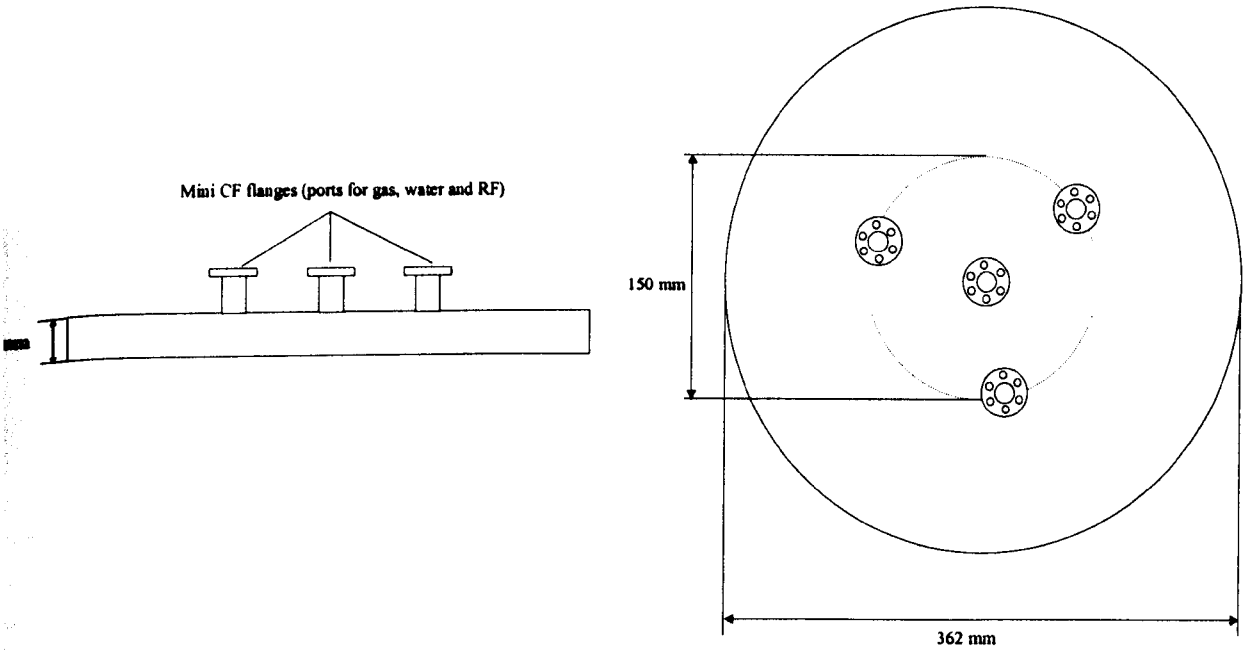

Load Lock door fitted with Viewport flange

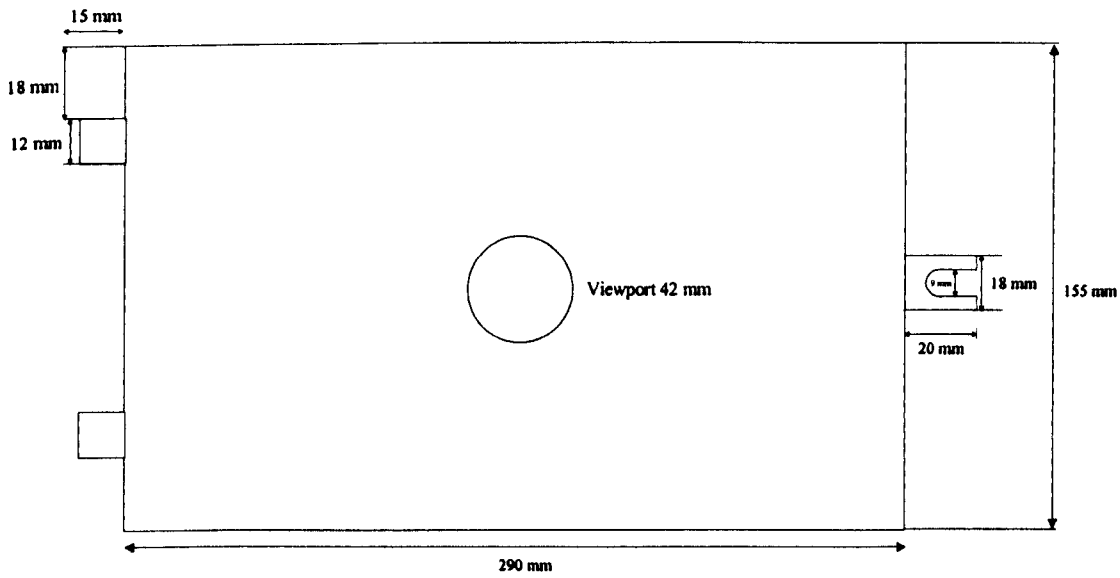

Load lock Port Flange

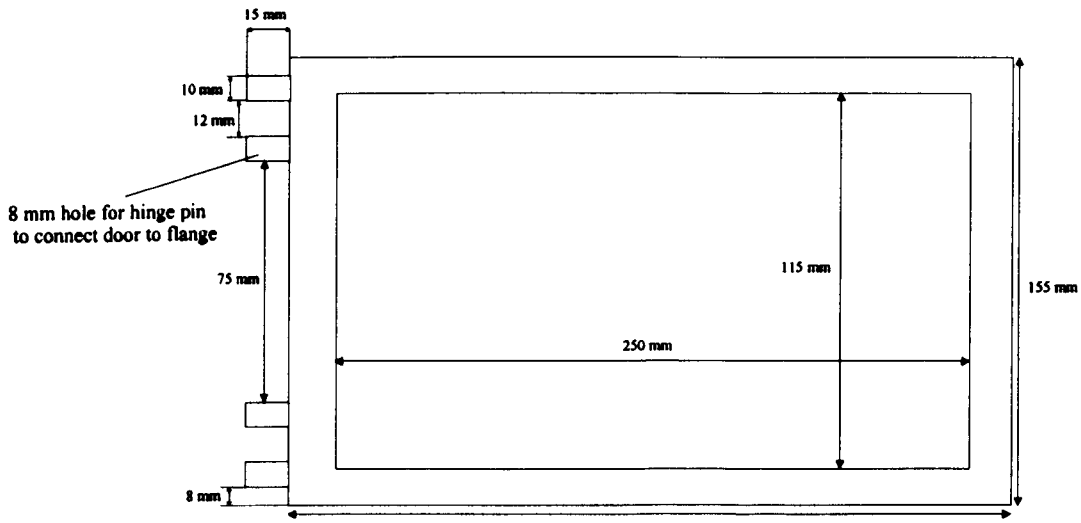

Fitted with 8mm Viton 'O' ring. Door hinge fitted to left side. Catch and thumb screw fitted to right side

Top Electrode

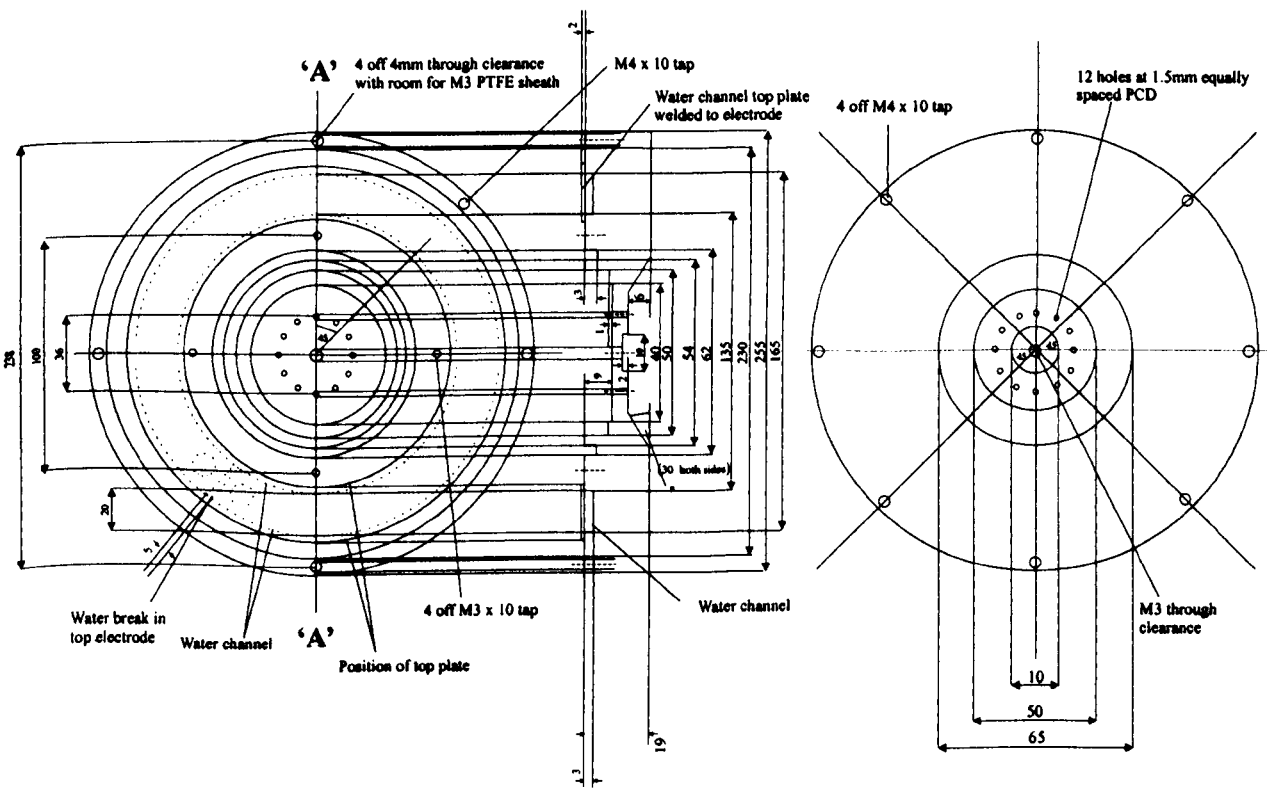

Not to scale
All measurements in mm
Tolerrance +- 0.2mm

Section 'A'- 'A'

Material: Aluminium 6082-T6

Gas Inlet assembly

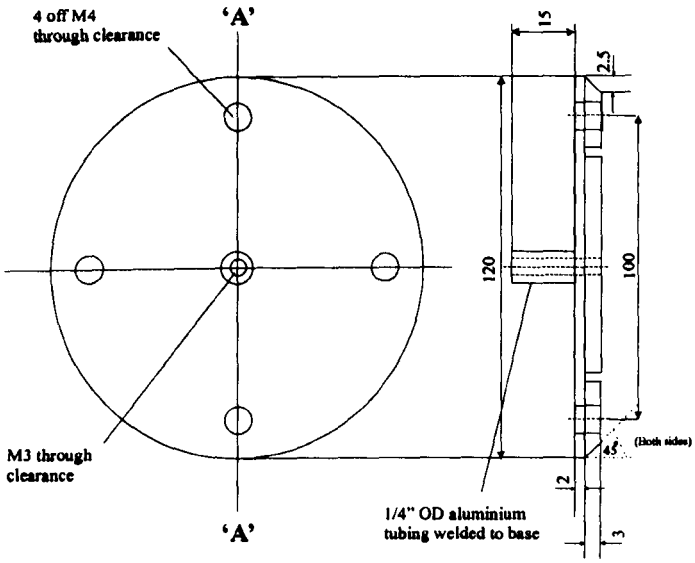

Section 'A'- 'A'

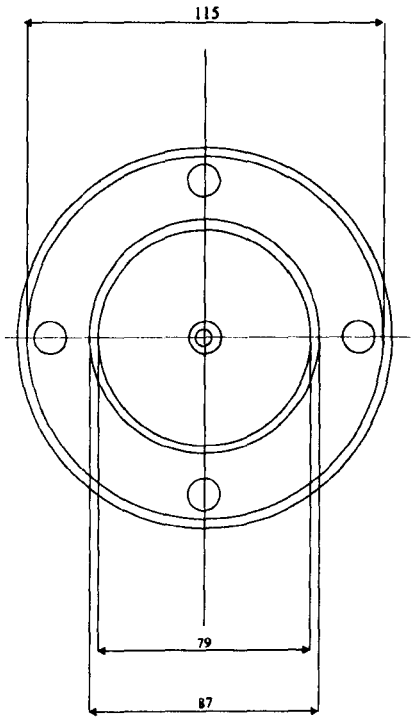

Not to scale
All measurements in mm
Tolerrance +- 0.2mm

Material: Aluminium 6082-T6

Updated 13/7/01

PTFE spacer

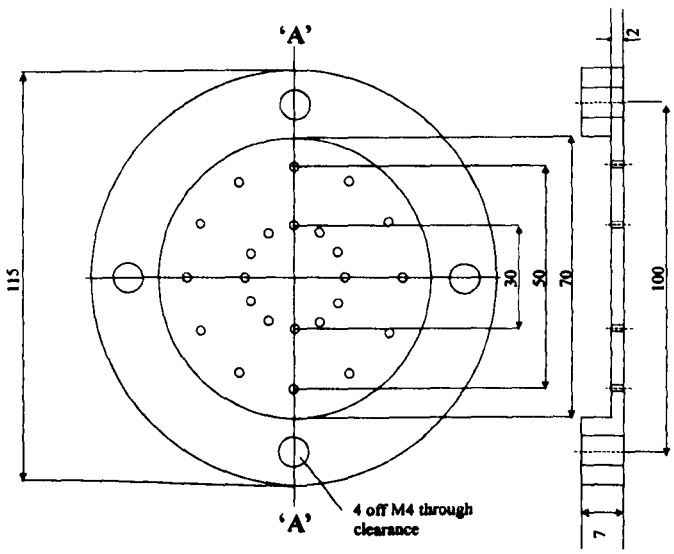

Section 'A'- 'A'

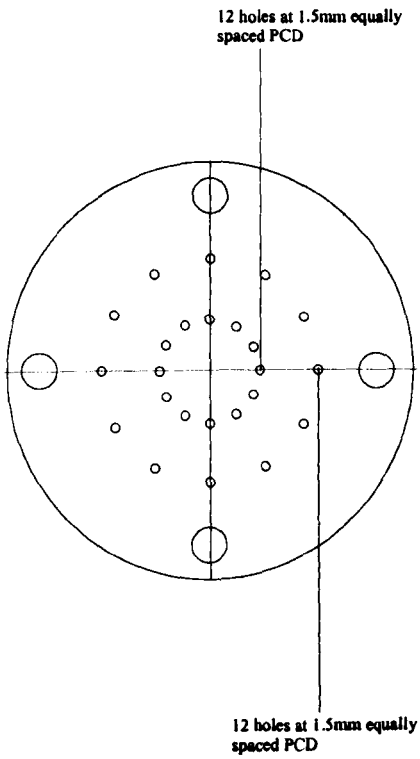

Not to scale
All measurements in mm
Tolerrance +- 0.2mm

Material: PTFE

Showerhead

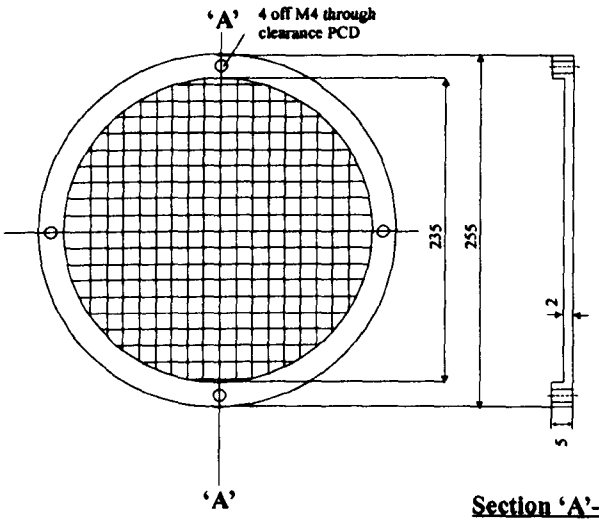

Section 'A'- 'A'

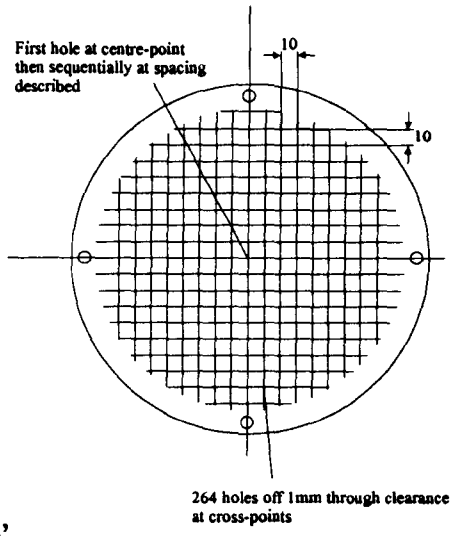

Not to scale
All measurements in mm
Tolerrance +- 0.2mm

Material: Aluminium 6082-T6

Gas Inlet Diffuser

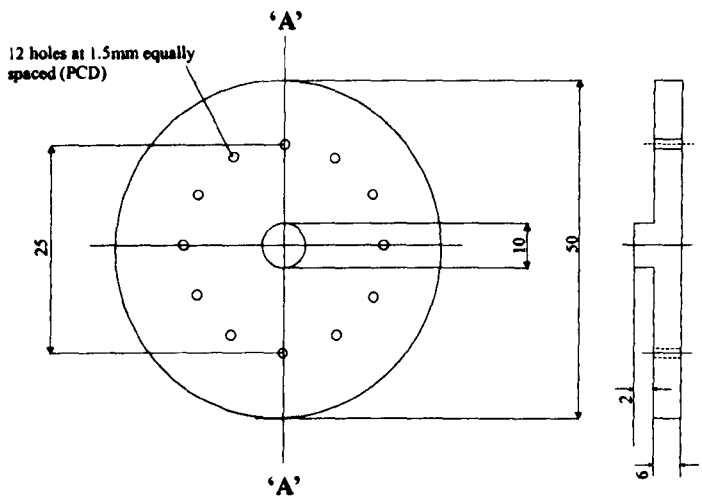

Section 'A'- 'A'

Not to scale
All measurements in mm
Tolerrance +- 0.2mm

Material: Macor, Al 6082-T6
(Two different diffusers)

Gas Spreader

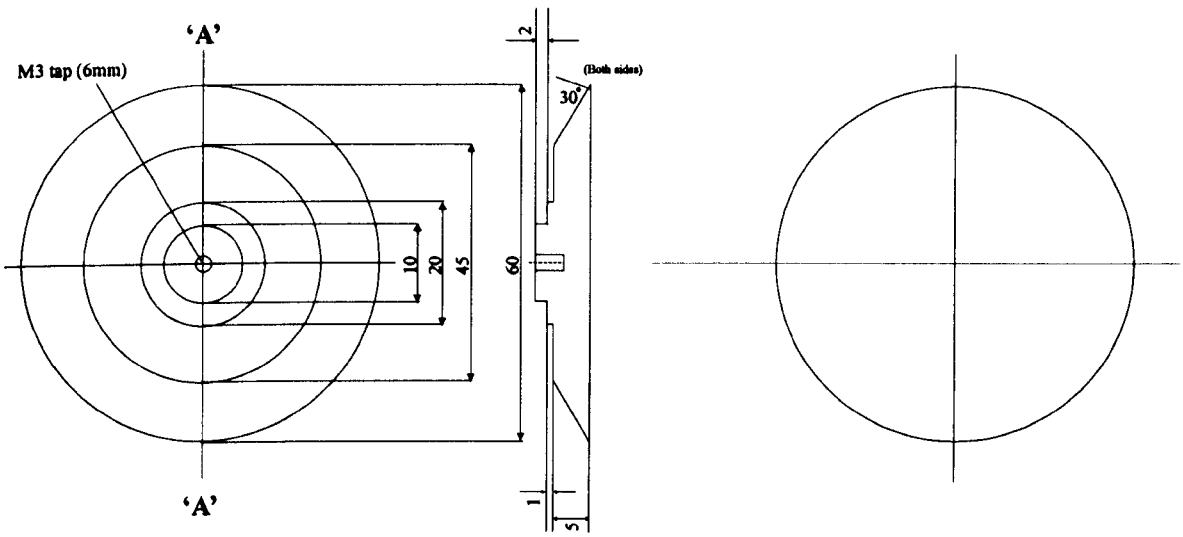

Section 'A'- 'A'

Not to scale
All measurements in mm
Tolerrance +- 0.2mm

Material: Aluminium 6082-T6

Water Channel top plate

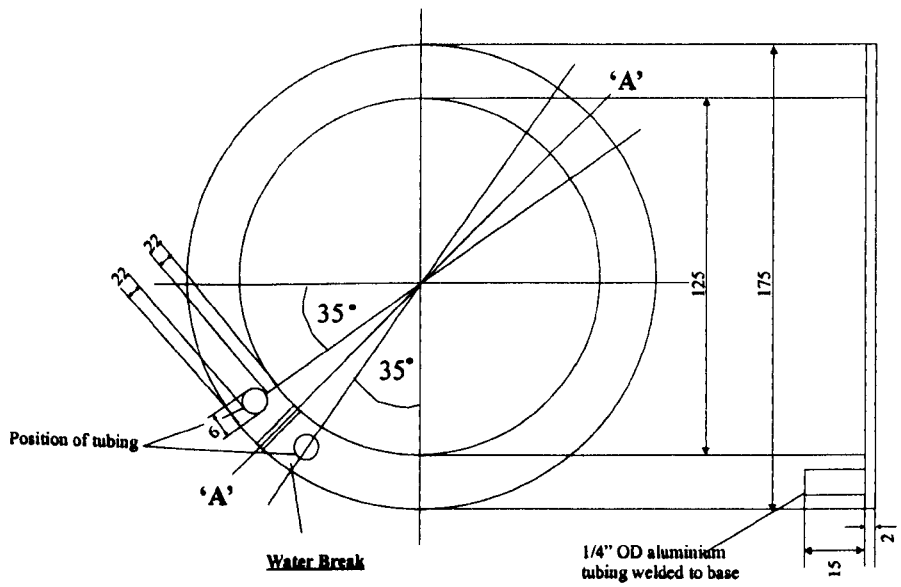

Section 'A'- 'A'

Not to scale
All measurements in mm
Tolerrance +- 0.2mm

Material: Aluminium 6082-T6

Schematic of top electrode assembly

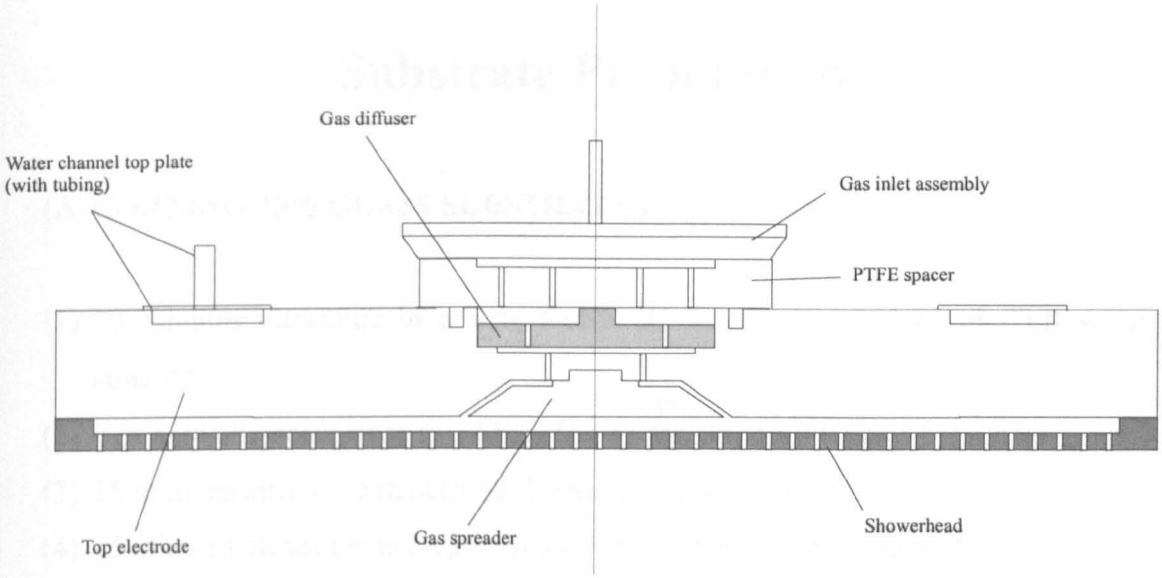

Appendix B

Substrate Preparation

(A) CORNING 7059 GLASS SUBSTRATES

(1) 30 minutes ultrasonic in a 5 % Decon 90 in 18 MΩ De-Ionised (D.I) water solution.

(2) 2 minute ultrasonic rinse in 18 MΩ D.I. water. Repeat 5 times.

(3) 15 minutes ultrasonic in acetone (Fisher Electronic grade).

(4) 15 minutes ultrasonic in isopropyl alcohol (Fisher Electronic grade).

(5) 2 minutes ultrasonic in 18 MΩ D.I. water. Repeat 5 times.

(6) Blow-dry with nitrogen gun.

(7) 1 hour drying bake in air at 200 °C.

(B) CRYSTALLINE SILICON WAFERS

(1) 10 minute 'bomb' clean (i.e. 50 % sulphuric acid and 50 % hydrogen peroxide).

(2) 2 minute ultrasonic rinse in 18 MΩ D.I. water. Repeat 5 times.

(3) 30 second dip into buffered HF (Fisher Electronic grade) (H_2O:HF (50 %), 10:1).

(4) 2 minute ultrasonic rinse in 18 MΩ D.I. water. Repeat 5 times.

(5) Spin dry at 3000 rpm for 30 seconds under flow of nitrogen.

(6) 15 minute drying bake, in air, at 100 °C.

Appendix C

TFT Fabrication Procedure

The fabrication of the TFTs used in this work is described below.

Step 1: Substrate preparation

The c-Si substrates were thoroughly cleaned as described in Appendix A. All of the substrates used were prepared under clean room conditions and transferred to the deposition system in airtight containers. This ensured that there was minimum atmospheric contamination prior to insulator deposition.

Step 2: Insulator deposition

Prior to deposition, the PECVD system was prepared by outgassing the depostion chamber for several hours at 300 °C. This was then followed by the deposition of a suitable passivation layer (~0.5 μm) of silicon nitride. The substrate was then inserted into the chamber which was evacuated to it minimum base pressure $<10^{-3}$ mTorr using the roots/rotary combination. The system was pumped at the appropriate temperature for several hours so that a steady base pressure was obtained. A suitable layer of SiN (300nm) was then deposited under the conditions as described above.

Step 3: a-Si:H deposition

The sample was removed from the Oxford Plasmatechnology μP 80 system and placed immediately into the low temperature PECVD system. The chamber had been plasma cleaned for 90 minutes using carbon tetrafluoride (CF_4) prior to sample insertion. The system was evacuated for a period of 3-4 hours as the deposition

temperature, and a layer of a-Si:H (150nm) was then deposited under the conditions described earlier.

Step 4: Doped a-Si:H deposition

Following the a-Si:H deposition, the system was immediately evacuated to base pressure again. Using silane and a premixed 1% phosphine in hydrogen gas combination and identical conditions to those use for the a-Si:H deposition, a 50nm layer of heavily doped n-type a-Si:H was then deposited.

Step 5: Source-Drain metallisation

After the doped a-Si:H deposition, the sample was removed from the low temperature PECVD system, and placed into the Nordiko sputtering unit. The time to transit the sample form the deposition chamber to the sputterer was kept at a minimum in an effort to reduce surface contamination and native oxide formation. The chamber was evacuated to a pressure of $< 10^{-7}$ Torr before deposition. Approximately 500nm of aluminium (99.999%) was then deposited by RF magnetron sputtering. The sample remained in the chamber for approximately an hour to allow for the metal layer to cool under vacuum.

The aluminium layer was then photolithographically patterned, under clean room conditions, using the procedure outline in Appendix A. The mask alignment system was a Sulzer Electro Technic mask aligner Model MA750. It is an optical alignment and projection system with a resolution of 5μm.

Step 6: Etching of doped a-Si:H layer

After the chemical etching of the source-drain contacts, the photoresist was left in place and the doped a-Si:H layer was removed using CF_4 plasma etching process. The resist was then removed.

Step 7: a-Si:H island patterning

The undoped a-Si:H was patterned by a second photolithographic step in order to produce electrically isolated a-Si:H islands. The etching was again performed using a CF_4 plasma process.

Step 8: Device annealing

The completed device was then annealed at 125 $^{\circ}$C in air for a period of 30 minutes in an effort to remove any defects caused processing.

Appendix D

Photolithographic Processing Steps

Step 1: PRELIMINARY BAKE

Bake the wafer for 30 minutes at 110 °C in air to remove any remaining moisture. Cool to room temperature using a high-pressure nitrogen gun, which also removes any loose dust particles.

Step 2: RESIST COATING

Apply 1 ml^3 of positive photoresist, and then spin at 3000 rpm for 30 seconds using an Electronic Microsystems Model 4000 photoresist spinner. The resulting photoresist layer is approximately 1.5 μm thick prior to baking.

Step 3: SOFT BAKE

Soft bake the wafer for 2 minutes at 90 °C in air.

Step 4: EXPOSURE

For the first patterning step in device fabrication, the mask was aligned roughly to the optimised orientation with respect to the substrate. For subsequent exposures, the mask was aligned to the alignment marks on the underlying layers. The exposure time was 20 seconds.

Step 5: POST RESIST BAKE

Bake the wafer for 15 minutes at 100 °C, in air.

Step 6: RESIST DEVELOPING

The exposed area of the resist is removed by dipping the wafer in a 2:1 solution of 18 MΩ D.I water and Microposit Positive developer. The developing time is dependent on the type of surface the resist is deposited onto. For highly reflecting surfaces, such as aluminium, the develop time is 1-2 minutes, but it can be as much as 4-5 minutes for a-Si:H. To aid in the removal of the resist, the wafer is constantly agitated by a Stuart Scientific SO5 mini-orbital shaker.

Step 7: POST DEVELOP BAKE

Bake the wafer for 30 minutes at 125 °C, in air.

Step 8: ETCHING

The aluminium layer was wet etched using a 4:4:1:1 solution of Acetic acid: Phosphoric acid:Nitric acid:D.I. water. (All acids were Fisher Scientific Ultra pure grade). Plasma etching was used to pattern both the doped and intrinsic a-Si:H layers. Following any wet etching, the wafer was rinsed for 2 minutes (repeat 2-3 times) in 18 MΩ D.I. water, and then allowed to stand in fresh D.I. water for at least 30 minutes. This was done in an effort to remove any residual etchants.

Step 9: RESIST STRIPPING

5 minutes ultrasonic in acetone (Fisher Scientific electronic grade).

Step 10: RINSE

2 minutes ultrasonic in 18 MΩ D.I. water. Repeat 5 times.

Step 11: DRYING

Spin-dry the wafer at 3000 rpm for 30 seconds under flow of nitrogen, then dry bake in air at 110 °C.